REQ. NO. 0-9199

CONTRACT REPORT NO. OSU81-00091

THE APPLICATION OF FRACTURE MECHANICS TO CREEP CRACK GROWTH IN PRESSURE VESSEL STEELS

D.S. Wilkinson and S.B. Biner

Department of Metallurgy and Materials Science,

and

Institute for Materials Research

McMaster University

Hamilton, Ontario, Canada, L8S 4M1

DEC 13 1984

MICROMEDIA

January 1984

119 pp

The Application of Fracture Mechanics to Creep Crack Growth in Pressure Vessel Steels

Final Report

D. S. Wilkinson and S. B. Biner
Department of Metallurgy and Materials Science
and Institute for Materials Research
McMaster University
Hamilton, Ontario, Canada
L8S 4M1

Work on this project was conducted under the auspices of the Physical Metallurgy Research Laboratories, Canada Centre for Mineral and Energy Technology; Energy, Mines and Resources, Canada.

DSS File Number: 05SU-23440-0-9199
DSS Contract Serial Number: OSU81-00091
CANMET Scientific Authority: Dr. W. R. Tyson/Dr. O. Vosikovsky

Principal Investigator: Dr. D. S. Wilkinson

January 1984

The D.S.S. File Number should be used in references to this report.

ACKNOWLEDGEMENTS

We would like to express our appreciation to the Physical Metallurgy Research Laboratory (PMRL) of the Canada Centre for Mineral and Energy Technology (CANMET) for the opportunity to perform this research. We are especially indebted to Dr. W.R. Tyson of CANMET for his help and guidance during the formative stages of this project. We are also grateful to Dr. D. Watt of the University of Windsor for substantial contributions to the ideas presented in Part I of this report. Finally, useful discussions with Dr. J.D. Embury of McMaster, Dr. A.S. Argon of M.I.T. and Dr. G.A. Webster of Imperial College are acknowledged.

ABSTRACT

This report describes the results of a project which aimed to assess the applicability of fracture mechanics concepts to creep crack growth, with particular attention being paid to thick-walled pressure vessels made of 2¼ Cr-1 Mo steel. We have approached this problem by combining an experimental assessment of damage in small scale creep tests, with crack growth simulation using finite element methods. The experimental work suggests that for coarse grained 2¼ Cr-1 Mo steel, and for creep lives of relevance to creep crack growth, the most appropriate parameter for damage is the equivalent tensile strain. A critical value of this strain required for crack advance during the finite element simulation can be obtained, using quantitative metallography on failed and interrupted creep test samples. The finite element results indicate that the rate of creep crack growth can be predicted with reasonable accuracy, if the appropriate damage condition is used. They also show that if crack growth proceeds in a stress field which is at or near the steady-state condition, then the C* integral provides an adequate parameter for correlating, and therefore predicting, creep crack growth rates. If steady-state conditions are not maintained a new parameter must be used. This parameter, which we have called C_B, is the limiting value of the path dependent C integral, as the path collapses into the crack tip. A careful study of this parameter for a stationary crack shows how C_B can be estimated from known functions. However the effect of crack growth on C_B is not so easily treated.

INTRODUCTION

There is a well defined need in industry for reliable procedures which can be used to access the remaining life of structural components. Large structures, such as the pressure vessels which are used in the petrochemical and power generating industries, may contain stress concentrators such as holes, abrupt changes of section, and cracks. These may either be present from the beginning of service or developed later due to microstructural damage. It has long been known that design and residual life assessments based solely on uniaxial test data may be considerably in error. This is because the transient behaviour which results from the redistribution of stresses introduced by geometrical discontinuities has a marked effect. In particular, many materials may not have adequate ductility to allow for a complete stress-redistribution. Instead, cracks are developed which, if allowed to propagate can cause catastrophic failure. Therefore considerable effort has been devoted to characterizing the slow growth of cracks during creep using fracture mechanics parameters (or at least the framework of fracture mechanics). The stress-strain field which is developed ahead of a crack (or a notch) cannot be uniquely characterized by a single parameter throughout the life of a structure. Therefore, laboratory data very often shown contradictory results regarding correlation of crack growth with any given fracture mechanics parameter. The growth rates observed from a single geometry may correlate well with some of these parameters. However correlation for a range of geometries (the true validity test for any parameter) is generally poor. In addition, one must question the use of this approach due to uncertainties arising from scatter in the materials data, and the utility of short-term laboratory tests for estimating long term behaviour. Consequently alternative approaches have been investigated. These involve models for material degradation at the microstructural level. However such studies are not sufficiently advanced to provide a reliable procedure for life assessment. In particular, they are hampered by a lack of understanding of the time dependent stress-strain field ahead of a crack in a creeping solid. It is therefore clear that a

much sounder understanding of the deformation fields ahead of creep cracks is of paramount importance.

Studies of this type for room temperature elastic-plastic fracture mechanics have recently met with considerable success. However very few studies have been carried out for creep. On the other hand some of the most promising crack tip parameters in low temperature plastic fracture mechanics have not been explored for high temperatures. This is partly due to the experimental difficulties introduced by raising the temperature. This is leading to increased emphasis on numerical analysis.

For any fracture mechanics parameter to prove useful in the assessment of creep crack growth, it should satisfy certain criteria. Among these are:

i) The parameter must provide a measure of the stress-strain state in the vicinity of the crack tip.

ii) The correspondence between the crack growth rate and the parameter, should be independent of the specimen geometry and/or initial crack length.

iii) The parameter should be obtainable from global measurements, or failing this, from local measurements near the crack tip, by means of numerical anlaysis.

iv) From the computational viewpoint the parameter must be insensitive to finite element modelling and to mesh size.

In the first part of this report, the time dependent stress-strain fields ahead of a stationary crack in a creeping solid are investigated. A parameter which meets the above requirements is developed. Moreover, an approximate analytical formulation is developed, which allows the parameter to be estimated at any stage of creep, without the need to repeat the numerical analyses for each case.

Parts II and III are concerned with methods to assess the remaining life of structures containing flaws. One such method involves removing service-exposed material, and determining the state of damage and its remaining creep ductility. We show that if this can be done, the rate of crack growth can be determined. In Parts II, we show that for 2¼ Cr-1 Mo

steel, tested following a simulated heat-affected zone heat treatment, damage is controlled by the effective strain. From this, a method of estimating the critical effective strain required for crack advance is determined. In Part III, we use this data in a computational model, to determine the crack growth rate. The results are compared with experimental creep crack growth data for 2¼ Cr-1 Mo steel.

PART I

THE APPLICATION OF FRACTURE MECHANICS CONCEPTS TO THE CREEP REGIME AND TIME DEPENDENT STRESS-STRAIN FIELDS AHEAD OF A CRACK

1. Introduction

There is considerable interest in applying the concepts of fracture mechanics (or at least its framework) to the growth of cracks in creeping solids. Some high strength, creep resistant alloys (e.g. most nickel base superalloys) tend to be creep-brittle. Thus, there is only a small zone of creep relaxation ahead of the crack tip, and the crack aspect ratio $\Delta a/\Delta\delta$ tends to be very large (where Δa is the crack extension resulting from a given increment of crack opening displacement $\Delta\delta$). Under these circumstances crack growth rates can be expected to correlate well with the linear elastic stress intensity factor, K. (Siverns and Price, 1973; Neate and Siverns, 1973), at least for the most constrained specimen geometries.

At the opposite extreme, ductile materials, especially when tested with specimen geometries which produce a low degree of constraint, can develop creep zones ahead of the crack tip, extending right across the remaining ligament of the structure. In this case, crack growth rates may correlate with the net section section stress, σ_{net}, or a reference stress if bending is present (Harrison and Sander, 1971; Nicholson and Formby, 1975; Taira and Ohtani, 1977).

For most situations of practical interest, however, neither of these extreme situations is applicable. Cracks propagate in a "quasi-brittle" manner, in which a creep deformation zone is developed ahead of the crack to a sufficient extent that the elastic stress field no longer controls events at the crack tip. A new parameter capable of characterizing this stress field is required. For this situation, an approach has been developed by analogy to the J-integral method at low temperatures. The first formulation of this type is due to Goldman and

Hutchinson (1975) who developed an expression for J (later renamed C*), the energy production rate for steady-state creep,

$$C^* = \int_\Gamma \left(W^* \, dx_2 - \sigma_{ij} \frac{\partial u_i}{\partial x_i} \right) ds \tag{1}$$

Here W^* is the strain energy rate density $\int \sigma_{ij} \, d\dot{\varepsilon}_{ij}$, and u_i is the displacement rate. The integral is evaluated along a path Γ, which starts at one surface of the crack and moves through the material surrounding the crack tip to the opposite face of the crack. Under steady-state conditions, this integral should be path-independent, as is the J-integral under rate-insensitive conditions.

A data reduction scheme for experimentally determining C* has been developed by Landes and Begley (1976, 1980), while other methods have also been developed (Harper and Ellison, 1977; Haigh and Richards, 1972), as outlined previously (Wilkinson, 1981). All of these methods are based on the concept that C* is an energy rate integral, a notion which has recently been challenged (Atluri, 1982; Stonesifer and Atluri, 1982). However, if we accept these ideas then we can write (under steady-state conditions)

$$C^* = - \frac{1}{B} \frac{\partial U^*}{\partial a} \tag{2}$$

where B is the specimen thickness, and U^* is the rate of potential energy production in the specimen, i.e.

$$U^* = \int_0^{\dot{\Delta}} P \, d\dot{\Delta} \tag{3}$$

Here P is the applied load and $\dot{\Delta}$ is the load point displacement rate. In this way C* can be estimated using measured values of $\dot{\Delta}$. Much of the available experimental data seems to show better correlation with C* than with other parameters. However, the degree of experimental scatter is generally large.

From this brief survey, some initial conclusions can be drawn. First, there is no single fracture mechanics parameter which adequately correlates creep crack growth data for all materials and geometries. Second, the suitability of a given parameter will depend on the

brittleness of the material, and on the test geometry. Brittleness is a function of material processing prior to service. It may also change during service due both to long term aging at evaluated temperatures, and to the effect of distributed cavitation and microcracking on ductility.

We must also realize that the stress fields surrounding a crack are also time-dependent -- whether or not the crack propagates. This again affects the correlation of crack growth with fracture mechanics parameters. We therefore need to question the applicability of accelerated laboratory tests to the estimation of long term behaviour of large structures.

These are not new issues in materials engineering. The main purpose of a fracture mechanics approach to structural design is to enable us to estimate the behaviour of a structure containing flaws, based on laboratory tests, in which the geometry is very much different. Fracture mechanics provides a method for extrapolating from one situation to the other, provided the parameter we use to measure "toughness" is independent of geometry. In the analysis of creeping structures, there is a long established need to extrapolate from short term tests to long time service. While this can be done only with great care, and with a considerable level of uncertainty, there are now well established procedures for accelerated creep tests. These are used increasingly to estimate the remaining life of structures (Cane, 1982; Neddham and Cane, 1983).

In dealing with creep crack growth, we need to combine these two forms of extrapolation through geometry and time. This is not a straightforward task. However, there is reason to believe (as this report will show), that fracture mechanics can be usefully applied to creeping structures, to obtain estimates of residual life and for safety assessment of crack structures.

2. Time Dependence of Crack Tip Fields

The initial response of a cracked specimen, upon application of a load and for some time after, is essentially elastic. During this initial period creep strains are negligible

everywhere (i.e. less than the elastic strains), except in the immediate vicinity of the crack tip. This is analogous to the small-scale yielding situation at low temperatures and K provides an adequate description of the crack tip stress-strain field, i.e.

$$\sigma_{ij} = \frac{K}{\sqrt{(2\pi r)}} f_{ij}(\theta) \tag{4}$$

where r is the radial distance from the crack tip and f_{ij} contains angular dependence of the crack tip strain field.

The analytical studies of Rice and Riedel (1980), supported by numerical analyses (Bassani and McClintock, 1981; Stonesifer and Atluri, 1982) show that once a steady-state has been achieved, the stress and strain fields near the crack tip have an HRR-type singularity with an amplitude given by the path independent C* integral, i.e.

$$\sigma_{ij} = \left(\frac{C^*}{B I_n r} \right)^{\frac{1}{n+1}} \sigma_{ij}(\theta, n) \tag{5}$$

where σ_{ij} contains the angular dependence of the stress field, I_n is an integration constant and B is the material parameter is Norton's power law, i.e.

$$\dot{\varepsilon} = B\sigma^n \tag{6}$$

Between the two limiting situations of K and C* control lies a transition period in which creep strains are higher than elastic strains over an extensive region ahead of the crack tip. Throughout this transition, the C* integral is (by definition) path dependent (i.e. the value of C* integral will be dependent upon the contour over which it is evaluated). Thus neither C* nor K are valid parameters describing the stress-strain field ahead of the crack. If crack propagation commences before a steady-state is achieved, none of these parameters can be expected to provide adequate correlation of the crack growth rate.

The length of this transient period t_I (i.e. from initial loading to the development of a steady-state C* stress field), has been estimated by Rice and Riedel (1980). They start with an approximate estimate of the crack tip C- integral for short times, namely

$$C(t) = a_n \frac{(1-\nu^2)K^2}{(n+1)Et} \tag{7}$$

They then extrapolate this to the steady-state C* value to obtain t_T, i.e.

$$t_T = a_n \frac{(1-\nu^2) K^2}{(n+1) E C^*} \tag{8}$$

Here $a_n = 0.96$ for plane strain conditions. For plane stress, $a_n = 1.05$ and the $(1-\nu^2)$ is omitted. In addition, the integral is path-independent throughout the transition from K to C* controlled behaviour.

All of these analyses are strictly applicable, only to stationary cracks. The introduction of a moving crack greatly complicates the analysis. Even for room temperature fracture mechanics, there is as yet no complete description of the stress and strain fields for stable moving cracks. Several workers (Amazigo and Hutchinson, 1977; Dean and Hutchinson, 1980; Hutchinson and Paris, 1979; Rice et al. 1980) have shown that a milder stress-strain singularity than the HRR field (namely $(1/\ell n(r))$ may occur. For creeping materials Hui and Riedel (1979) have given results for quasi-static creep crack growth under small-scale yielding conditions. They report a new type of singularity which depends on the creep exponent n such that (for $n > 3$)

$$\sigma_{ij} = a_n \left[\frac{\dot{a}(t)}{B E r} \right]^{\frac{1}{n-1}} \sigma_{ij}(\theta, n)$$

$$\varepsilon_{ij} = \frac{a_n}{E} \left[\frac{\dot{a}(t)}{B E r} \right]^{\frac{1}{n-1}} \varepsilon_{ij}(\theta, n) \tag{9}$$

Thus, the amplitude of this singular field is related to the crack growth rate. This is a stronger singularity than due to HRR field. However according to Parks (1980), the stress singularity described by Hui and Riedel decays so rapidly with distance from the crack tip that this field may fail to dominate over any physically significant dimension.

In view of these and other uncertainties we have undertaken to analyse the time dependent variation of stress-strain field ahead of stationary crack using the finite element method (FEM). One primary interest is to understand the geometry dependence of the

transition period and the development of a crack tip parameter which characterizes the stress-field at any stage of creep independent of specimen geometry and crack size.

3. Finite Element Analysis

An incremental finite element program has been developed, following the small strain formulation of Kanchi et al. (1978). A detailed description of this formulation is given in Appendix 1. We have assumed mode I loading under plane strain conditions throughout. Fig. (1) shows the underformed mesh containing 134 8-node isoparametric elements. The a/W ratio was kept constant at 0.5. Three geometries are studied using this mesh. These are single-edge notched (SEN), double-edge notched (DEN), and centre-cracked plate (CCP). Because of symmetry, this mesh represents one-quarter of a DEN or CCP, or one-half of an SEN specimen. Traction-free boundary conditions are applied to the crack surface, while nodes ahead of the crack plane are restrained to remain in that plane. Those nodes on the appropriate vertical symmetry axis are also restrained to correctly model the DEN and CCP specimen geometries.

In our initial work, we wished to study the effect of crack tip blunting on the crack tip stress fields. This is necessary, to determine if the singular fields developed analytically for atomically sharp cracks are applicable to the real situation. This was done by placing a small ($r/a = 0.005$) semicircular hole at the crack tip. This was bounded by 12 equal-sized elements, thus giving 25 nodes at the tip of the crack. In later work, this hole was removed and the mesh refined from 134 elements to 204 elements. The crack tip was again modelled by 12 equal sized elements, but with one edge collapsed initially to zero length, and free to extend. On the remaining edges, the midside nodes remained at their usual positions. This crack tip mesh configuation is known to produce an HRR singularity for plastic solutions (deLorenzi and Shih, 1981).

The material is assumed to obey a constitutive equation for steady-state creep described Norton's power law,

$$\dot{\epsilon} = B\sigma^n \tag{6}$$

The parameters used in the analyses are the same as those used by Ehlers and Riedel (1980) and by Stonesifer and Atluri (1982), namely n = 5, B = 10^{-16} MPa^{-5}/hr, E = 150 GN/m^2 and v = 0.3. For each specimen geometry, the initial elastic stress intensity factor K_I was kept constant at 40 MN m$^{-3/2}$ by altering the applied loads accordingly. The loading was uniform and applied to ends of the specimens.

The method used to evaluate the C* integral is described in Appendix 2. At certain time intervals, the C(t) integral is calculated along six paths ahead of the crack tip using,

$$C(t) = \int_\Gamma \left| \left(\frac{n}{n+1} \sigma_{ij} \dot{\epsilon}_{ij} - \sigma_{11} \frac{\partial \dot{u}_1}{\partial x_1} - \sigma_{12} \frac{\partial \dot{u}_2}{\partial x_1} \right) dy + \right.$$

$$\left. \left(\sigma_{21} \frac{\partial \dot{u}_1}{\partial x_1} + \sigma_{22} \frac{\partial \dot{u}_2}{\partial x_1} \right) dx \right| \tag{10}$$

The integral paths chosen follow the edges of the elements. To do this the stresses and strain rates calculated at the integration points are extrapolated to the nodal points using a procedure developed by Hinton and Campbell (1974). The displacement rates appearing in eq. (10) are approximated using,

$$\dot{u}_{ij} = \frac{\Delta u}{\Delta t} \tag{11}$$

where Δu is the displacement increment during the time increment Δt immediately prior to the calculation of C(t).

4. Results

For all specimen geometries the initial elastic stress field ahead of the crack was kept constant by altering the magnitude of the applied loads. In each case, the elastic stress intensity factor calculated using an elastic finite element programme gave a maximum deviation of 0.96% from the desired value of 40 MN m$^{-3/2}$ and maximum variations between the paths of less than 1% (using the grid given in Fig. (1)).

The variation of the C integral with the time is shown in Figures 2 and 4 for the SEN, CCP and DEN geometries respectively. C(t) values are calculated along each of 6 paths whose distance from the crack tip is P. The normalized path distance d = P/c is also shown in the figures (c being the length of uncracked ligament). It is clear from these figures that the progressive development of the creep zone ahead of the crack causes convergence of C(t) values earliest for paths closest to the crack tip. Once C(t) has converged to the same result for all paths the calculations are continued for another 40 time steps. This ensures complete convergence of C(t) to a steady-state C*. The average values obtained from 6 integral paths are given in Table I. While values for the SEN and CCP values agree within 2% with tabulated values of Kumar and Shih (1981), the resulting value of C* for the DEN geometry is significantly higher than the tabulated one. For all geometries, the variation in C* between the paths at steady-state is less than 3% of their average value. The time to reach steady-state (defined as a variation between paths of less than 5%), is also a sensitive function of geometry (see Table I).

The progressive development of the creep zones with time are shown in Figs. 5 and 6 for the SEN and CCP geometries. The creep zone boundary is defined by the locus of points at which the equivalent creep strain is equal to the elastic strain (i.e. $\varepsilon_e = [2/3\ \varepsilon_{ij}\ \varepsilon_{ij}]^{1/2}$), not by some arbitrary constant strain. A linear interpolation of the plastic strains at the integration points was used to construct smooth boundaries. As the figures show the creep zones have a similar shape to the plastic zones found for small scale yielding conditions at low temperatures. It is clear that until the creep zone extends over the whole area of the uncracked ligament C* remains path dependent.

Figure (7) shows the time-dependence of the effective creep strains in the first element ahead of the crack tip (0.125 mm). This is computed by averaging all points lying between 0 and 15 degrees from the crack plane. The steady state displacement profiles of the cracks are given in Fig. 8.

To examine the influence of the remote deformation field on the strain distribution in the crack tip region, the circumferential variation of effective creep strain at a fixed distance from the crack tip is determined from the integration points. These results are shown in Fig. 9. The angle of maximum effective strain θ_m, is tabulated in Table I. Those for the SEN and DEN geometries are in reasonable accord with HRR field which predicts an angle of about 80°. For the CCP specimen the strains show a peak around 55° which clearly indicates a loss of triaxiallity associated with spread of creep deformation.

The resulting steady-state distributions are compared with the analytical HRR field in Figs. 10 to 12. For the SEN specimen, the numerical solution is in good agreement with HRR field over a distance of about 0.5 mm from the crack tip (or 5 δ where δ is the crack opening displacement). For the DEN specimen agreement is also good, but over a smaller distance than the SEN specimen. For the CCP geometry however there is no measurable distance over which the steady-state stress distribution agrees with the HRR field.

5. Discussion

Using finite element analysis, we have been able to examine the time dependent nature of the stress and strain fields surrounding the crack tip for stationary cracks. A number of important issues emerge.

The first is the degree to which the results are a sensitive function of geometry. We have kept the initial elastic K_I constant at 40 MPa $m^{-1/2}$. In the case of two of the geometries (CCP and DEN), the elastic compliance functions are essentially the same. Thus both K_I and the net section stress are held constant in this case. Despite this, the time to reach a steady-state C^* field varies greatly, as does the amount of creep deformation required. This raises several concerns. Because the time to reach steady-state varies so much with geometry, it is quite possible that, if one measures crack growth rates using different test specimens, one specimen may be characterized by a steady-state C^* field throughout most of the test, while for a second geometry steady-state is never reached. Moreover, even if laboratory tests are

carefully configured so that a steady-state is reached early in the tests, the data may not be applicable for estimating the life of a component which exhibits non-steady behaviour for much of its life. Finally since transient stresses near the crack tip are higher than at steady-state, data from steady-state crack growth experiments provide a non-conservative estimate of crack growth rate.

Regarding the absolute time for convergence, it is worth comparing our results with the estimate of Rice and Riedel (1980), given by eq. (8). The estimates from this equation, for the present conditions are given in Table I. They underestimate the time to reach a true steady-state by about one order of magnitude. One therefore needs to be careful when applying this estimate to the analysis of experiment data. This suggests that, under certain circumstances, crack propagation will commence before a steady-state stress field is established. This is discussed in more detail in Section III, in which the simulation of crack growth by finite element methods is discussed.

Figures 10 to 12 compare the computed stress field with the analytical HRR fields at steady-state. It is clear that the distance ahead of the crack for which the HRR field is valid, is specimen dependent. For the CCP specimen no correlation is found (Fig. 12). To investigate this further the mesh was refined to 204 elements with collapsed elements at the crack tip (as described earlier). However, the results obtained were no different from those obtained earlier. Thus it would appear that for the conditions tested, the HRR field is applicable at the crack tip in a CCP specimen, if at all,over a very small distance and over a much smaller region than for the SEN specimens. This raises the issue of validity criteria for C* testing. Such criteria have been suggested for J-integral tests (Begley and Landes, 1972). It can be shown that in order to ensure that an HRR field exists over a significant distance ahead of a crack tip, both the specimen thickness and the remaining ligament must exceed a critical value, which depends on $(J/\sigma_{ys})^2$. No such criterion has been suggested for creep crack growth tests. However something of this type is required if laboratory data are to be applied

correctly to the analysis of creeping structures, in which a different geometry may drastically alter the size of the HRR field.

We now turn our attention to the most important issue raised by this work. It appears likely that crack propagation occurs under transient conditions. We would like a parameter which characterizes the state of stress surrounding the crack tip during the K-to-C* transition period. For any crack tip parameter to be viable it must satisfy certain conditions, including the following:

i) The parameter must scale with the stress-strain state in the vicinity surrounding the crack tip.

ii) The response of the material (eg. failure load or crack growth rate) to any given value of the parameter, should be independent of the specimen geometry.

iii) It should be obtainable from global measurements, or, if this is not possible, from numerical methods.

iv) From a computational viewpoint the parameter must be insensitive to finite element modelling and to mesh size.

The C* parameter, acting as the amplitude of an HRR field appears to match these conditions once a steady-state stress field has been established. However, during the transient period, a different parameter is required. Ideally, this transient parameter should approach C* at steady-state.

A careful examination of the Figs. 2 to 4 indicates that due to the progressive development of the creep zones ahead of the crack tip, convergence of C(t) values to a path-independent value occurs earliest for paths close to the crack tip. We find that for all paths contained within the creep zone (i.e. the region in which creep strains are higher than elastic strains) the value of C(t) is path independent, within the accuracy of the numerical solutions (e.g. less than 2%). We have therefore investigated this limiting value of the C-integral, as a crack tip parameter. We have chosen to call this new parameter C_B. It is defined as

$$C_B(t) = \lim_{p \to 0} C(t) \tag{12}$$

where p is the path radius used in the calculation of C(t). Several values of $C_B(t)$ for each geometry are obtained by extrapolation of C(t) values to zero path radius. This is illustrated in Fig. 13 for the SEN geometry. It is clear that C(t) becomes path independent over a larger region with increasing time.

To test the validity of C_B as a crack tip parameter we have used it as the amplitude of the HRR field, and compared the stress distribution so obtained, with the finite element results. The results are shown in Figs. 14 to 16. The solid lines show the stress field given by

$$\sigma_{ij}(t) = \left[\frac{C_B(t)}{B I_n r} \right]^{\frac{1}{n+1}} \sigma_{ij}(\theta, n) \tag{13}$$

while the dashed lines are the finite element results. The initial elastic stress field is also shown, for comparison. It appears that C_B provides a reasonable correlation of the near stress fields during the transition period. It also appears that during the transition period the stress-strain field near the crack tip has a singularity of the HRR type. However the amplitude of this singularity is described by C_B. By its definition, eq. (12), C_B must reduce to C* once steady-state is established.

Figures 14 to 15 establish C_B as a valid crack tip parameter, according to condition (i) described above. However, the other conditions need to be satisfied. In particular, C_B is not easily obtained, since it requires a finite element analysis. We have therefore investigated the relationship between C_B, C* and t_s the time to reach steady-state for various geometries. Figure 17 shows the time dependence of C_B. Here, $C_B(t)$ is normalized by the steady-state C*, while time is normalized by t_s. By doing so, all the data, for all geometries fall on a single curve. Note, that the figure also contains data from the finite element calculations by Stonesifer and Atluri (1982) for a compact tension specimen (using the same material parameters). Since they used a different mesh geometry, this establishes, to a limited extent at least, the mesh-independence of C_B (condition iv).

Figure 17 indicates that C_B can be estimated from a knowledge of C*, and t_s. The first of these C*, can be calculated analytically, using the tabulated data of Kumar and Shih

(1981). All that is needed is the specimen geometry, the applied loads, and the creep characteristics of the material. However, we also need to know t_s, which is determined by finite element calculations.

As Table I indicates, there is a correlation between t_s and t_I, the transition time estimate of Rice and Riedel (1980). We therefore replot Fig. 17, using t_I as the normalizing parameter for time. This is shown in Fig. 18. Again, a single curve is found for all geometries. This can be represented by the equation

$$C_B(t) = C^* \left[1 + \left(r \frac{t_I}{t} \right)^s \right] \tag{14}$$

where

$$t_I = a_n \frac{(1-\nu^2) K^2}{(n+1) E C^*}$$

Since both C^* and t_I can be found analytically, Fig. 18 enables a determination of C_B using macroscopic parameters. It therefore conforms to condition (iii) outlined above.

Equation 14 provides a single equation fit to Fig. 18. However, it is considerably in error at $t = t_s$. A better result is provided by a two-equation fit, namely,

$$C_B = \begin{cases} C^* \left(r \frac{t_I}{t} \right)^s, & t < r t_I \\ C^* \qquad\quad , & t \geq r t_I \end{cases} \tag{15}$$

From Fig. 18, $r = 2.4$ and $s = 0.73$. The first of these parameters, r, is essentially the ratio of t_{ss}, the time at which the extrapolated transient C_B curve reaches C^*, and t_I, the transition time estimate. However this involves a slightly different definition of t_{ss}, than that used in the FEM analysis, where steady-state was determined by an arbitrary degree of path dependence for C. That definition results in higher values for t_{ss} and thus for r (see Table I). The physical meaning of s is not clear. However, it is probably a function of the creep exponent n. As n increases and the material becomes more brittle, we might expect C_B to approach the short time estimate of Rice and Riedel (1980), given by eq. 7, in which case $s = 1$. However, to verify this requires further finite element analysis for at least two different values of n.

These results establish C_B as a valid crack tip parameter for stationary cracks. It remains to be seen whether C_B may also prove useful in correlating the growth of creep cracks. This subject is addressed in Section III.

6. Conclusions

i) When creeping structures containing cracks are placed under identical initial elastic loading conditions, the time to approach a steady-state C* stress field and the amount of creep deformation required is a sensitive function of geometry.

ii) During the transition period the stress-strain field near the crack tip has an HRR singularity.

iii) The amplitude of this transient HRR field is described by C_B, a new crack tip parameter defined as

$$C_B = \lim_{p \to 0} C(t)$$

where p is the path radius for C(t).

iv) The parameter C_B describes the stress field ahead of the crack tip under transient conditions, as well as C* does during steady-state.

v) C_B equals C* once a steady-state is established.

iv) C_B can be estimated without recourse to finite element analysis, using eq. 15. It therefore meets the main conditions for a crack tip parameter. However, the ability of C_B to correlate creep crack growth data is not established by this study.

vii) A set of validity criteria should be introduced for creep crack growth testing which may be applied to both laboratory tests and the analysis of cracked components in service. These must ensure that the HRR field developed at any stages of creep exists over a significant distance from the crack tip.

7. References

Amazigo, J.C. and J.W. Hutchinson (1977), J. Mech. Phys. Solids, **25**, 81.

Atluri, S.N. (1982), Engg. Fract. Mech. 16, 341.

Bassani, J.C. and F.A. McClintock (1981), Intl. J. Solids Struc., 17, 479.

Begley, J.A. and J.D. Landes (1972), ASTM STP 514.

Cane, B.J. (1982), Intl. J. Press. Vess. Pip., 10, 11 (1983).

Christian, E.M., D.J. Smith, G.A. Webster and E.G. Ellison (1981), Proc. ICF 5, 1295.

Dean, R.H. and J.W. Hutchinson (1980), ASTM STP 700, 383.

deLorenzi and C.F. Shih (1977), Intl. J. Fract. Mech., 13, 507.

Ehlers, R. and H. Riedel (1980), Proc. ICF-5, 691.

Goldman, N.L. and J.W. Hutchinson (1975), Intl. J. Solids Struct. 11, 575.

Haigh, J.R. (1973), Mater. Sci. Engg. 20, 213.

Haigh, J.R. and C.E. Richards (1972), CERL Memorandum, No. RD/L/M461,

Harrison, C.B. and G.N. Sandor (1971), Engg. Fract. Mech. 3, 403.

Harper, M.P. and E.G. Ellison (1977), J. Strain Analysis, 12, 167.

Hinton, E. and J.S. Campbell (1974), Intl. J. Num. Methods Engg., 8, 461.

Hui, C.Y. and H. Riedel (1979), Brown University Report MRS E-117.

Hutchinson, J.W. and P.C. Paris (1979), ASTM STP 668, 37.

Kanchi, M.B., O.C. Zienciewicz and D.R.J. Owen (1978), Intl. J. Num. Methods. Engg, 12, 109.

Kumar, V. and C.F. Shih (1981), EPRI Report No. 1931/1237-1.

Landes, J.D. and J.A. Begley (1976), ASTM STP 590, 128.

Landes, J.D. and J.A. Begley (1980), ASTM, STP 700, 112.

McEvily, A.C. and C.H. Wells (1973), Proc. Intl. Conf. Creep and Fatigue in Elevated Temperature Applications.

Neate, G.J. and M.J. Siverns (1973), Intl. Conf. on Creep and Fatigue in Elevated Temperature Applications, Paper No. 234.

Nicholson, R.D. and C.L. Formby (1975), Intl. J. Fract., 11, 594.

Needham, N.G. and B.J. Cane (1983), ASME Intl. Conf. on Advances in Life Prediction Methods, 65.

Nicholson, R.D. and C.L. Formby (1975), Intl. J. Fract., 11, 594.

Parks, D.M. (1980), Proc. Second Intl. Conf. on Num. Methods in Fract. Mech., 239.

Rice, J.R., W.J. Drugan and T.L. Sham (1980), ASTM STP 700, 189.

Riedel, H. and J.R. Rice (1980), ASTM STP 700, 112.

Siverns, M.J. and A.T. Price (1973), Intl. J. Fract., 2, 193.

Stonesifer, R.B. and S.N. Atluri (1982), Engg. Fract. Mech. 16, 625.

Taira, S. and R. Ohtani (1973), Intl. Conf. on Creep and Fatigue in Elevated Temperature Applications, Paper No. 213.

Wilkinson, D.S. (1981), D.S.S. Report, Material and Design for Resistance to Crack Growth by Creep.

TABLE I

Finite Element Analysis of a Stationary Crack

Geometry	K_I (MPa.m$^{\frac{1}{2}}$)	C* (N/m/h)	t_s (h.)	t_1 (h.)	θ_m
SEN	40	213	117	7.29	78°
DEN	40	417	49.9	3.72	68°
CCP	40	1017	12.4	1.53	55°

Notes: t_s - time to reach steady-state in finite element analysis

t_1 - time to reach steady-state according to estimate of Riedel and Rice (1980), eq. (8)

θ_m - angle of maximum effective strain.

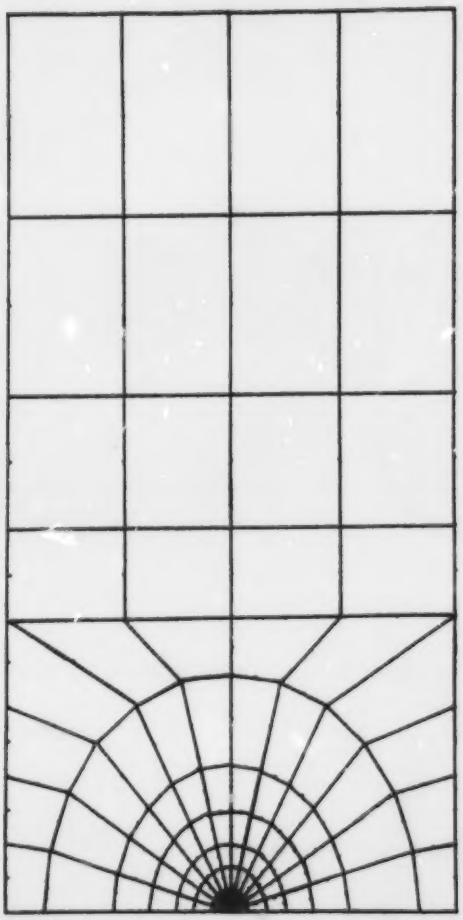

Fig. 1: The finite element grid used to determine the response of a stationary crack to mode I, plane strain loading.

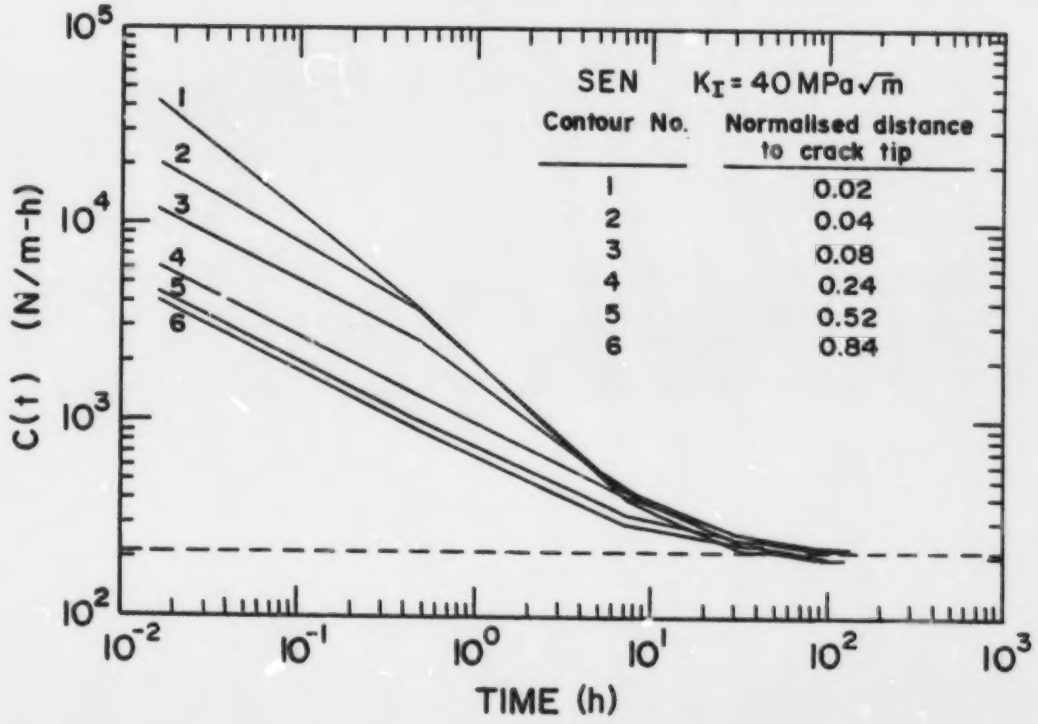

Fig. 2: The variation of C(t) with time and integration path for the SEN geometry.

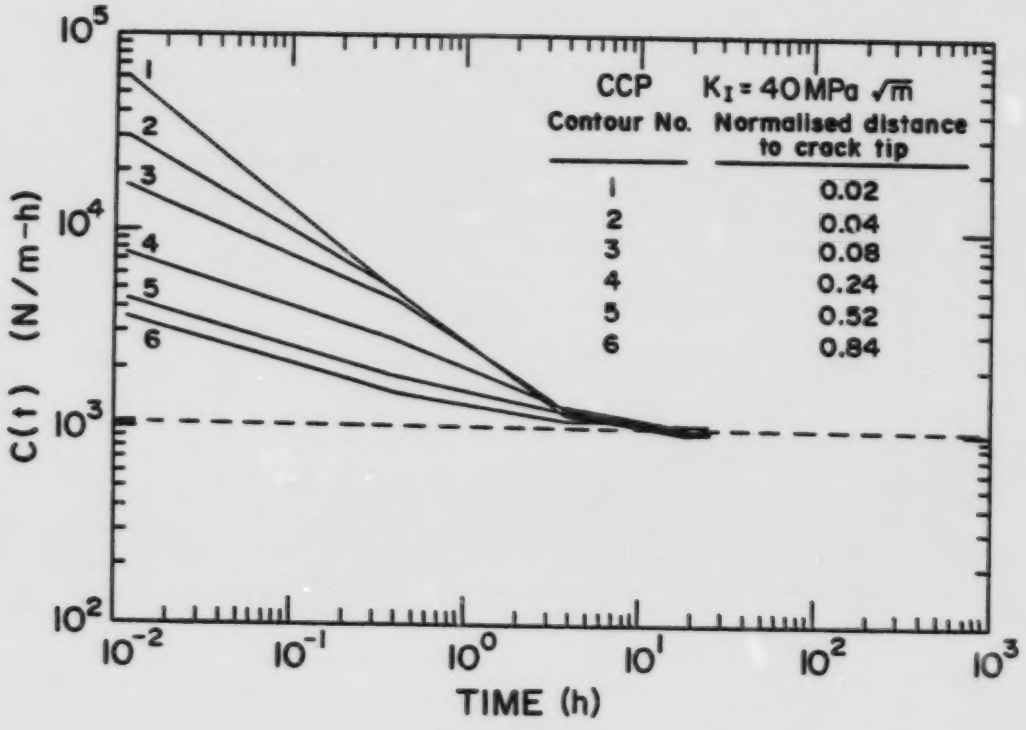

Fig. 3: The variation of C(t) with time and integration path for the CCP geometry.

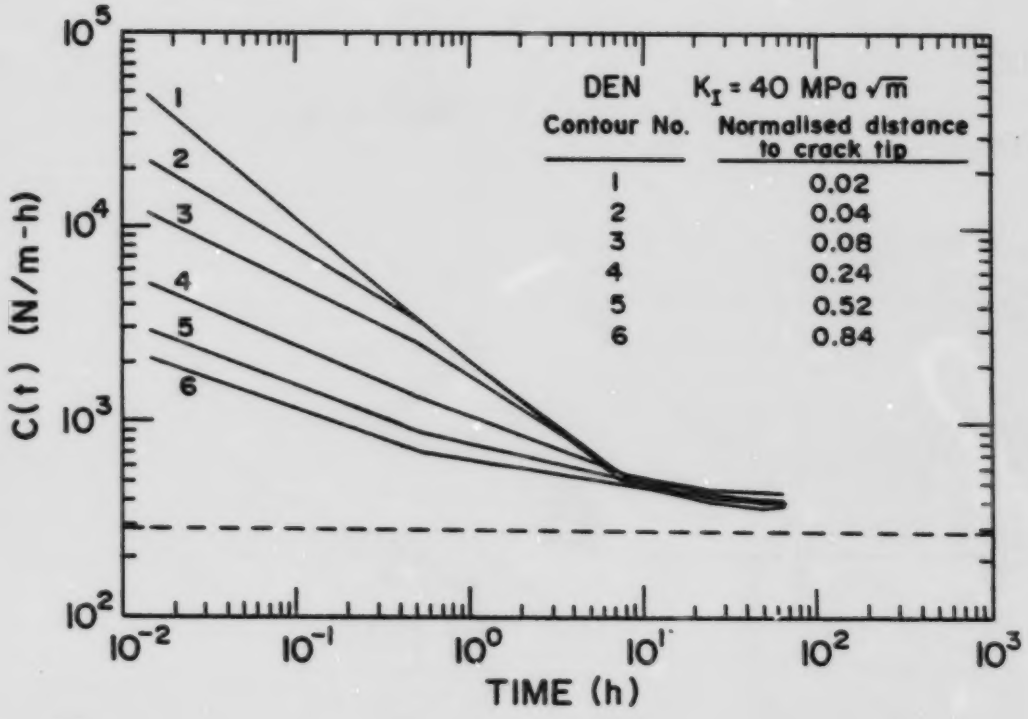

Fig. 4: The variation of C(t) with time and integration path for the DEN geometry.

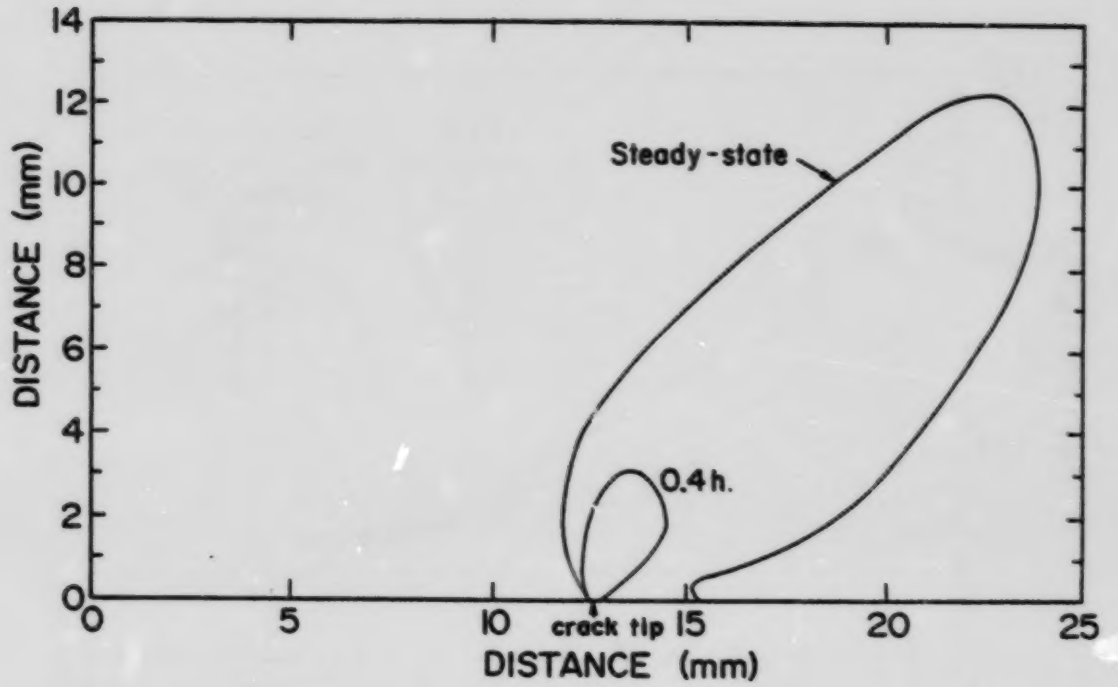

Fig. 5: The size of the creep zone, at different times, for the SEN geometry.

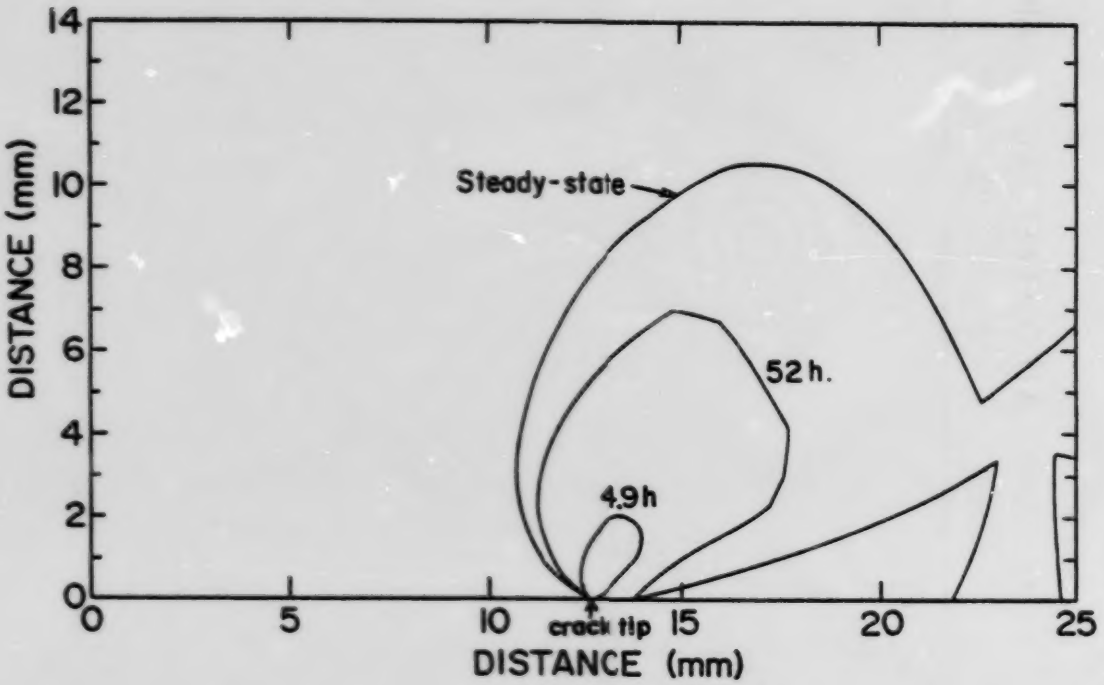

Fig. 6: The size of the creep zone, at different times, for the CCP geometry.

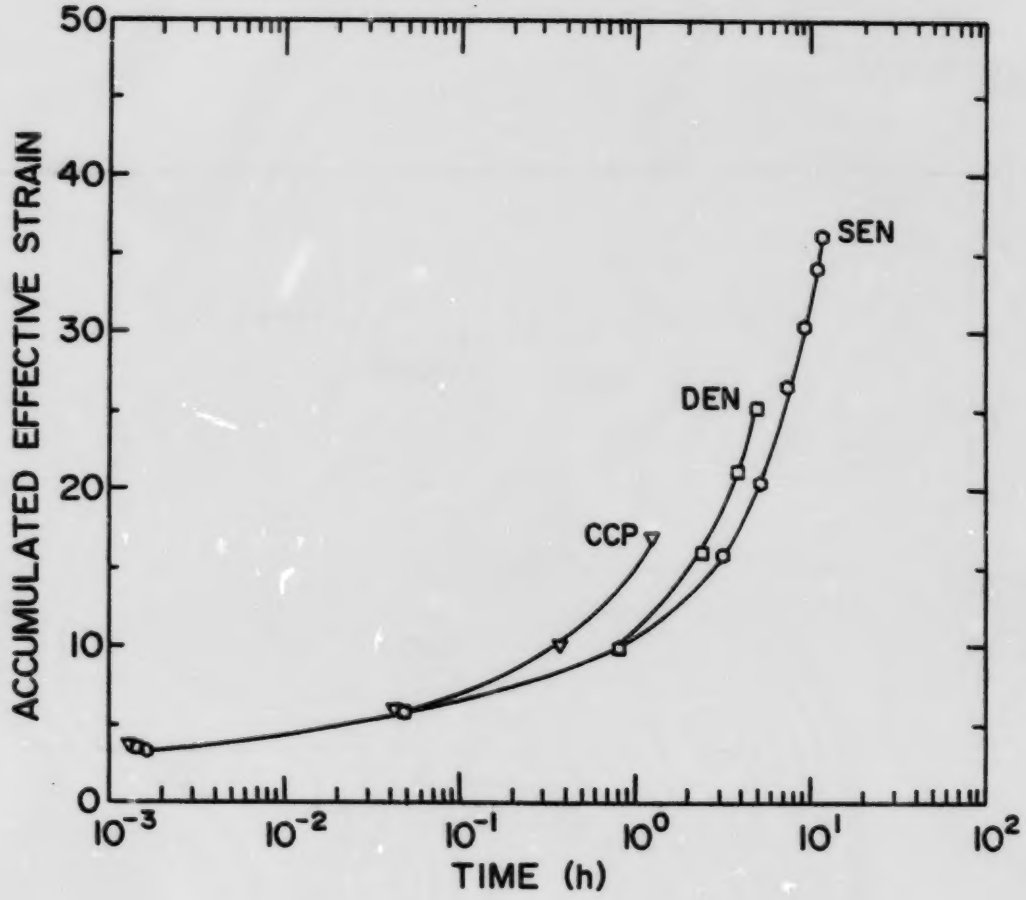

Fig. 7: The effective creep strain near the crack tip, as a function of time, for all three geometries.

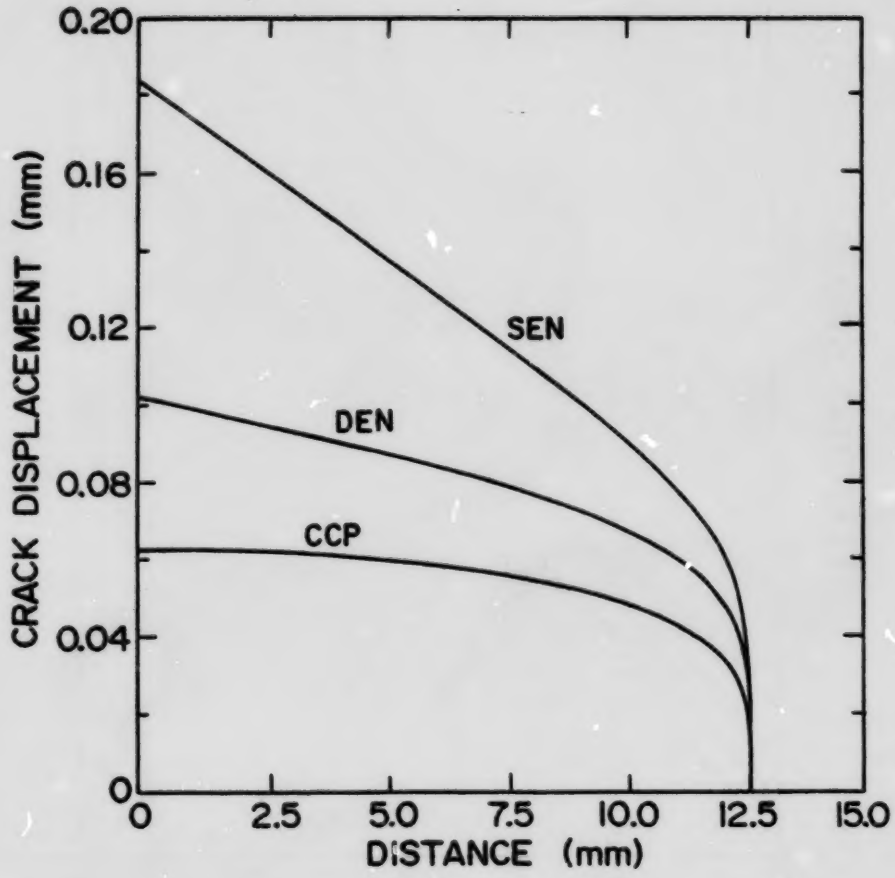

Fig. 8: The crack surface profiles, at steady-state.

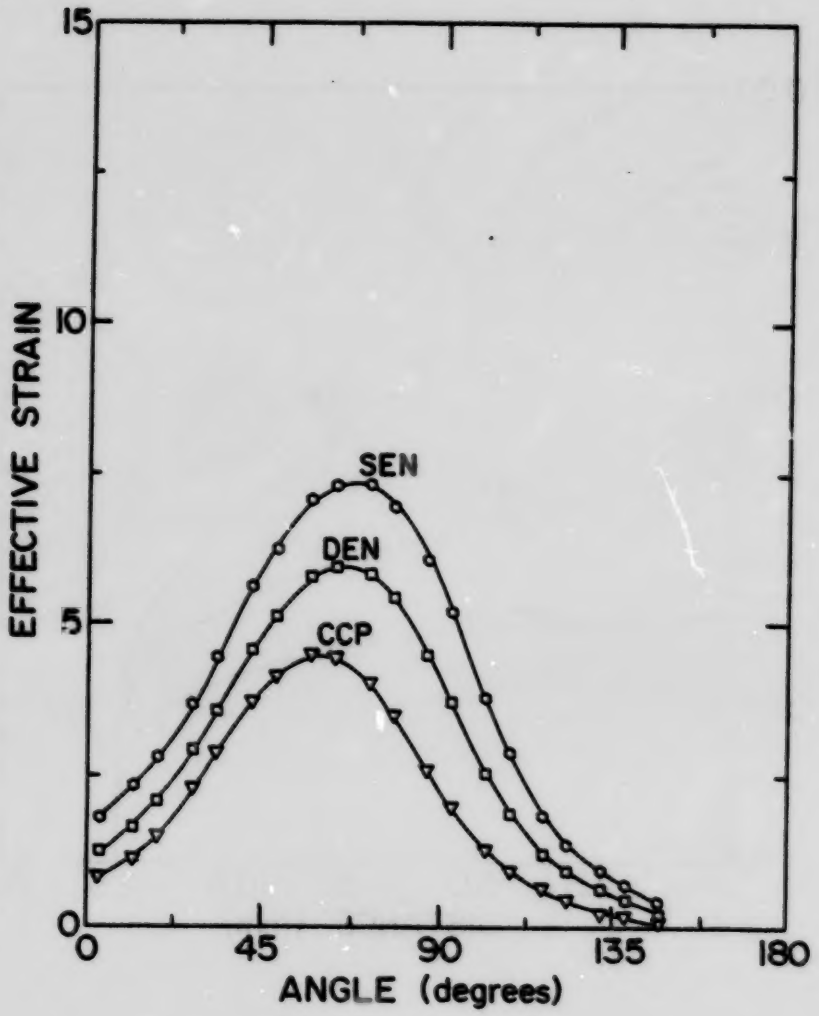

Fig. 9: The angular dependence of effective strain at a fixed distance ahead ot the crack tip.

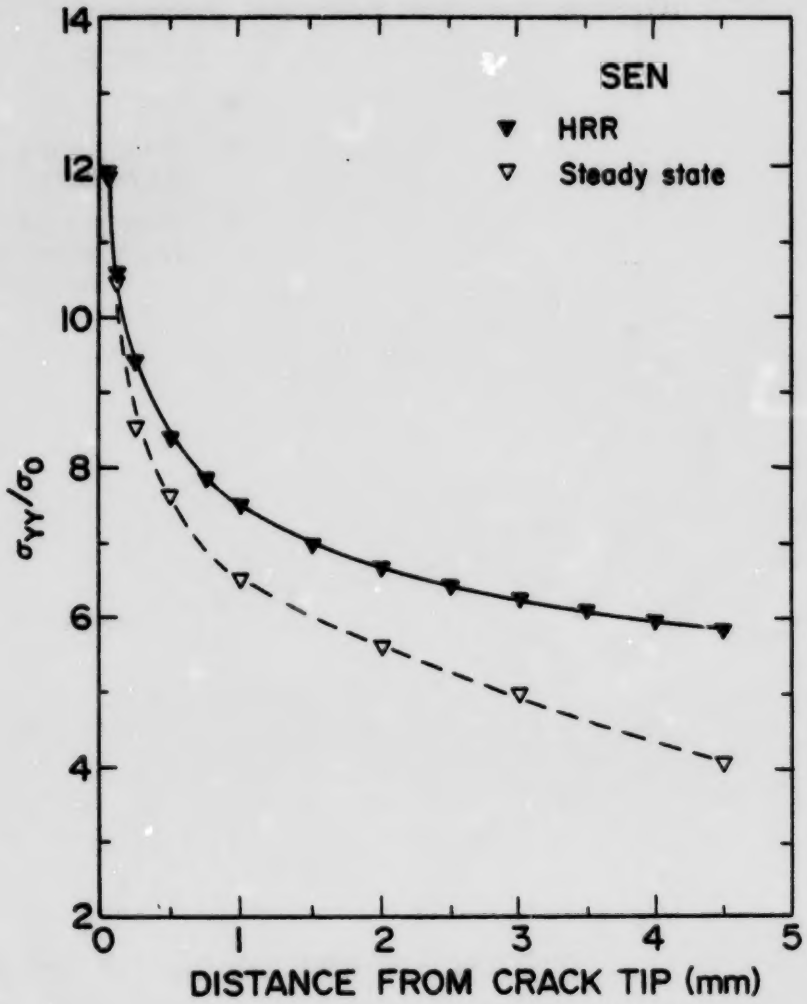

Fig. 10: A comparison of the finite element results (---) with the HRR field from eq. 5 (——), at steady state, for the SEN geometry.

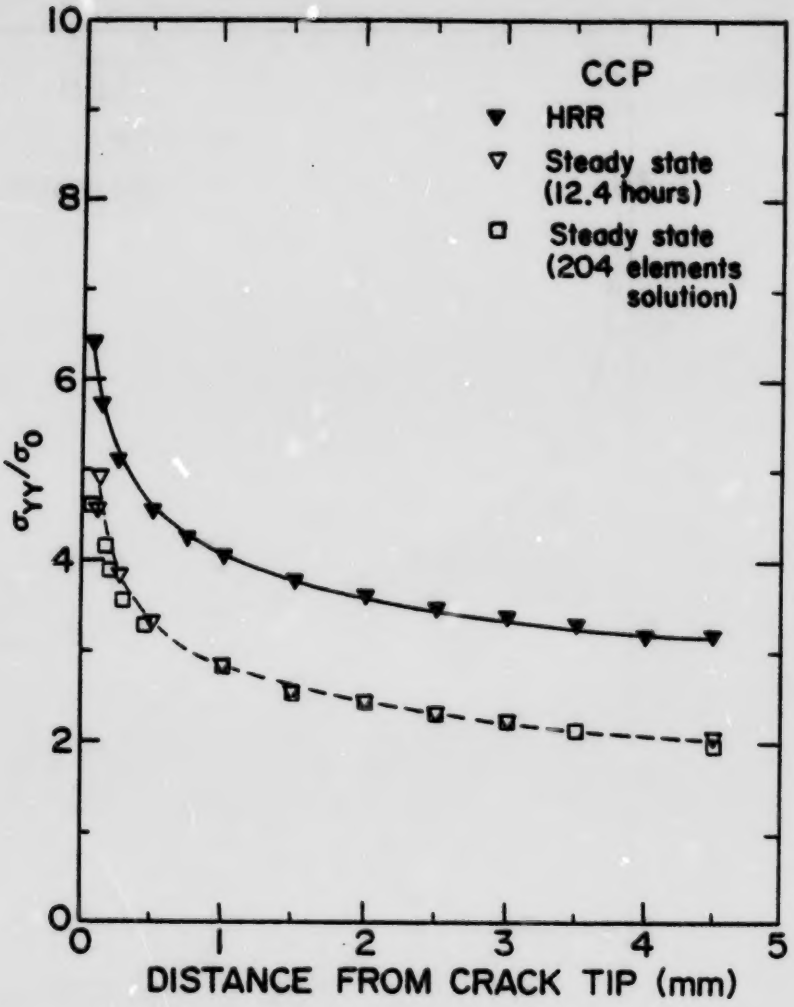

Fig. 11: A comparison of the finite element results (---) with the HRR field from eq. 5 (——), at steady-state, for the CCP geometry.

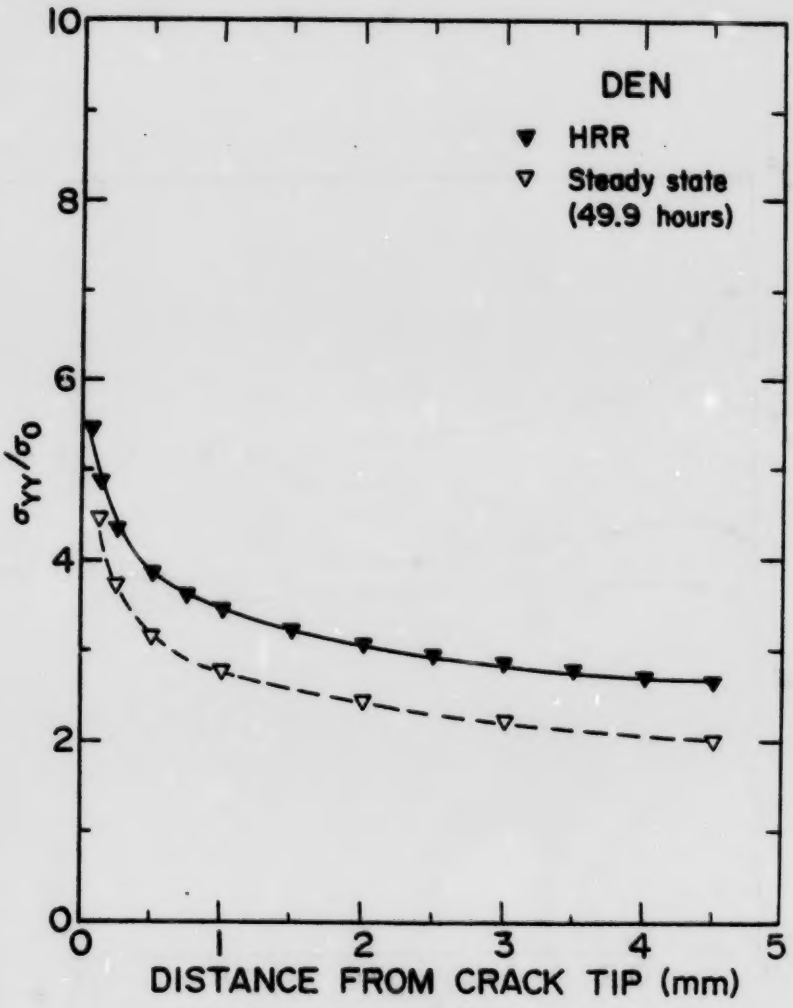

Fig. 12: A comparison of the finite element results (---) with the HRR field from eq. 5 (——), at steady-state, for the DEN geometry.

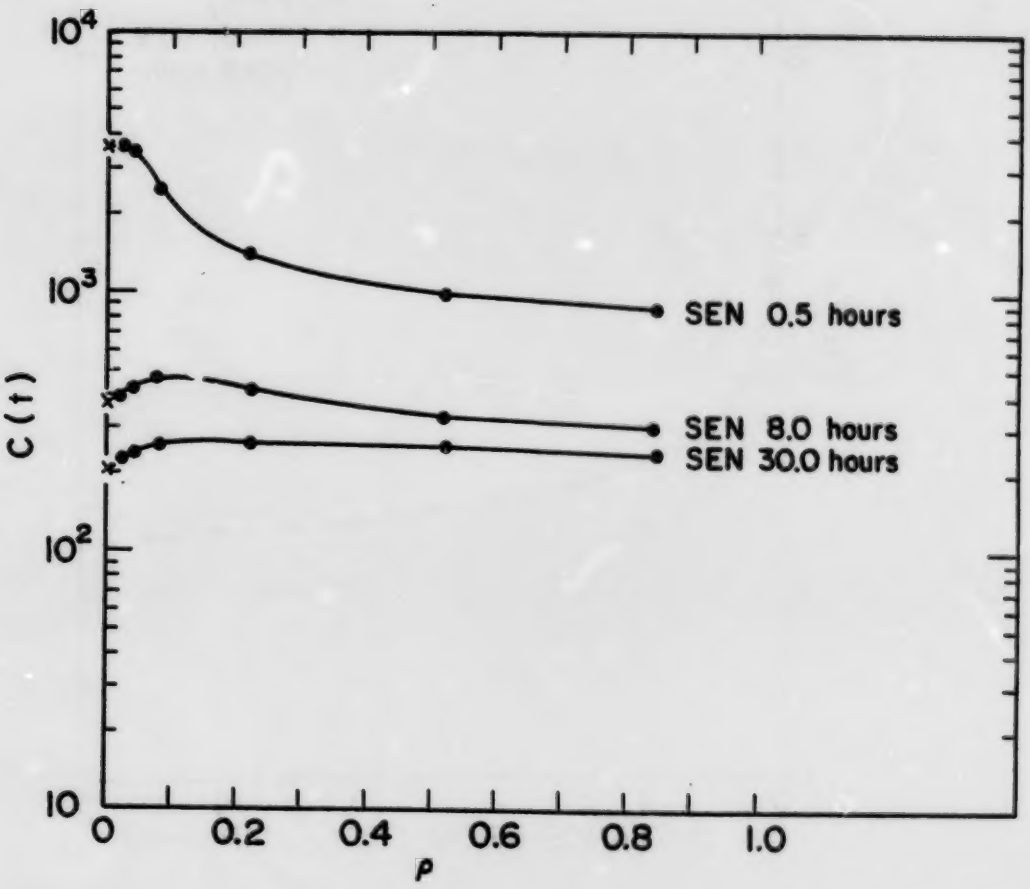

Fig. 13: The path dependence of the C-integral for the SEN geometry at various times. This illustrates the determination of $C_B(t)$.

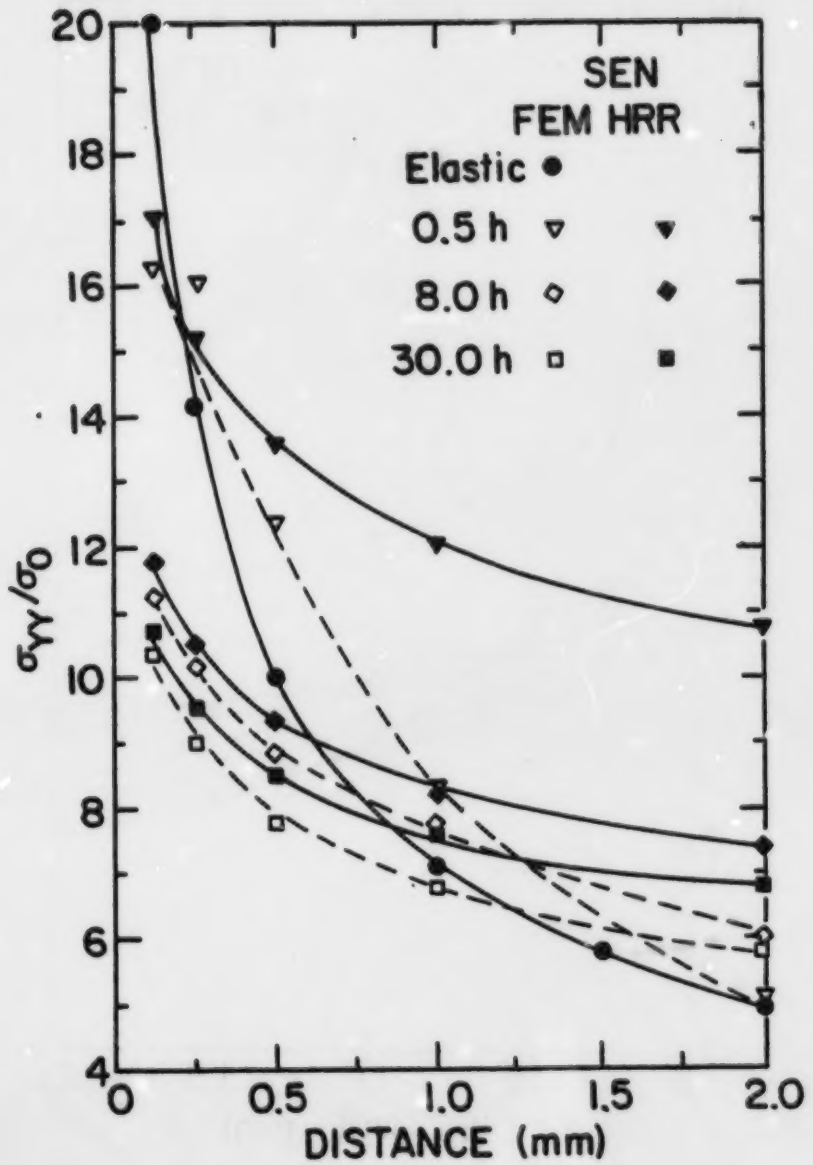

Fig. 14: A comparison of the transient finite element results (---) with the C_B-controlled HRR field from eq. 13 (——), for the SEN geometry.

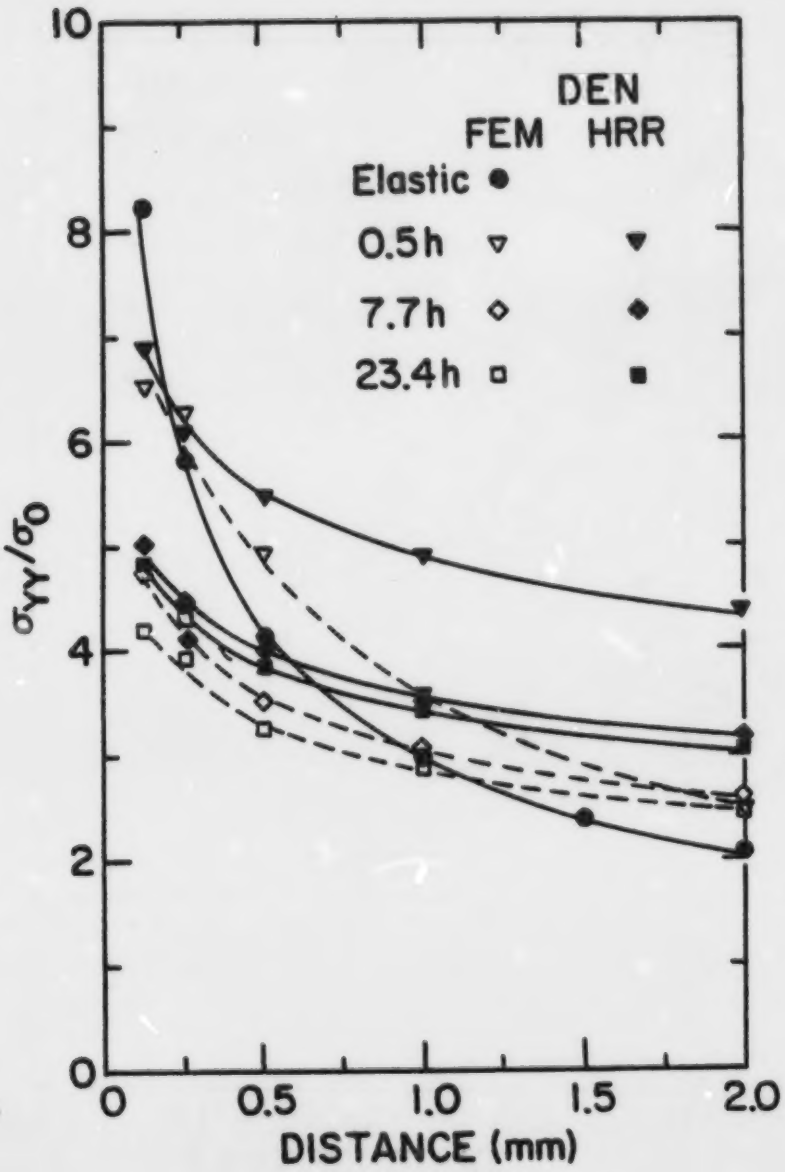

Fig. 16: A comparison of the transient finite element results (---) with the C_B-controlled HRR field from eq. 13 (——) for the DEN geometry.

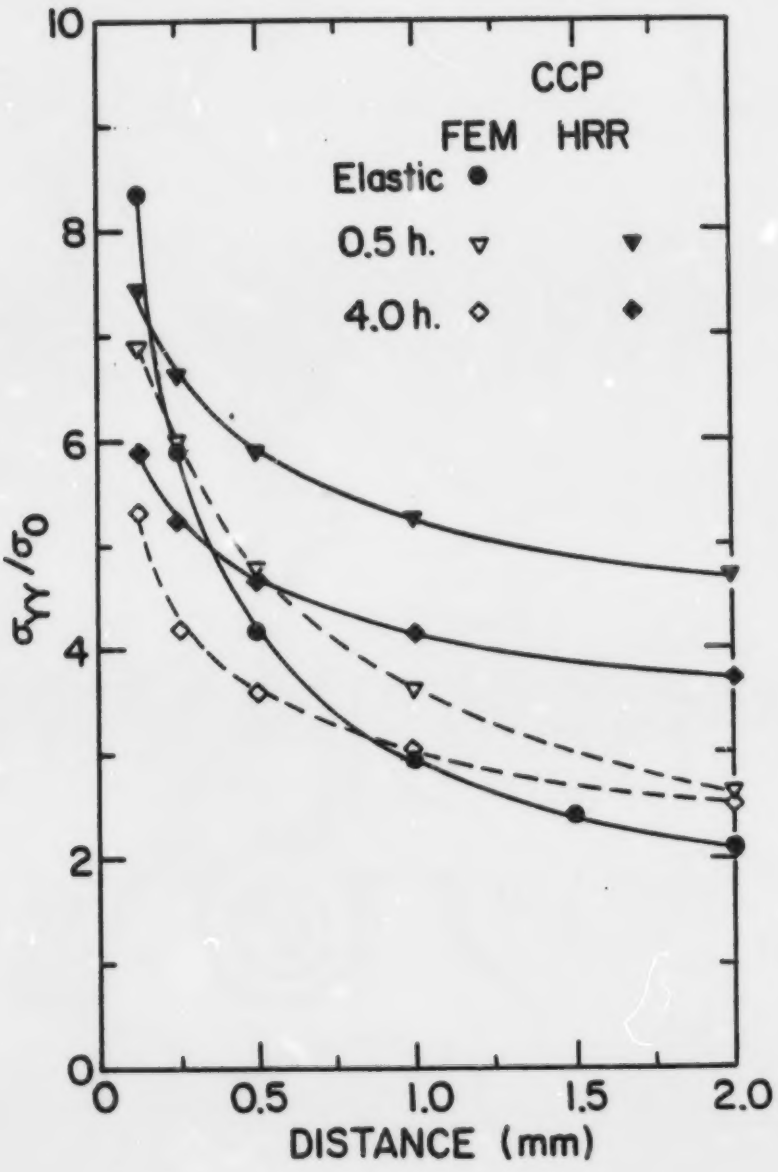

Fig. 15: A comparison of the transient finite element results (---) with the C_B-controlled HRR field from eq. 13 (——), for the CCP geometry.

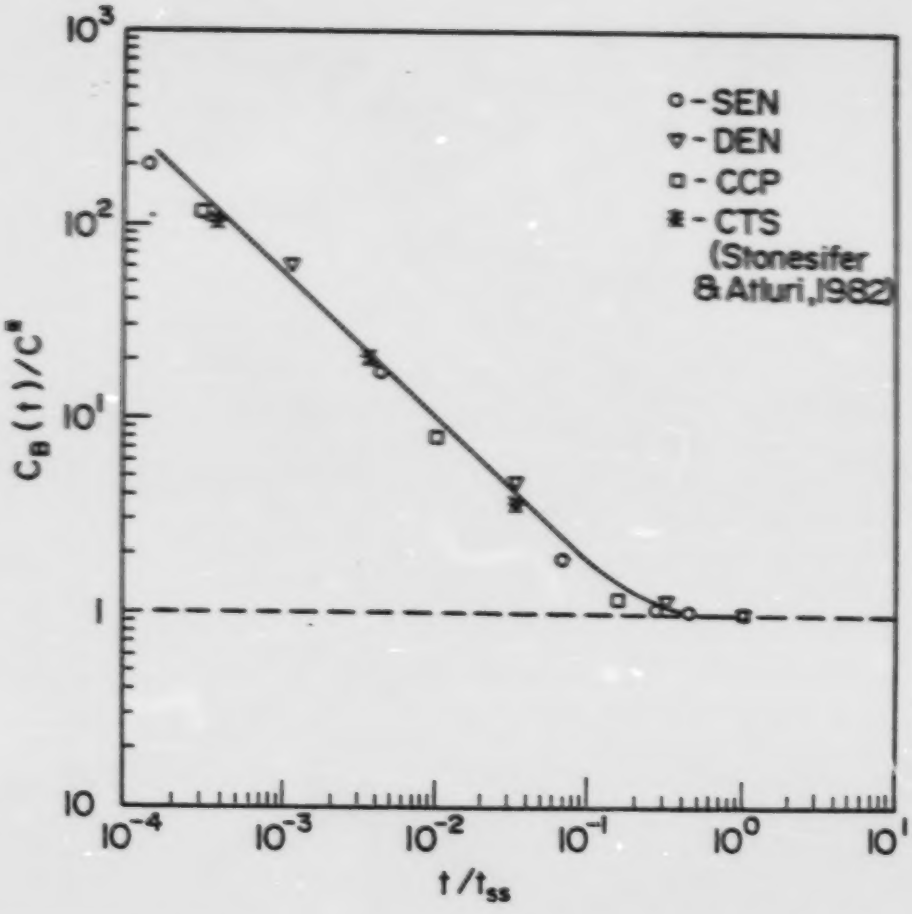

Fig. 17: $C_B(t)/C^*$ vs. t/t_s for four geometries. The data all lie on a single curve.

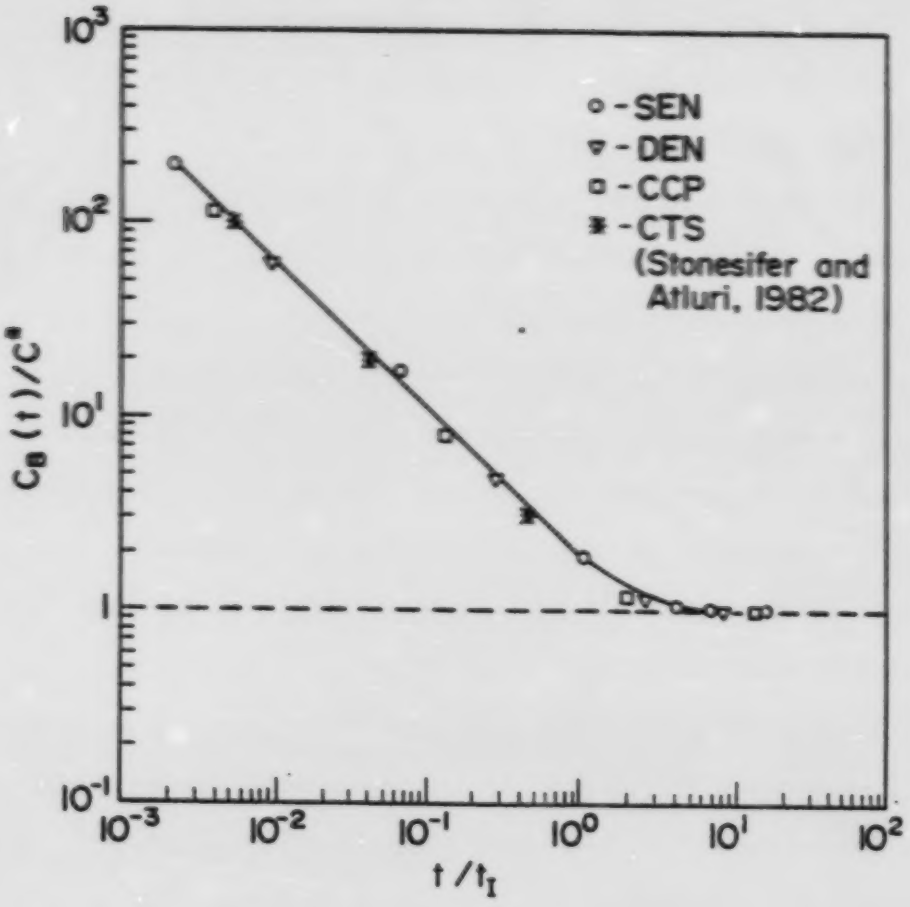

Fig. 18: $C_B(t)/C^*$ vs. t/t_I for four geometries. The data all lie on a single curve.

PART II

EXPERIMENTS ON THE EFFECT OF A MULTIAXIAL STRESS-STATE ON CREEP DAMAGE AND FRACTURE

1. Introduction

Creep fracture occurs by a process of cumulative damage. This involves the nucleation and growth of cavities, their subsequent linkage to form microcracks, the propagation and linkage of these to form a macrocrack, and the final growth of this macrocrack until failure. In a structure, the rate of damage accumulation is a function of the local loading history, temperature, and microstructure. This makes the estimation of remaining life in a complex structure difficult. One approach is to remove a sample of service-exposed material, from a critical region of the structure, and to determine the state of damage by microstructural observation (Needham and Cane, 1983), or by accelerated creep testing (Woodford, 1974; Hart, 1976).

The most widely used of these is the latter. There are several problems however. First, it is assumed that the material removed for sampling is representative of the most highly damaged material in the structure. Otherwise, remaining life is overestimated. Second, tests must be accelerated. This is generally accomplished by maintaining the same stress as in service (assuming this is known with reasonable certainty) and raising the temperature. The assumption here is that material aging processes are accelerated in the same proportion as creep damage. In this way, the length of an accelerated test t_{acc}, at temperature T_{acc}, is related to the remaining service life t_{serv}, at the service temperature, T_{serv}, by the Robinson (1952) rule,

$$\frac{t_{serv}}{T_{serv}} + \frac{t_{acc}}{T_{acc}} = 1 \qquad (1)$$

If assumptions upon which the Robinson rule is based are valid, then the creep ductility is not affected by accelerated testing. The rule can therefore be rewritten as

$$\varepsilon_{serv} + \varepsilon_{acc} = \varepsilon_{virgin} \tag{2}$$

where ε_{virgin} is the ductility of virgin material before service. Thus accelerated testing provides a measure of the remaining damage tolerance of the material.

Accelerated creep tests are invariably carried out under uniaxial tension. Since the state of stress in service is rarely uniaxial, this raises the question of the effect of stress state on creep rupture, and life prediction. This is also relevant to a discussion of damage accumulation in advance of a propagating creep crack. This is the subject addressed in this section. If creep fracture depends only on a certain component of the stress state or strain state, then accelerated uniaxial creep tests can still be used to determine the damage tolerance of the structure, under multiaxial loading. Moreover, they can be used to determine the resistance of the material to crack propagation, as compared with the resistance of virgin material.

A determination of the state of damage in a structure, and the rate of damage accumulation can be formulated either in terms of detailed mechanisms, or in terms of continuum damage parameters. Of these two, the former is most attractive in the long term, since it enables material behaviour to be predicted from well understood physical principles. However, the predictive abilities of available models is not yet of sufficient accuracy. Therefore, in the experimental work outlined below, we have used a continuum approach to damage assessment. Nonetheless, it is useful to start this discussion by first developing a proper framework for understanding the damage processes by discussing the physics of the cavitation process.

2. Models for Creep Damage

Cavity Nucleation

The nucleation of cavities has generally been given much less attention than cavity growth. An excellent review of available models has been produced by Goods and Brown (1979). Early theories of Greenwood (1952), later extended by Balluffi and Seigle (1955) were based on the concept that vacancies produced by plastic deformation condense on grain boundaries. Other theories (Davies and Wilshire, 1961; Chen and Machlin, 1956) are based on grain boundary sliding. Dislocation pile-ups, impinging on nondeformable particles and grain boundaries, have also been suggested as nucleation sites (Smith and Barnby, 1967). Although experimental evidence for such a dislocation mechanism has been proposed by Dyson et al. (1976), a direct application of this model is difficult, due to uncertainties in the extent to which grain boundary sliding and local diffusion reduces the build-up of stress-concentration (Goods and Grown, 1979). A model incorporating both bulk deformation and grain boundary sliding has been proposed by Gifkins (1956). According to this mechanism tensile stresses are developed at boundary steps due to grain boundary sliding. Once the boundary separates, dislocations within blocked slip bands run into the cavity nucleus, resulting in a stable cavity. This mechanism has been supported by others (Wear, 1959; Harris, 1965; Fleck et al., 1975; Argon et al., 1980).

Argon et al. (1980, 1982) have considered the nucleation of cavities during creep in considerable detail. They find that a high level of interfacial stress is necessary for decohesion at particles by the condensation of vacancies. According to their conclusions, a threshold stress of at least 10^{-3} E (where E is Young modulus) is required. Thus high stress concentrations must exist, at least for short periods of time. Such stress concentrations can be produced during creep by a stochastic process of grain boundary sliding around particles, setting up a high interfacial stress on particle interfaces.

Critical measurements of nucleation rates require observation of cavities at or close to their nucleation size. This is generally beyond most currently available sampling techniques.

Most observations of cavities occur after considerable growth has occurred. Therefore, the experimental data on the "nucleation" of the cavities are gathered from a quantitative assessment of cavity density at various stages of creep (Cane and Greenwood, 1975; Argon, 1982; Needham and Gladman, 1980). From these results it appears that for many materials, some cavities nucleate immediately upon the onset of deformation, and nucleation is continuous thereafter. However the rate of nucleation varies with time and strain (or stress). In some cases, there is evidence of the exhaustion of available nucleation. In addition, measurements of cavity density are affected by void coalescence at large strains. There is relatively little data on the role of stress-state on the nucleation of cavities.

Growth of Cavities and Damage Concepts

The growth of cavities has received considerable attention. The most refined current view (Cocks and Asbhy, 1981) is that cavity growth along grain boundaries can be controlled by at least three mechanisms. At low stress levels, which produce negligible deformation in the matrix, cavities grow with a "spherical shape" by diffusional flow along the grain boundaries. This process has been modelled in varying amounts of detail (Hull and Rimmer, 1959; Speight and Harris, 1967; Raj and Ashby, 1971). When cavities become larger or when surface diffusion is slow, the voids become crack-shaped, and their growth is controlled by surface diffusion (Chuang et al., 1979). If the applied stress is high enough or cavities are very large, significant deformation is produced in the matrix and cavities grow primarily by power law creep (Edward and Ashby, 1979; Cocks and Ashby, 1980; Beere and Speight, 1978). In most cases cavity growth occurs by a combination of power-law creep and diffusional flow (Cocks and Ashby, 1980; Beere and Speight, 1978; Needleman and Rice, 1980). We start by considering the growth of voids by boundary diffusion. In this case, atoms diffuse out of the growing void and plate onto the grain boundary as shown in Fig. (1-a). The void growth rate can be expressed as (Cocks and Ashby, 1981)

$$\frac{dv}{dt} = \frac{2\pi D_B \delta_B \sigma_1 \Omega}{kT} \frac{\left(1 - \frac{r^2}{\ell^2}\right)}{\ell n\left(\frac{\ell}{r}\right)} \tag{3}$$

where

$2r$ = hole diameter

2ℓ = hole spacing

D_B = grain boundary diffusion coefficient

δ_B = grain boundary thickness

Ω = atomic volume

k = Boltzman constant

T = temperature

σ_1 = remote applied tensile stress.

If the area fraction of holes f_h is defined as,

$$f_h = \frac{r^2}{\ell^2} \tag{4}$$

and the jacking effect of diffusional plating is included, then the rate of damage accumulation df_h/dt can be written as

$$\frac{df_h}{dt} = \frac{\Phi_0 \sigma_1}{f_h^{1/2} \ell n\left(\frac{1}{f_h}\right)} \left(\frac{\dot{\varepsilon}_o}{\sigma_o}\right) \tag{5}$$

where

$$\Phi_0 = \frac{2 D_B \delta_B \Omega}{kT} \ell^3 \frac{\sigma_o}{\dot{\varepsilon}_o} \tag{6}$$

and ($\dot{\varepsilon}_o$ and σ_o) are material parameters, defined by Norton's power law.

When surface diffusion is slow, atoms flow out from the equator of the voids, causing it to become flatter and more crack like (Fig. 1-b). This type of growth mechanism has been investigated in detail by Chuang et al. (1981). The rate of damage accumulation is now

$$\frac{df_h}{dt} = \frac{\Psi_o f_h^{1/2}}{(1 - f_h)^3} \left(\frac{\sigma_1}{\sigma_o}\right)^3 \tag{7}$$

where

$$\Psi_o = \frac{1}{2} \frac{D_S \delta_S \Omega \sigma_o^3}{k T \gamma_S \dot{\varepsilon}_o} \tag{8}$$

D_S = surface diffusion coefficient

δ_S = thickness of layer of material in which diffusion takes place

γ_S = surface free energy.

The growth of voids by power-law creep is illustrated in Fig. (1-c). The shaded area containing the void extends at a rate determined by the net section stress $\sigma_e/(1-f_h)$ (where σ_e is the effective stress). The remaining volume deforms at a rate determined by σ_e. The rate of cavity growth is then given by

$$\frac{d f_h}{dt} = \beta \left[\frac{1}{(1-f_h)^n} - (1-f_h) \right] \left(\frac{\sigma_e}{\sigma_o} \right)^n \dot{\varepsilon}_o \tag{9}$$

For uniaxial tests, $\beta = 0.6$, while in general

$$\beta = \sinh \left[2 \frac{(n-1/2)}{(n+1/2)} \frac{\sigma_m}{\sigma_o} \right] \tag{10}$$

where σ_m is the hydrostatic stress.

Under certain conditions, two mechanisms can be expected to contribute significantly to the growth of cavities. Considerable effort has been devoted to this problem. However, as Cocks and Ashby (1981) have shown, a solution based on the simple addition of the damage rates for the individual mechanisms is sufficiently accurate for most purposes.

Discussion

Models of the type just discussed can be incorporated into a theory for the propagation of cracks by cavitation. Considerable progress has been made in this area for the case of a steady-state crack tip stress field (Vitek, 1978; Wilkinson, 1981; Wilkinson and Vitek, 1982). Recently, this work has been extended to certain types of transient stress fields, including the C_B-controlled field developed in the previous section (Wilkinson, 1984). All of these models enable a prediction of the crack growth rate, given a knowledge of the dominant cavity growth

mechanism, and the controlling stress field. However, in general, there is insufficient data for these models to provide an accurate assessment of remaining life.

As noted earlier,it is not our intention to use these models as a basis for predicting creep crack growth rates. However, they do offer some insight into the effect of stress state on damage accumulation. First consider cavity nucleation. All of the mechanisms considered, even those involving vacancy condensation, are ultimately controlled by the rate of deformation in the bulk material. Cavity nucleation should therefore be controlled by the equivalent stress σ_e or equivalent strain ε_e, as it is at ambient temperature.

Cavity growth by power law creep is also controlled primarily by the equivalent stress, although the mean stress also plays a role. Diffusion-controlled cavity growth, in contrast, is controlled by the normal traction σ_1 acting across the grain boundary.

Depending on the material and test conditions used, we may therefore expect fracture to be controlled either by the normal stress σ_1 or the equivalent stress σ_e. This view has been proposed by several authors (Dyson, 1976; Dyson and McLean, 1977; Cane, 1980; Pandey et al., 1982).

We have therefore carried out an experimental study to determine which component of the stress (or strain) state controls the rate of damage accumulation in a coarse-grained 2¼ Cr-1 Mo steel. This investigation is described next.

3. Experimental

Material and Heat Treatment

The material used for this study was a commercial heat of 2¼ Cr-1 Mo steel. It was received in the form of a 3 inch thick hot rolled plate. Blanks were cut from the plate parallel to the rolling direction. These were homogenized at 1300°C for 40 minutes and water quenched, then tempered at 700°C for four hours. This heat treatment provided a fully bainitic structure with a large prior austenite grain size, representative of the coarse-grained region of a weld, heat- affected zone. All heat treatments were carried out in air. The

tempering characteristics after heat treatment are shown in Fig. (2). The grain size measurements were carried out using a linear intercept method and prior austenite grain size was found to be 190 ± 90 μm.

Test Specimen Geometry

In order to impose different levels of hydrostatic stress and constraint three different specimen geometries were used. These are the smooth uniaxial tensile, notched tensile, and plane-strain tensile geometries. The details of the specimen geometries and dimensions are given in Fig. (3).

Creep Tests

Creep tests were performed at 550°C in an inert atmosphere using a Dennison constant load creep machine. Except for the plane-strain tensile specimens, the axial displacement of the gauge length was monitored continuously using an extensometer connected to the shoulders of the specimens. The temperature was monitored with three thermocouples attached to the specimen. The difference in thermocouple readings was kept less than 5°C. The thermocouple attached to the mid section of the specimen was recorded as the test temperature. This was kept at 550°C ± 1°C.

Some samples were tested to failure. Others were interrupted prior to failure, to enable the progressive accumulation of damage to be monitored. This was accomplished by breaking interrupted samples using impact loading in liquid nitrogen. This produced a grain boundary fracture surface for damage analysis.

Quantitative Determination of Grain Boundary Cavitation

Fractured samples were examined in a Phillips scanning electron microscope. Quantitative studies were performed by surveying a specimen at a magnification of 5000 x. A contrast enhancement device on the microscope was used for some of this work. By drastically

altering the white and black levels of the image, pictures were obtained which could be used with an OMNIMET image analyser to determine cavity density. The validity of this technique was verified by comparison of these results with manual cavity counting on pictures of the same area taken under normal contrast conditions.

4. Results

For each specimen geometry (e.g. smooth, notched round bar and plane- strain tensile), tests were carried to failure for at least two different load levels, to ensure that the failure mechanism was intergranular. The test durations, stress levels and other relevant data are summarized in Table I. The notched bar samples were examined from the edge of the notch through to the centre of the specimen. The position of the sampled grains were carefully determined on the low magnification pictures. In these samples damage was expressed as the number of nucleated grain boundary cavities per unit area of grain boundary. The data obtained from these studies are summarized in Fig. (4).

For smooth tensile specimens and plane-strain tensile specimens the number of cavities observed at grain boundaries as a function of time and the accumulated average effective creep strain are given in Figs. (5) and (6). As can be seen there is continuous nucleation, the rate of which is strongly dependent on the applied stress level. According to Fig. (6), the nucleation of cavities is controlled by the effective strain. It is independent of the amplitude of the applied tensile stress. The nucleation rate is also independent of the stress state applied. This is demonstrated by the sets of data collected at the same nominal tensile stress of 190 MPa for two geometries. Although the difference between these stress states is small, there is a clear effect on cavity nucleation, which disppears when the data is plotted against the effective strain.

Data points marked "F" represent the density of dimples on the fracture surface. In all cases, this is less than the maximum cavity density observed on unfailed specimens. It therefore appears that cavity coalescence prior to failure decreases the number of

distinguishable cavities on the final fracture surface. A more detailed view is obtained by plotting the density of cavities within a certain size range (Fig. 7). There is a continuous increase in the number of large cavities ($> 0.4\,\mu m$), up to fracture. The density of smaller cavities on the fracture surface is considerably less than that observed on the interrupted samples, however.

The variation of cavitated area fraction is shown in Figs. (8) and (9) as a function of time and the effective creep strain, respectively. As with nucleation, the growth rate of cavities correlates well with effective strain, and not with the nominal tensile stress.

The minimum creep rates were determined using smooth tensile specimens at different stress levels. The results obtained are given in Fig. (10), together with the coefficients of Norton's power law.

5. Discussion

A quantitative assessment of the effect of stress triaxiality on the accumulation of cavitation is needed to understand the processes which occur in the vicinity of a crack tip. In this study we have used three geometries. Of these, the most severe geometry, and that which most closely approximates a crack tip, is the notched tensile bar. We discuss those results first.

When a notched specimen is loaded initially, an elastic stress distribution, concentrated at the notch root is produced. This subsequently relaxes until a steady-state is achieved. The finite element analysis of this problem is discussed in Appendix III, along with the results. As Figs. (A3-3) and (A3-4) indicate, the notch root stresses relax considerably while those in the centre of the sample increase with time (especially for the most severe notch). This relaxation occurs by the rapid accumulation of strain near the notch root (Fig. A3-5). This in turn increases the rate of damage accumulation near the notch root. Indeed the damage distribution curves for interrupted tests (Fig. 4), and the strain distribution curve (Fig. A3-5) are very similar in shape.

Eventually, sufficient damage is developed below the notch root to nucleate a circumferential crack, which then propagates into the centre of the bar. As Fig. 4 indicates, the cavity density associated with this process is considerably higher. This presumably is due to the influence of the increased stress triaxiality on the effective strain accomodated at the crack tip.

The notched bar specimens have certain experimental advantages, such as short failure times and the promotion of the intergranular failure at high levels of stresses. On the other hand, only small regions of the specimen are suitable for quantitative damage analysis. In order to relate the nucleation and growth of the voids to local stress, strain and strain history a detailed knowledge of the stress- strain distribution is necessary. This can only be obtained by means of FEM. Such analyses of each specimen geometry and for different load levels appear unfeasible due to the computational cost. Alternatively, Bridgman solutions might be applied for very blunt notches, but only once a steady-state has been established. Even then, correct monitoring of each experiment is necessary to ensure that microcracks do not nucleate before steady-state is established. It therefore appears that a notched bar tensile specimen is not the most suitable geometry for such a quantitative analysis.

In Fig. (11) the area fraction of cavities measured experimentally on smooth specimens is compared with the analytical models discussed earlier. The material parameters used to compute these curves are:

k	Boltzmann constant: 1.38×10^{-23} J/K
δ_S	grain boundary thickness: 3×10^{-10} m
Ω	atomic volume: 3×10^{-10} m^3
D_B	grain boundary diffusion coefficient: 2.1×10^{-10} m^2/h (for pure iron)
T	temperature: 823°K
B	constant of Norton's power law: 1.07×10^{-15} MPa$^{-5.02}$ h^{-1}
n	power law coefficient: 5.02
ℓ_0	initial cavity spacing: 3.02 μm

f_h initial damage: 0.015

Initial cavity spacing and damage were determined from our quantitative analysis for the shortest interrupted test duration. The power law constants are also experimentally determined. The equations were integrated numerically using 5 hour intervals. The time to failure predicted by the coupled mechanism is close to that found experimentally at 190 MPa. However, the damage is overestimated at all strains. There is almost no correlation for other stress levels. There are obvious difficulties in applying these models to the observed experimental data. First, the damage rate predicted by the models depends on the nucleated cavity size and the cavity spacing. The models treat these as homogeneous and constant, whereas our observation shows them to be both inhomogeneously distributed and time-dependent. Secondly, material data are not easily obtained. Diffusion coefficients are mostly available for pure materials only, while boundary and surface diffusion are known to be sensitive to local chemistry variations.

Our main aim in this work was to study the effect of stress state on damage accumulation. This has been done using pure tensile and plane strain creep tests. The results indicate that both the density of observable cavities, and the cavitated area fraction are controlled by the effective strain, independent of stress level and test geometry. These results are consistent with data on 2¼ Cr-1 Mo steel obtained by Al-Faddagh et al. (1982). They studied the affect of notch acuity on creep failure and found a direct correlation between the variation in failure life and the variation in effective stress for a set of tests on different notch geometries. Other results, for a nickel base alloy Nimonic 80A, obtained by Loveday and Dyson (1979), show a different effect. They also performed notched bar creep tests, and their failure times correlate reasonably well with the effective stress. However, they also measured the cavity density through the notch region, in the same way we have done. They find a correlation of cavity density not with the effective strain, but with the ratio of effective stress to axial stress, thus indicating an influence of the hydrostatic component of stress on cavitation, in this material. We may therefore conclude that no single component of the stress

or strain tensor controls damage in all cases. Nonetheless, for 2¼ Cr-1 Mo steel, under the test conditions we have used, damaged is controlled by the effective strain. The tests we have used to obtain these results are of relatively short duration, up to 1000 hr. It might therefore be argued that for long time tests, and for service conditions, damage may be controlled by some other parameter, perhaps the maximum principal stress. However, from the creep crack growth perspective, this argument is flawed. This is because, as a crack propagates slowly through a structure, only a small zone of material is currently undergoing deformation. Suppose this damage is of order one grain diameter, say 100 μm. Then a 1000 hr creep test corresponds to a crack growth rate of 0.1 μm/hr, or 1 cm in 100,000 hr. We therefore feel it is justified to use the short time data presented here to assess damage ahead of a creep crack. We have therefore adopted, in the crack growth simulations presented in the next section, a damage parameter based on the equivalent strain.

6. Conclusions

i) Creep fracture in 2¼ Cr-1Mo steel appears to be controlled by the accumulated effective strain in the material. This is consistent with data for both the cavity number density, and the cavitated area fraction.

ii) The cavity number density increases linearly with effective strain. The dimple density on the fracture surface is less than the maximum cavity density observed on interrupted samples. This suggests that small cavities coalesce during fracture, and become inseparable on the fracture surface.

iii) The cavitated area fraction increases slowly up to about 3% effective strain, after which, a rapid acceleration ensues.

7. References

Al-Faddagh, K.D., G.A. Webster and B.F. Dyson (1982), ICM4, 289.

Argon, A.S. (1982), "Creep and Fracture of Engineering Materials and Structures", (Ed. B. Wilshire and D.R.J. Owen), 1.

Argon, A.S., I.-W. Chen and C.-W. Lau (1980), Creep Fatigue Environment Intersection (AIME), 46.

Baluffi, R.W. and L.L. Seigle (1955), Acta Met., **3**, 1970.

Beere, W. and M.V. Speight (1978), Met. Sci. J., 1972.

Cane, B.J. (1980), Proc. ICF-4, 1285.

Cane, B.J. and G.W. Greenwood (1975), Metal Sci. J., **9**, 55.

Chen, C.-W. and E.S. Machlin (1956), Acta Met., **4**, 695.

Chuang, T.J., I.K. Kawaga, J.R. Rice and L.B. Silis (1979), Acta Met., **27**, 265.

Cocks, A.C.F. and M.F. Ashby (1980), Metal. Sci. J. **15**, 395.

Cocks, A.C.F. and M.F. Ashby (1981), Prog. Mater. Sci.

Davies, P.W. and B. Wilshire (1961), Structural Process in Creep, 34.

Dyson, D.F. (1976), Metal. Sci. J., **10**, 349.

Dyson, B.F., M.S. Loveday and M.S. Rodgers (1978), Proc. Roy. Soc., **A349**, 245.

Dyson, D.F. and D. McLean (1977), Metal. Sci. J., **11**, 37.

Edward, G.H. and M.F. Ashby (1979), Acta Met. **27**, 1505.

Fleck, R.G., D.M.R. Taplin and C.J. Beavers (1975), Met. Sci. J., **9**, 49.

Gifkins, R.G. (1956), Acta Met., **4**, 98.

Goods, S.H. and L.M. Brown (1979), Acta Met., **27**, 1.

Greenwood, J.N. (1952), JISI, **1971**, 380.

Harris, J.E. (1959), Trans. Met. Soc. AIME, **223**, 1509.

Hart, R.V. (1976), Metals Tech., **3**, 1.

Hull, D. and D.E. Rimmer (1959), Phil. Mag., **4**, 673.

Loveday, M.S. and B.F. Dyson (1979), ICM3, Cambridge, 213.

McLean, D., B.F. Dyson and D.M.R. Taplin (1978), ICF4, Waterloo, 325.

Needham, N.G. and T. Gladman (1980), Metal Sci. J., **14**, 65.

Needham, N.G. and B.J. Cane (1983), ASME Intl. Conf. on Advances in Life Prediction Methods, 65.

Needleman, A. and J.R. Rice (1980), Acta Met., **28**, 557.

Pandey, M.C., B.F. Dyson and D.M.R. Taplin (1982), Proc. CFC-5, "Fracture Problems and Solutions in the Energy Industry", (Ed., L.A. Simpson), 115.

Raj, R. and M.F. Ashby (1971), Met. Trans. **2**, 1113.

Robinson, E.L. (1954), Trans. AIME, **74**, 777.

Smith, E. and J.T. Barnby (1967), Met. Sci. J., **1**, 56.

Speight, M.V. and J.E. Harris (1967), Metal Sci. J., **1**, 83.

Vitek, V. (1978), Acta Met., **26**, 345.

Wear, C.W. (1959), J. Inst. Met., **8**, 249.

Wilkinson, D.S. (1981), Matl. Sci. Engg., **49**, 31.

Wilkinson, D.S. and V. Vitek (1982), Acta Met., **30**, 1723.

Wilkinson, D.S. (1984), 2nd Intl. Conf. on Creep and Fracture in Engineering Materials and Structures, to be published.

Woodford, D.A. (1974), Proc. Intl. Conf. on Creep and Fracture in Elev. Temp. Appl. 180.

TABLE I

Specimen No.	Net Section Stress MN/m^{-2}	Test Duration h	Elongation in ℓ/ℓ_o %	Reduction of Area %
1 NB	313.4	3	0.04	0.57
2 NB	313.4	60.6	0.13	1.97
3 NB	313.4	62.4F	0.22	9.81
1 ST	189.5	447F	14.2	32.97
2 ST	189.5	48	1.2	1.6
3 ST	189.5	431	5.15	5.67
4 ST	189.5	387	7.63	9.82
5 ST	170.5	1036F	11.70	15.80
6 ST	170.5	316	3.56	3.62
7 ST	170.5	193	1.87	1.62
9 ST	151.62	429	2.78	3.06
10 ST	151.62	208	2.19	2.41
1 PS	189.5	610	21.92	11.99
2 PS	189.5	428	14.79	5.32
3 PS	189.5	218	7.36	3.14
4 PS	189.5	113	2.4	0.74

NB: Notched round bar
ST: Smooth tension
PS: Plane-strain tension
F: complete failure

Note: Effective strain is defined as strain in the thickness direction for the P.S. specimens.

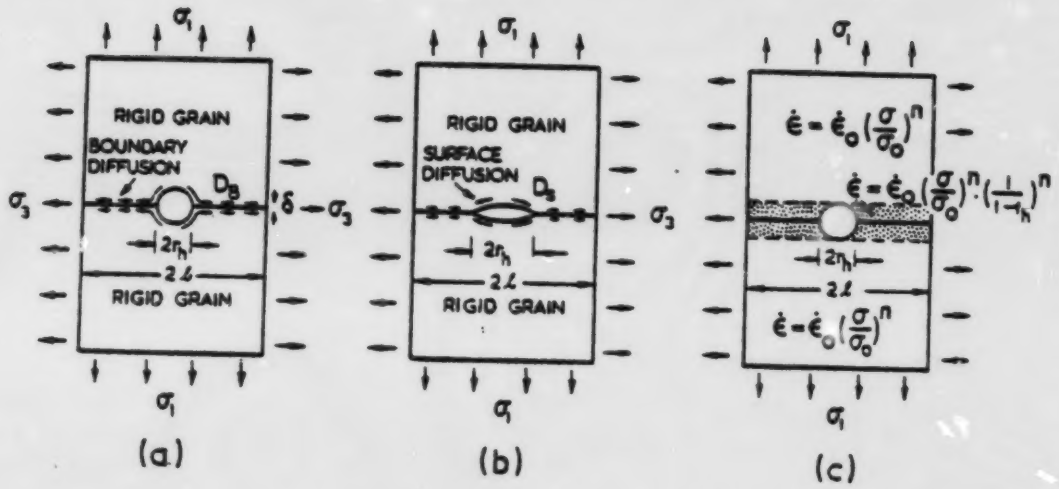

Fig. 1: The mechanisms of cavity growth: (a) boundary diffusion, (b) surface diffusion, and (c) power-law creep (after Cocks and Ashby (1981)).

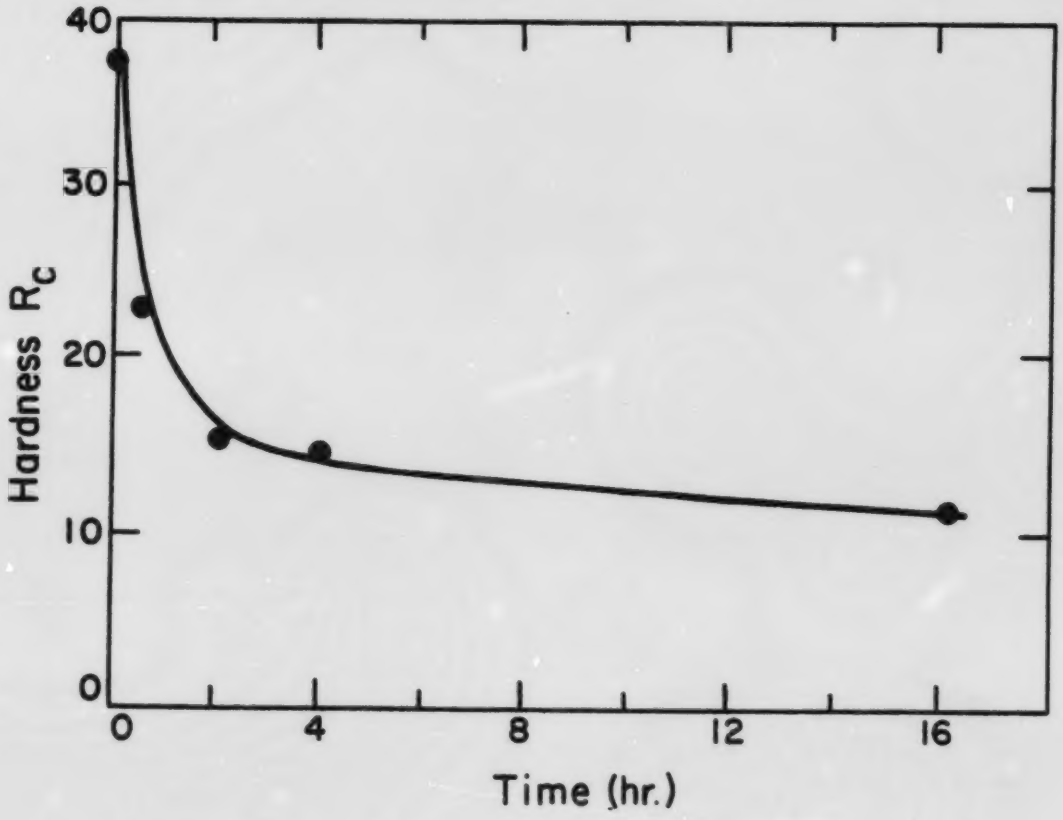

Fig. 2: Tempering characteristics of 2 1/4 Cr-1 Mo steel at 700°C.

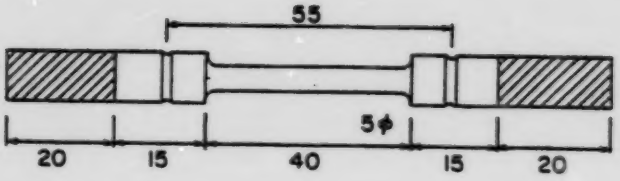

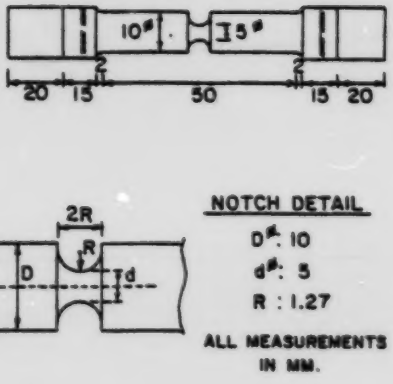

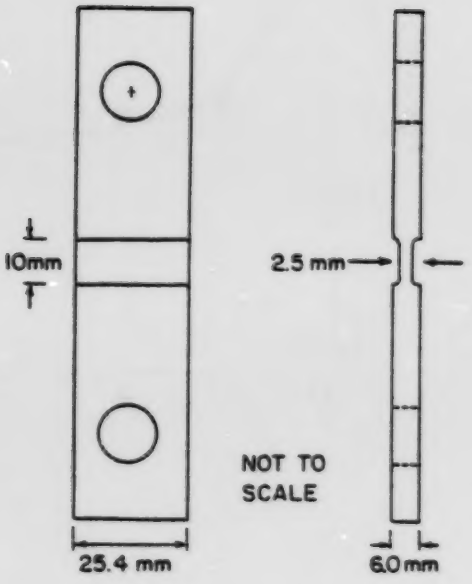

Fig. 3: Specimen geometries used in this study: (a) pure tension, (b) notched tensile, and (c) plane strain.

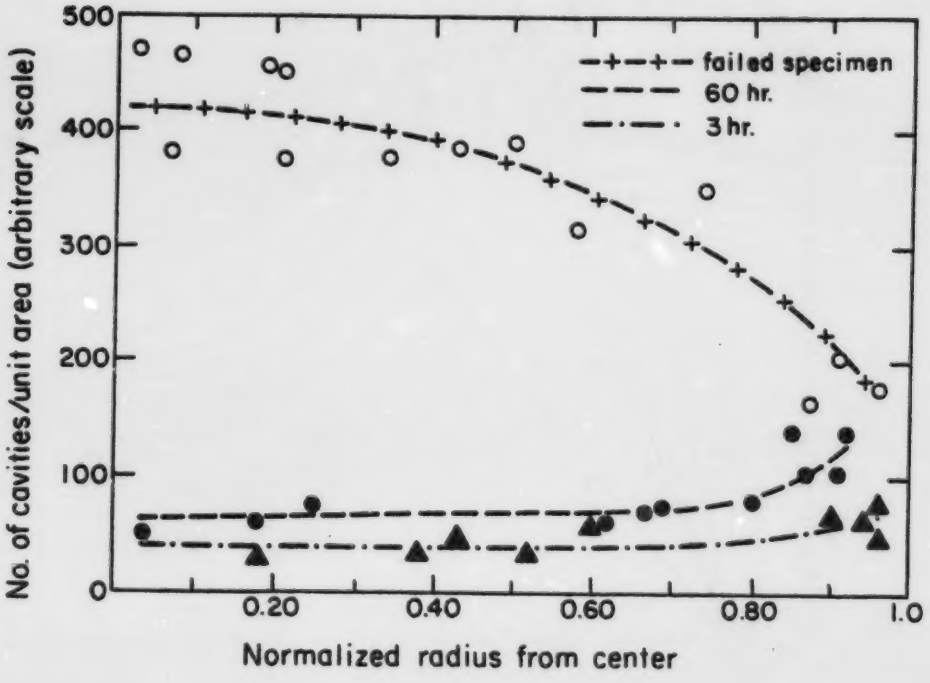

Fig. 4: The cavity density is plotted as a function of distance from the centre of the notch, normalized by the notch radius. All tests were performed at 550°C and a nominal stress of 313 MPa, for three different times.

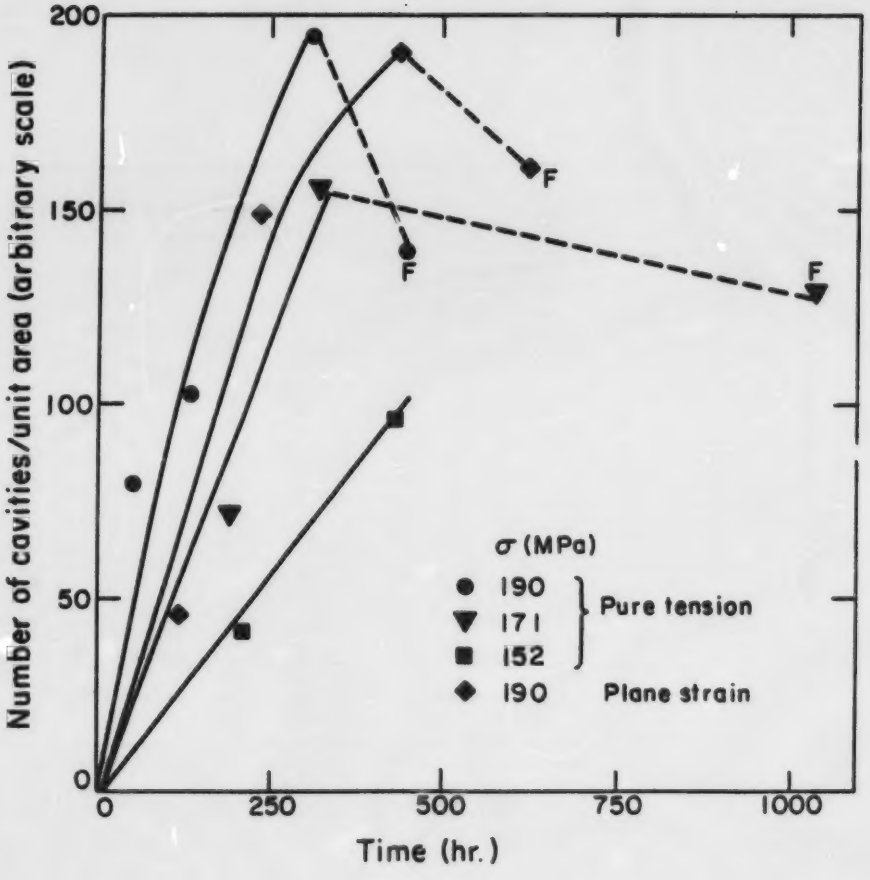

Fig. 5: The cavity density as a function of time. Data marked "F" represent failed samples, in which case the results indicate the density of dimples on the fracture surface.

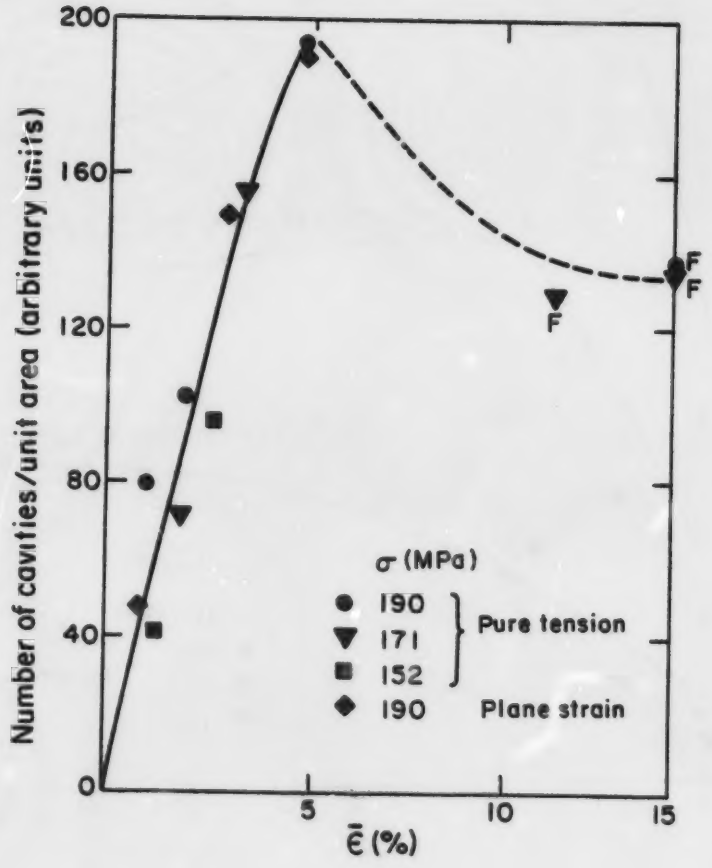

Fig. 6: The same data as in Fig. 5, plotted against the effective strain.

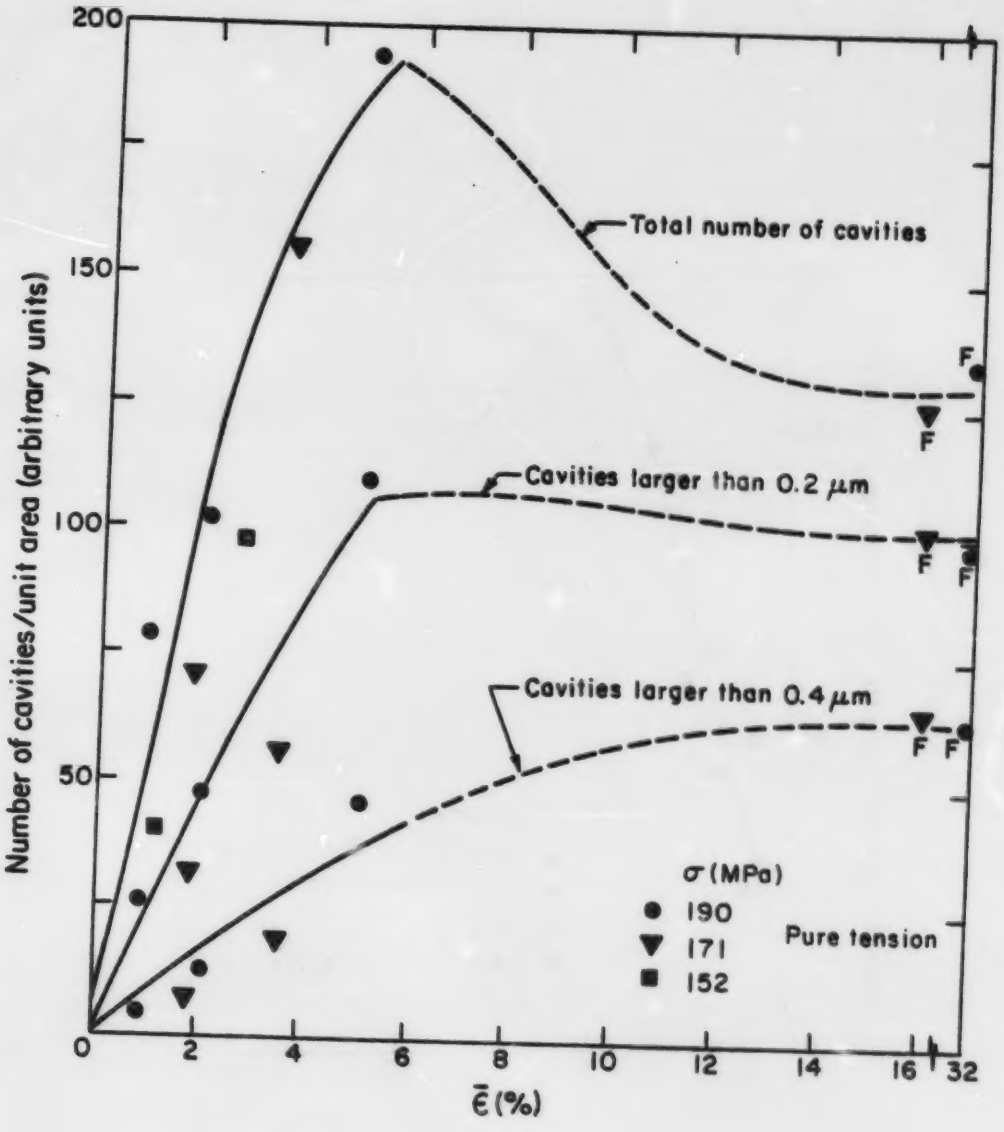

Fig. 7: The cavity density is broken down into three size ranges. The upper curve shows all cavities, while the middle curve shown only cavities larger than 0.2 μm in diameter. Thus, the difference between these shows the density of small cavities (< 0.2 μm). The bottom curve is for large cavities (≥ 0.4 μm).

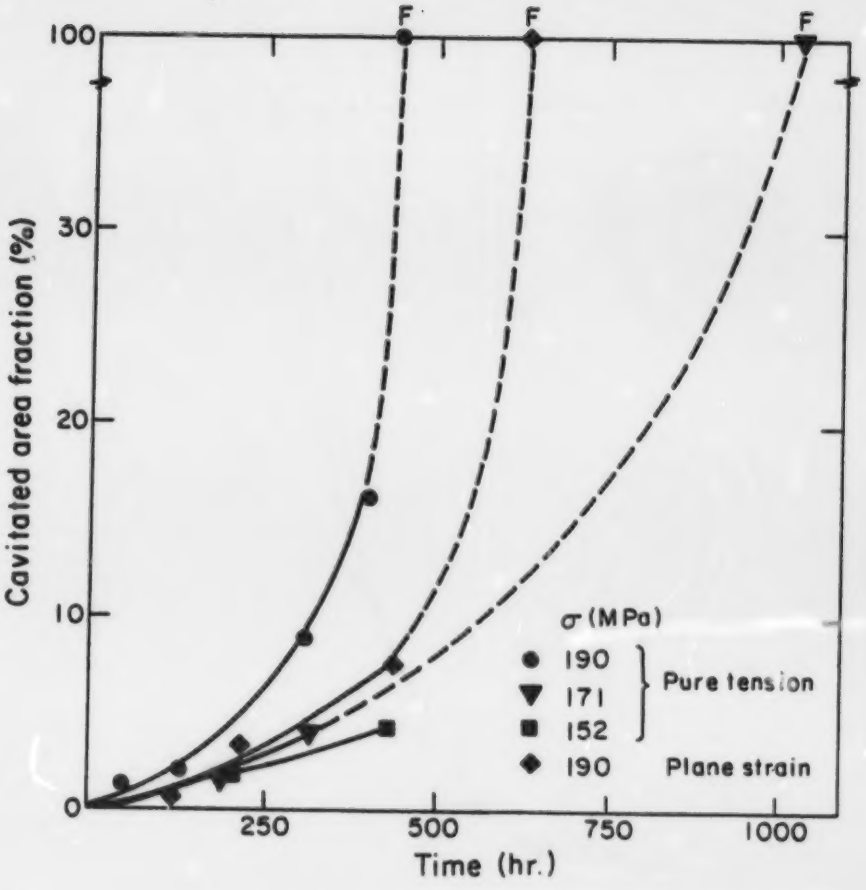

Fig. 8: Cavitated area fraction as a function of time.

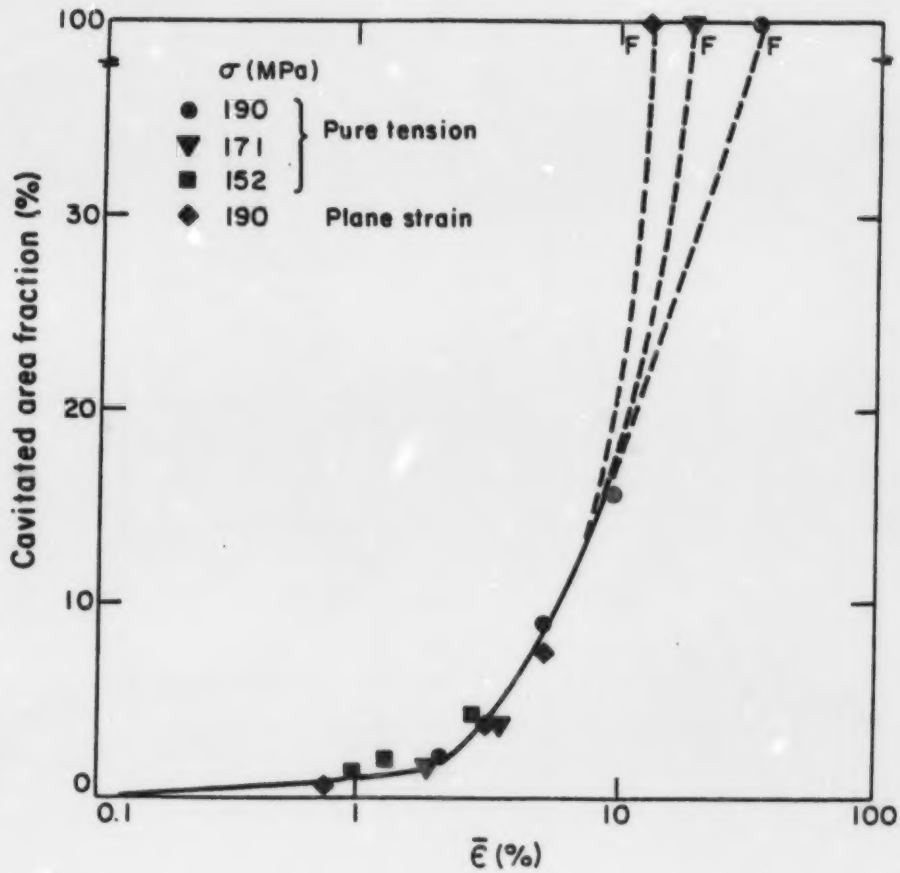

Fig. 9: The same data as in Fig. 8, plotted against the equivalent strain.

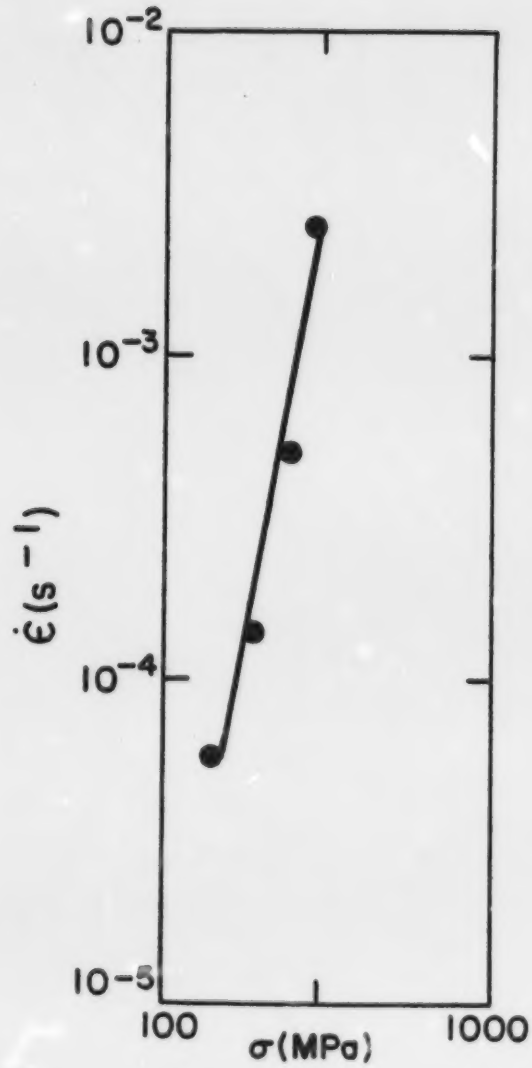

Fig. 10: The minimum creep rate plotted against stress for smooth tensile creep tests at 550°C. The data fit a Norton power law ($\dot{\varepsilon} = B\sigma^n$), where $B = 1.07 \times 10^{-15}$ $MPa^{-5.02}$ h.,and $n = 5.02$.

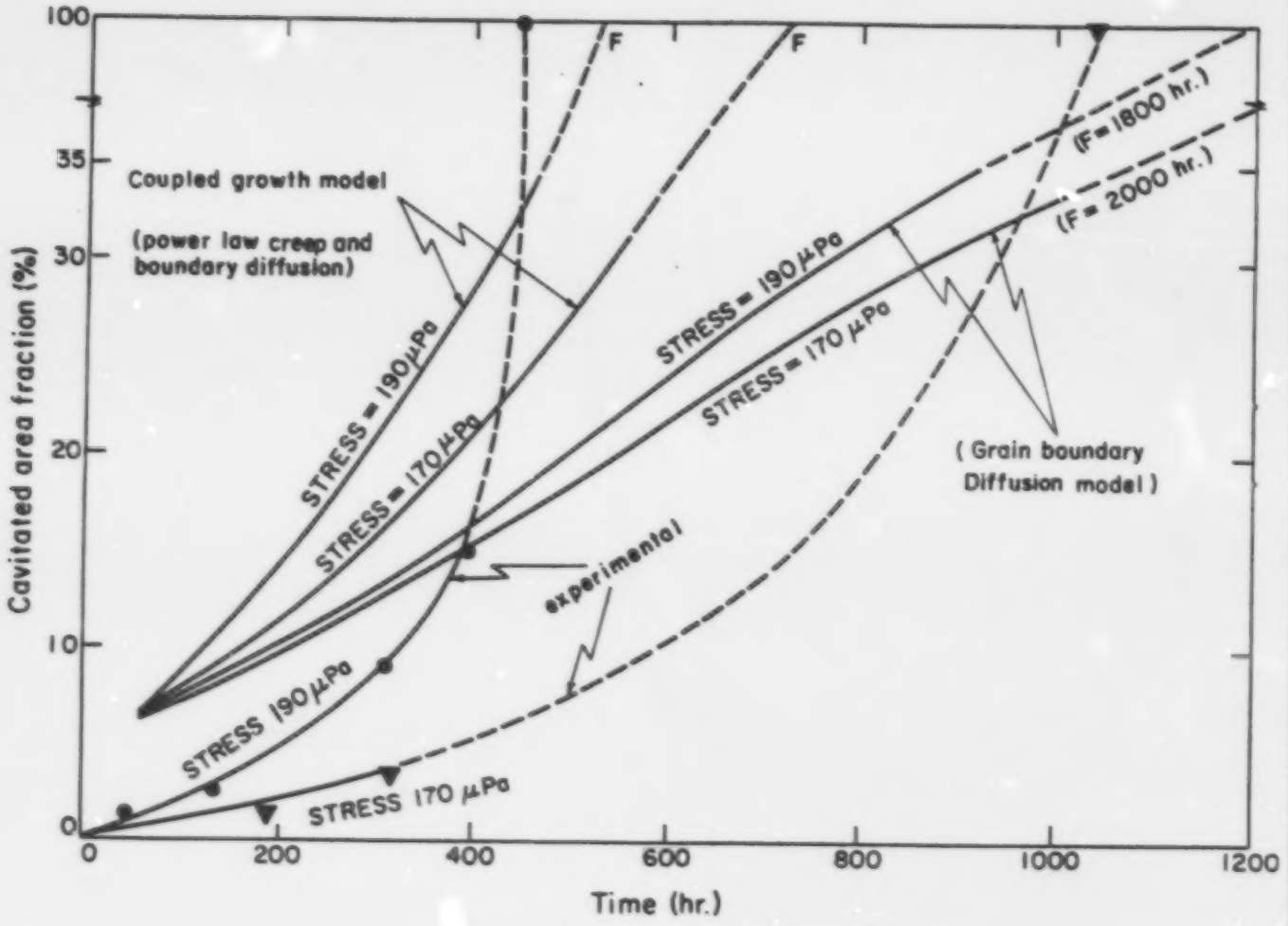

Fig. 11: A comparison of experimental damage data with analytical models for smooth bar creep tests at 550°C.

PART III

FEM MODELLING OF CRACK GROWTH

1. Introduction

In this section, crack *propagation* is modelled using finite element analysis, based on our experimental observations given in Part II. The details of the model are presented. Numerical results are compared with available experimental data.

2. Methodology and Documentation of the Numerical Analysis

The methodology used in the development of the computational model can be described in two stages. These are:

i) Selection of a damage criterion and modelling of crack growth.

ii) Selection of a crack propagation procedure for changing boundary conditions in the finite element model.

Development of the Model:

Because of the nature of finite element analysis, crack propagation must be treated as a step-wise process in which a crack moves in discrete steps, whenever a certain condition is satisfied. When modelling intergranular creep crack growth, this is not unreasonable. There is some evidence, both direct and indirect, that grain boundary cracks tend to propagate fairly rapidly across grain boundary facets, then wait until other parts of the crack catch up. Moreover, some facets may cavitate a short distance ahead of a crack. The process is therefore discontinuous.

The finite element analysis of creep crack growth is developed by modifying that for a stationary crack, developed in Part I. A constant far field load is applied to a cracked body, and the initial elastic stress field is computed. The material then begins to creep and the

stresses relax. However, in addition to calculating the stresses and strains which develop in each element, we also determine the rate of damage accumulation $\dot{\eta}$ for each element in the crack plane. When the total accumulated damage in the vicinity of the crack tip reaches a critical value, then the crack is allowed to advance by some characteristic distance, equal to an integral number of elements.

There are two material parameters which must therefore enter any finite element model for crack propagation. The first is a damage parameter, while the second is the distance by which the crack advances in each step. It is important that these be realistic for the material of interest.

The most appropriate parameter for damage is discussed in some detail in Part II. We use the equivalent tensile strain ε_e (i.e., $\eta = \varepsilon_e$). The appropriate value of equivalent strain for crack propagation is estimated from our experimental measurements to be 5%. This is determined by considering Fig. (9) (Part II). This shows a gradual increase in damage up to about 2% effective strain. Thereafter the rate of damage accumulation increases more rapidly. By a strain of 10%, failure is imminent. The failure strain is about 12-15%. However, before this strain is reached, the material undergoes tertiary creep, which accelerates until the final failure process. Our model does not include an acceleration of damage due to tertiary creep. Therefore, using the actual failure strain would result in too slow a crack growth rate. We therfore use a smaller value for the critical strain, namely 5%. This corresponds approximately to the strain at which damage begins to accumulate rapidly. In general, it may be appropriate to use the Monkman-Grant strain, $\varepsilon_{MG} = \dot{\varepsilon}_{ss} \cdot t_f$ (where $\dot{\varepsilon}_{ss}$ is the steady-state strain rate and t_f the corresponding failure time in a creep test). This is the strain which would accumulate in a creep test if deformation proceeded at the steady-state creep rate throughout the life.

The second material parameter is the characteristic distance for crack advance. In the finite element analysis, this must be no smaller than the mesh size in the crack plane, $2\rho_c$ (see Fig. 1). However, it may be larger. For grain boundary creep fracture, this distance

should correspond to the grain facet size. In the analysis which follows, a mesh size of 0.5 mm is used, which corresponds to roughly twice the grain size for the coarse-grained region of the heat-affected zone of a weld in Cr-Mo steel. It is therefore a reasonable mesh size for this analysis.

The crack growth process is illustrated in Figs. 1 and 2. When the amount of damage in element (j-1) reaches a critical value η_c, then the crack tip advances to element j. In terms of the analysis, this means that we release the nodes across the crack plane which connect element (j-1) to its mirror image below the crack plane. Therefore, the loads on these nodes are relaxed to zero.

We define $\dot{\eta}_{kj}$ and η_{kj} as the damage accumulate rate and the current value of the accumulated damage in element k, when the crack tip is located between elements (j-1) and j. The time between the release of element (j-1) and element j is defined as t_j, and the propagation distance is $2\rho_c$. Therefore, the average rate of crack growth is estimated to be

$$\frac{da}{dt} = \frac{2\rho_c}{t_j} \tag{1}$$

Crack Growth Simulation

Crack growth can be simulated in various ways in an FEM solution. One approach is the node sifting technique suggested by Shih et al. (3). Another involves the node releasing technique suggested by Anderson (1974) and Kfouri and Miller (1976). The first technique requires a prior knowledge of the crack growth rate. Thus the second approach is implemented here. Upon satisfaction of the fracture criteria, the crack is allowed to propagate. The reaction forces required to release the nodes at the crack-tip are calculated. When these are applied, loads on the released nodes are reduced to zero. These forces are calculated so as to maintain equilibrium with the applied loads. The process of nodal force relaxation is done in a time step equal to zero. After relaxation, the time step is reduced to its

initial value. This allows for rapid relaxation following crack advance, and insures convergence of the solutions during subsequent deformation.

3. Details of the FEM Studies

The finite element grid used in these analyses is shown in Fig. 3. As described in Part I, by a suitable selection of the boundary conditions, both the SEN and DEN geometries can be modelled using the same grid. The grid consists of 8 node isoparametric elements and 6 nodes transition isoparametric elements. Due to the nodal release technique employed in the analysis, we do not use special crack-tip singular elements as in Part I, since crack advance would require a procedure for refocussing the mesh at the tip of the extended crack. The program used in the analysis is a modified version of that for stationary cracks described in Appendix I. It differs primarily in the addition of a damage accumulation algorithm, and the routines to perform node release once the crack is ready to advance.

Loading is applied from the ends of the specimens. The initial crack length is kept constant at a/w = 0.4 and the initial stress intensity factor at $K_I = 20\ \text{MPa}\sqrt{\text{m}}$. The same time stepping procedure outlined in Part I is employed. However, when the crack advances the time step is reduced, as described above. The material parameters used in the analysis are $E = 150\ \text{GN/m}^2$, $\nu = 0.3$, $n = 5.02$, $B = 1.072 \times 10^{-5}\ \text{MPa}^{-5.02}\ \text{h}^{-1}$ (these being derived from our experimental studies on 2¼ Cr 1 Mo steel discussed in Part II).

4. Results and Discussion

Figure 4 shows the rate of crack growth, as a function of crack extension for both geometries. Note that no data are given for the first crack advance. Both the absolute rate of crack growth, and its dependence on crack extension are a function of geometry. The value of the C-integral, calculated along various paths, is determined immediately prior to each crack advance. These are plotted in Figs. 5 and 6 for the SEN and DEN geometry, respectively. The "near field" value is calculated over the integral path closest to the crack tip. The "far field"

value is an average of C values computed from three integral paths furthest from the crack tip (the variation being indicated by the error bars). The open points represent the C* values calculated using the J-integral tables of Kumar and Shih (1981), as discussed in Part I. (The discrepancy between the FEM results and the tabulated values for the DEN geometry are also discussed in Part I.) For both geometries, the initial value for C (i.e. just before the first crack advance) is path independent. Thus, the stresses have relaxed to a steady-state field. However, once the crack begins to grow, some path dependence reappears, and persists throughout crack growth. This effect is strongest for the DEN geometry, for which the near and far field integrals diverge sharply during crack growth. At the maximum divergence, the C values differ by a factor of two.

Figures 7 through 9 show attempts to correlate the crack growth rate with various common characterizing parameters. In Fig. 7, very poor correlation is found with the stress intensity factor K_I. The correlation is worst for the first growth increments when near steady-state C* conditions are obtained. As crack growth continues and the stresses become less relaxed, the correlation improves, but it is always poor. A similar situation is found when the crack opening displacement rate is used, as in Fig. 8. Here, COD is defined as the separation of the crack at the original crack tip.

Figure 9 shows the correlation of crack growth rate with the far field intergral, C_{far}. As Fig. 6 indicates, C_{far} values are the same as those calculated using the end displacement of the specimen. They are therefore comparable to the values determined experimentally by measuring the load point displacement. This is what experimentalists often refer to as C*, whether or not the structure is at steady-state. As Fig. 9 indicates, there is a reasonable correlation between crack growth rate and C_{far}. However, there are systematic differences between the two curves, which result from the loss of a steady-state stress field during crack growth.

It is also worth noting that the curves are very shallow for both geometries (much less than one). Most theories of creep crack growth in a steady-state C* field suggests a relation-

ship of the form

$$\frac{da}{dt} \sim (C^*)^{\phi} \qquad (2)$$

where ϕ is a number slightly less than one. If we were to consider only the first point on each curve in Fig. 9, and draw a line through these points, a slope of just under one is found. These points are the closest we can get to steady-state conditions. This behaviour is also seen in experimental data. A large volume of data can often be fit to a relationship like eq. (2) with ϕ near to one. However, the individual experimental curves often have a much smaller slope. It appears that in many cases, the rate of load shedding during crack growth is too rapid for steady-state to be maintained. The far field C integral therefore increases rapidly, decreasing the slope of a log (da/dt) vs. log(C_{far}) curve.

The crack growth rate is plotted against the near field C integral in Fig. 10. For convenience, this integral is labelled C_B, although it is not determined by extrapolation to zero path length, but from the integral path nearest the crack tip. Correlation of crack growth with C_B is excellent. This should not be surprising since C_B characterizes the stress field near the crack tip where the damage is occurring.

Comparison of Results with Experimental Data

The finite element results are compared with available experimental data for 2¼ Cr-1 Mo steel in Figs. 11 to 15. In Fig. 11, the numerical results are compared with the data of Gooch (1983), using 2¼ Cr 1 Mo weld metal. These tests used 1" thick compact tension specimens. The data agree very well with the FEM results for the SEN specimen, (for which the loading is similar to a CT specimen). Figure 12 shows the same data plotted against C*. The agreement between experiment and the numerical results is excellent. Note, however, that the C* referred to is that measured experimentally from the load point displacement or (in the case of FEM results), the far field integral. It does not represent a steady-state.

Figure 13 shows the results of Gooch and King (1976) for an SEN geometry, along with numerical results for the same geometry. Although in their work the grain size is slightly lower than ours, and the applied net section stress is 93 MN/m^2 compared to 120 MN/m^2 in the FEM analysis, the agreement is reasonable.

Figure 14 shows the results of Nibkin et al. (1983) on 2¼ Cr-1 Mo steel, tested at 538°C using compact tension specimens. This is a lower temperature than that used for the FEM work. However, most of the temperature dependence of crack growth is contained within the C* parameter, because of its dependence on the Norton creep parameters. Therefore if the crack growth rate is plotted against C*, as in Fig. 14, comparison of data for different temperatures is possible. These data occur over a higher crack growth rate range than those considered previously. Yet the extrapolation of the data to the range of the FEM studies indicate reasonable correlation. Moreoever, these data are for two different specimen configurations. The points marked (x) are closer to plane strain conditions. Their extrapolation to lower C* values shows excellent agreement with the FEM results.

Finally, we consider the work of Siverns and Price (1973), shown in Fig. 15. They tested 2¼ Cr-1 Mo steel following a simulated heat-affected zone treatment consisting of high temperature austenization, quench and temper at 690°C for 1 hour. This short tempering treatment results in a rather more brittle material than those discussed previously. As seen from Fig. 15, the numerical results obtained using a 5% failure strain predict crack growth considerably slower than those observed experimentally.

The critical effective strain for crack advance is based on experimental observations. Moreover, the appropriate value depends on conditions, such as the testing temperature, and especially the metallurgical condition of the material. Therefore, we do not expect that the critical value to be constant for all situations. This is shown most clearly by the experiments of Siverns and Price, in which samples of 2¼ Cr-1 Mo steel of high hardness were tested. The apparent decrease in creep ductility greatly increases the crack growth rate in comparison with the other experimental data, and with the FEM results.

The critical strain used here, namely 5%, gives good agreement with most of the experimental data in the literature. These materials were tested either in the as welded condition, or they had been given a heat treatment to simulate that experienced in the coarse-grained region of a weld heat-affected zone, followed by a reasonable stress relief heat treatment. This was also the condition of the creep specimens from which the 5% value was obtained. This encourages us to believe that the critical strain for crack advance can be determined from an assessment of damage in simple creep tests, as discussed in the previous section.

The characteristic distance for crack advance is also a material parameter, related to the microstructure of the material. However the microstructural parameter which governs this parameter must depend upon the fracture mode. For example, if fracture is intergranular, it is related to grain size. However, for transgranular fracture, it should be related to other microstructural features such as inclusion spacing. It is therefore clear that for intergranular fracture the characteristic distance cannot be smaller than one grain diameter. However, it will also depend on the extent of the damage zone ahead of the crack, and thus on the ductility. Therefore, the characteristic distance could be several times the grain size. For example, consider the experimental results of Nikbin et al. (1983) in Fig. 14, for which the grain size was 20 μm.

5. Conclusions

i) The process of creep crack growth can be simulated using the finite element method. Crack growth occurs in discrete steps whenever the relevant damage parameter reaches a critical value.

ii) For coarse-grained 2¼ Cr-1 Mo steel, an appropriate damage parameter is the equivalent strain. The critical strain for crack advance is estimated to be 5%, for the material condition studied in Part I. The appropriate step size for crack advance is the grain diameter. This is approximated in the current analysis.

iii) The results indicate that while a steady-state stress field may be established initially, this may be lost during crack growth, due to the effect of load shedding.

iv) The crack growth data can be correlated with the near-field integral C_B.

v) Unless a steady-state persists throughout crack growth, none of the far-field parameters correlate the crack growth data. However, if a steady-state is established initially, then C_{far} may provide an acceptable parameter for practical purposes. This is the parameter which is measured experimentally.

vi) The finite element results agree very well with crack growth data for 2¼ Cr-1 Mo steel in a condition similar to that tested in Part II. This suggests that the rate of crack growth can be estimated using data on the rate of damage collected in uniaxial creep tests.

vii) It may be possible to use accelerated creep tests on in-service material to assess the loss of ductility incurred during service exposure, and therefore, the enhancement of creep crack growth expected.

6. References

Andersson, H. (1974), J. Mech. Phys. Solids, **22**, 285.

Gooch, D.J. (1983), C.E.R.L. Report No. TPRD/L 12384/N82-1983.

Gooch, D.J. and B.L. King, (1976), C.E.R.L. Report RD/L/R-1976.

Kfouri, A.P. and K.J. Miller (1976), Inst. Mech. Eng., **190**, 571.

Kumar, V. and C.F. Shih (1981), EPRI Report No. 1931/1237-1.

Nikbin, K.M., D.J. Smith and G.A. Webster (1983), ASME Int. Conf. on Advances in Life Prediction Methods.

Shih, C.F., H.G. deLorenzi and W.R. Andrews (1979), ASTM-STP 668, 65.

Siverns, M.J. and A.T. Price (1973), Intl. J. of Fract., **9**, 199.

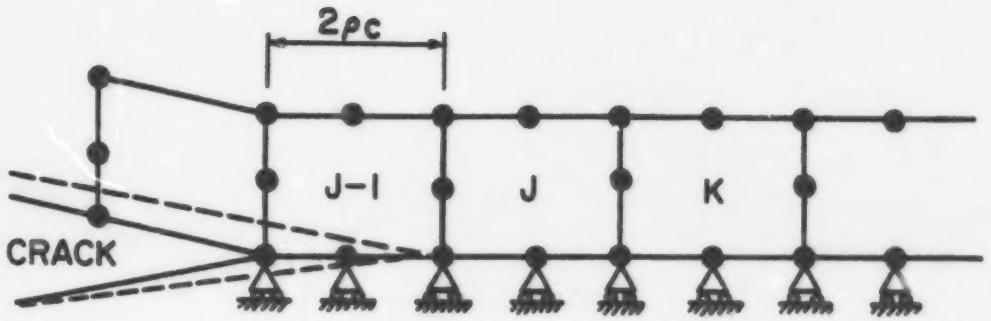

Fig. 1: This figure illustrates the procedure by which nodes are released at the crack tip when the crack propagates.

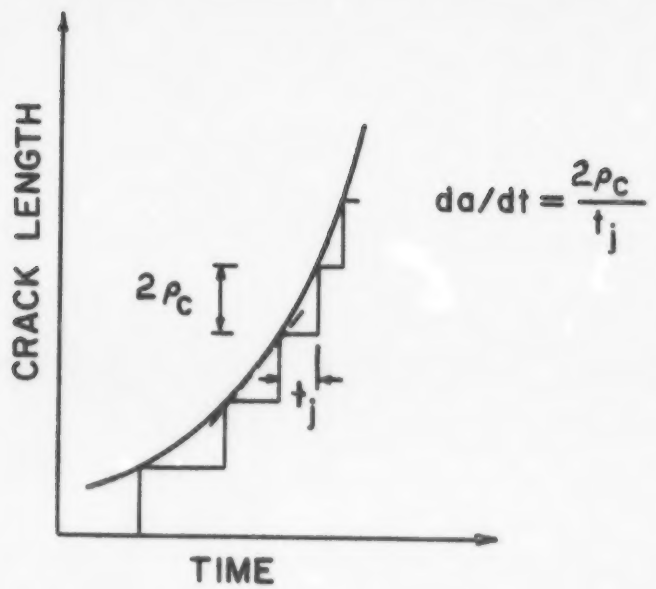

Fig. 2: Crack propagation occurs in steps, in which the crack front moves by ρ_c. If the time between steps is t_j, then the crack growth rate is ρ_c/t_j.

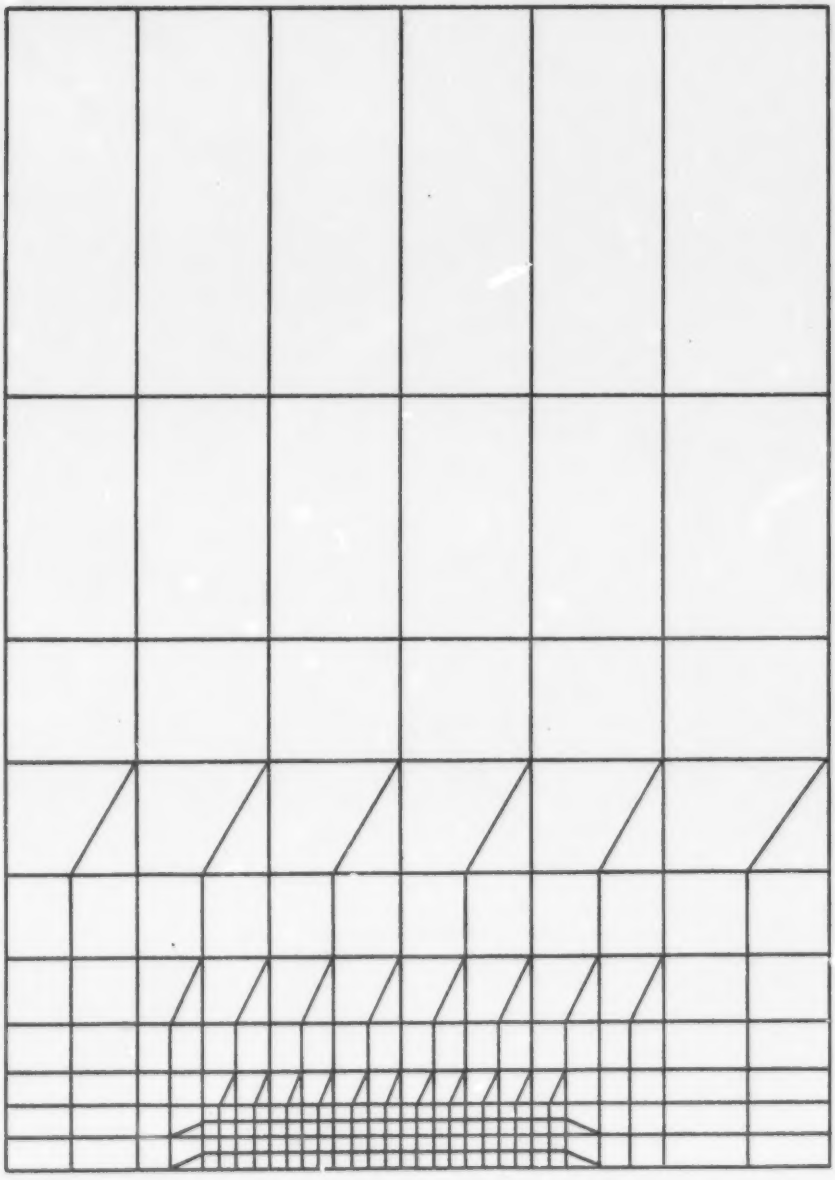

Fig. 3: Finite element grid used for the crack propagation analysis.

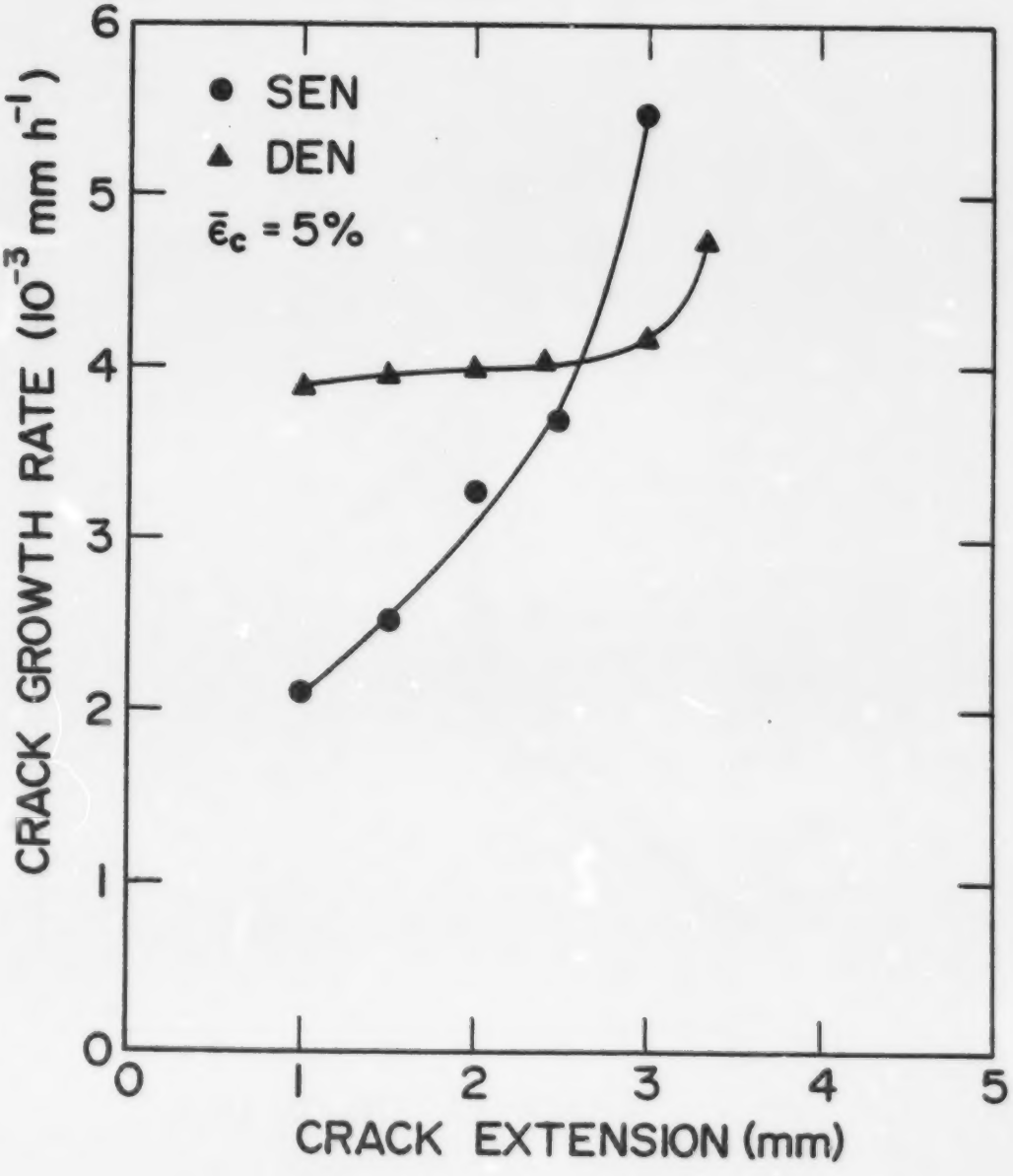

Fig. 4: The rate of crack growth as a function of crack extension for two geometries.

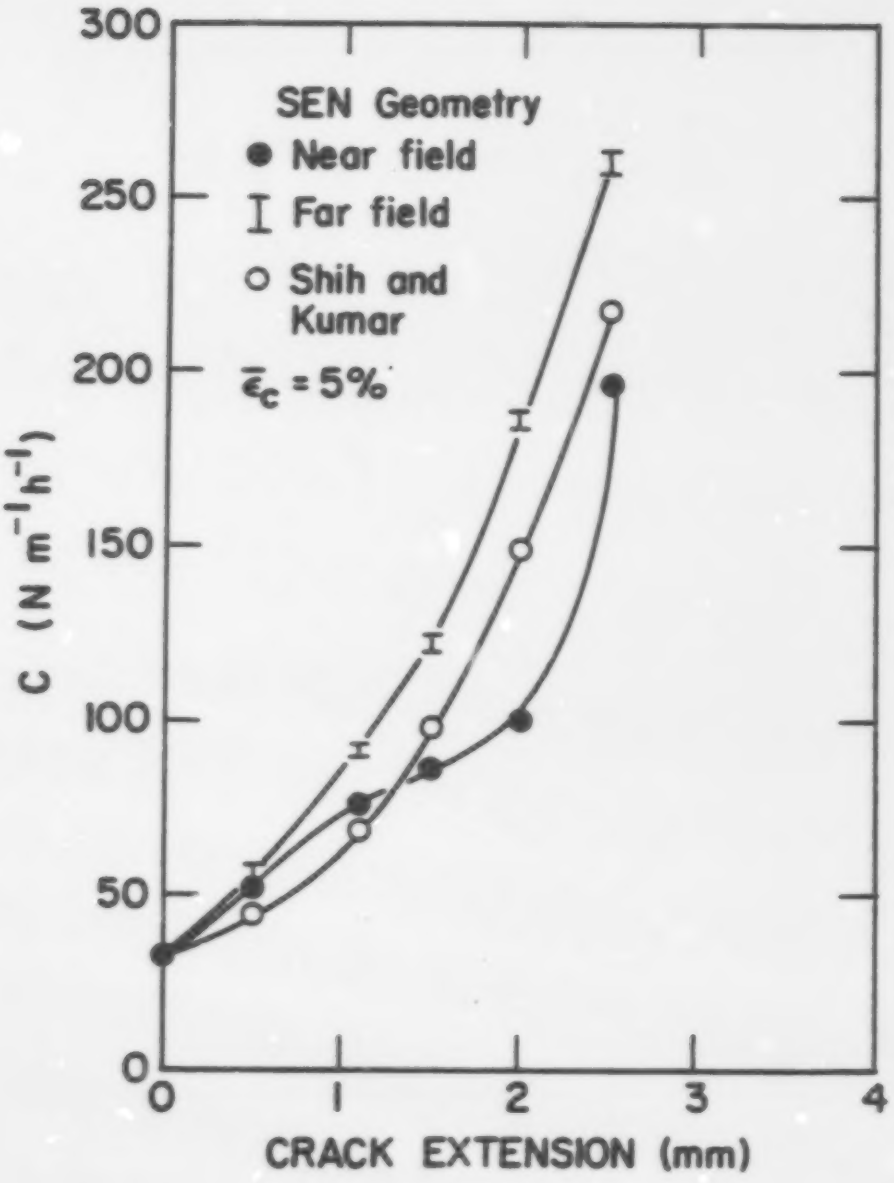

Fig. 5. The value of the C-integral calculated over several paths for the SEN geometry. These values are calculated immediately prior to crack extension.

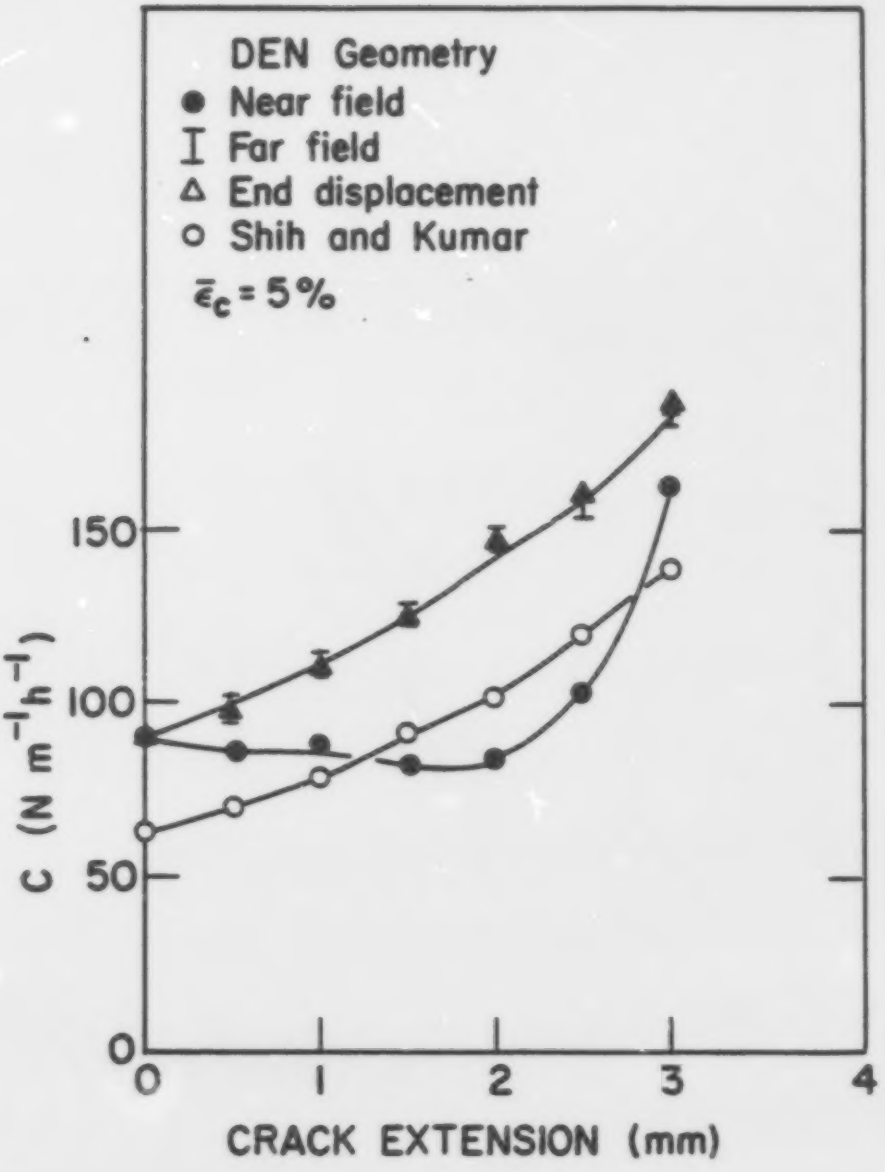

Fig. 6: The value of the C-integral calculated over several paths for the DEN geometry. These values are calculated immediately prior to crack extension.

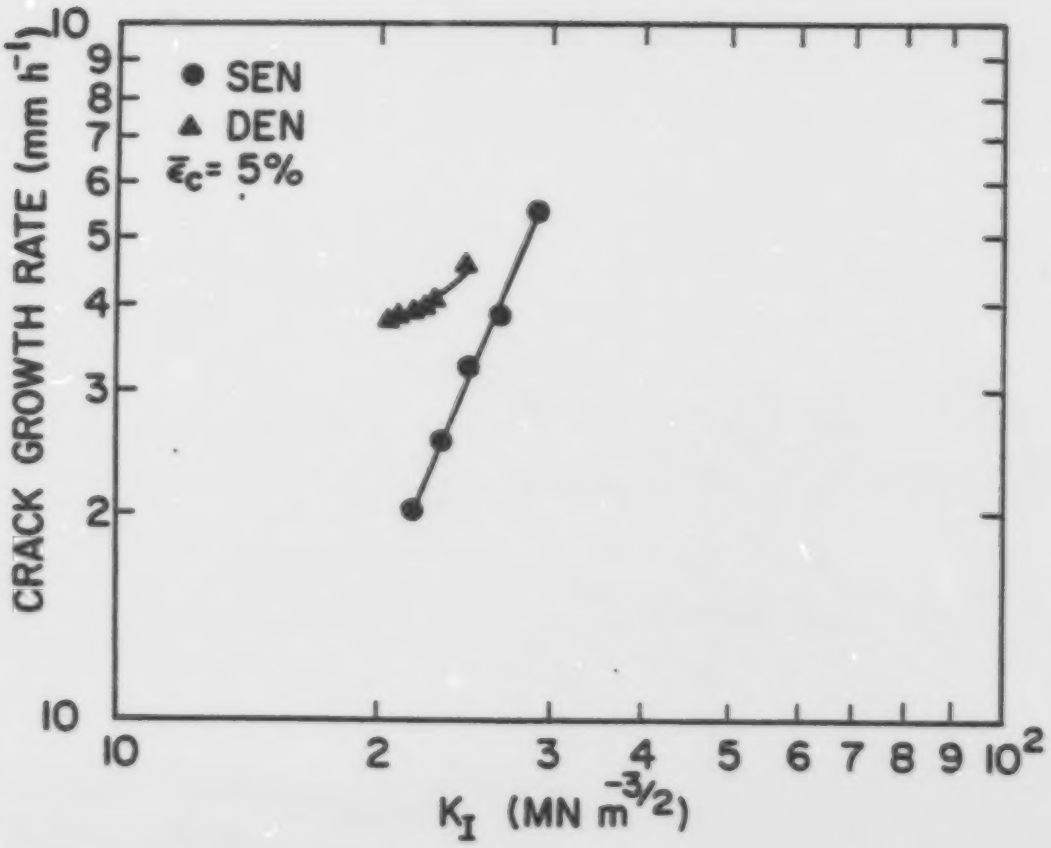

Fig. 7: The crack growth rate correlated with the nominal stress intensity factor K_I

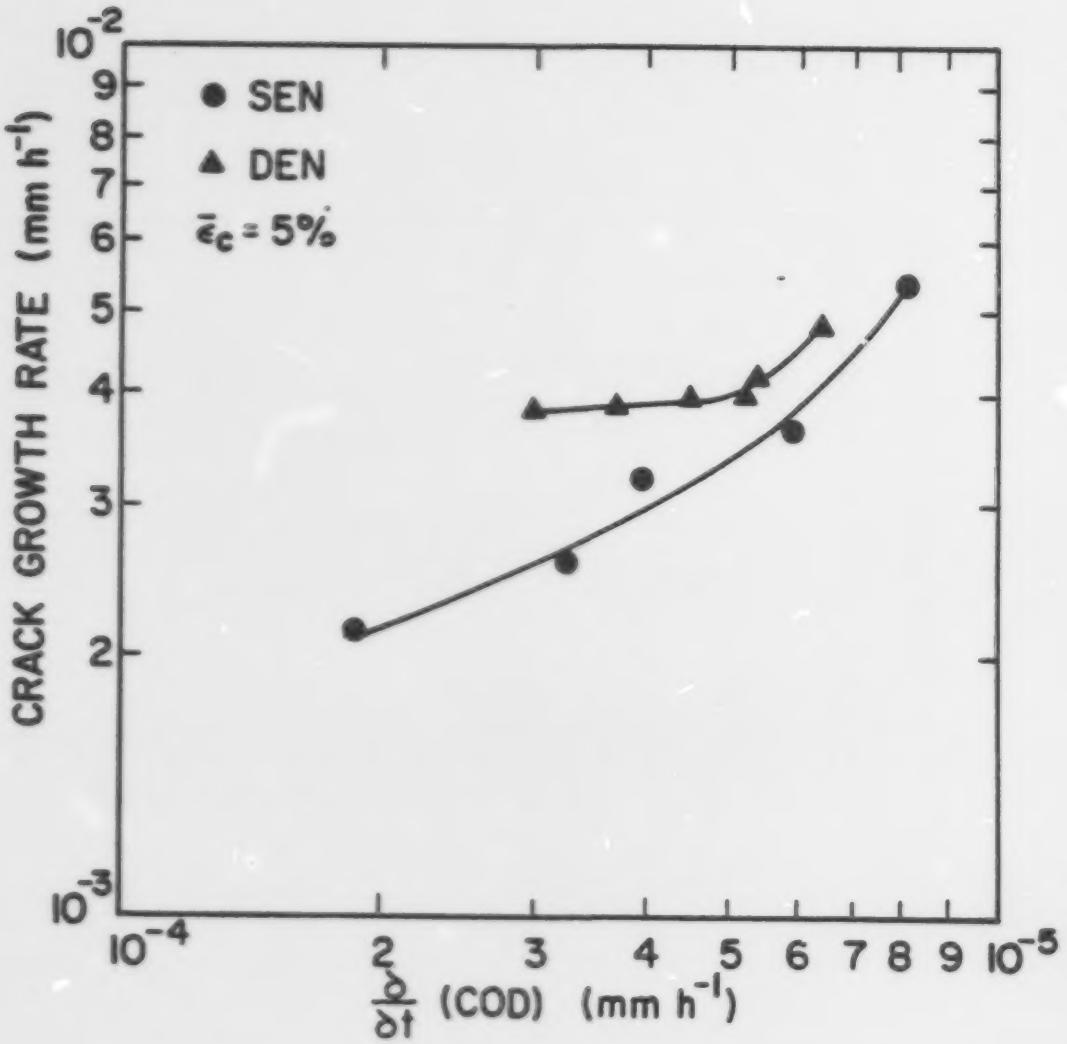

Fig. 8: The crack growth rate correlated against the crack opening displacement rate.

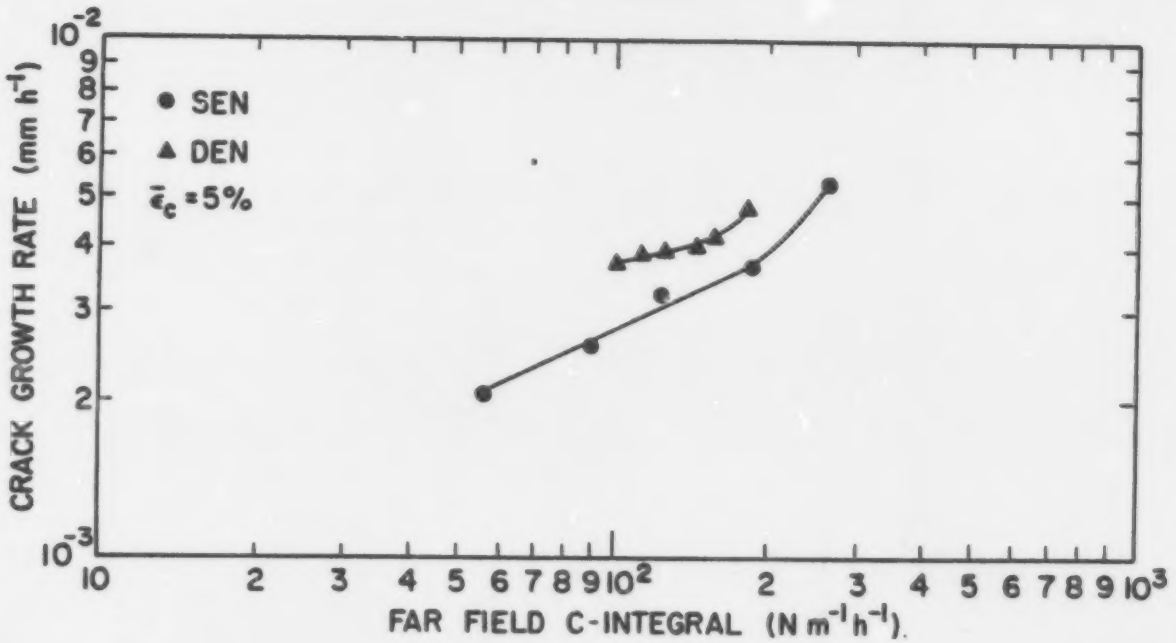

Fig. 9: The crack growth rate correlated against the far-field C-integral.

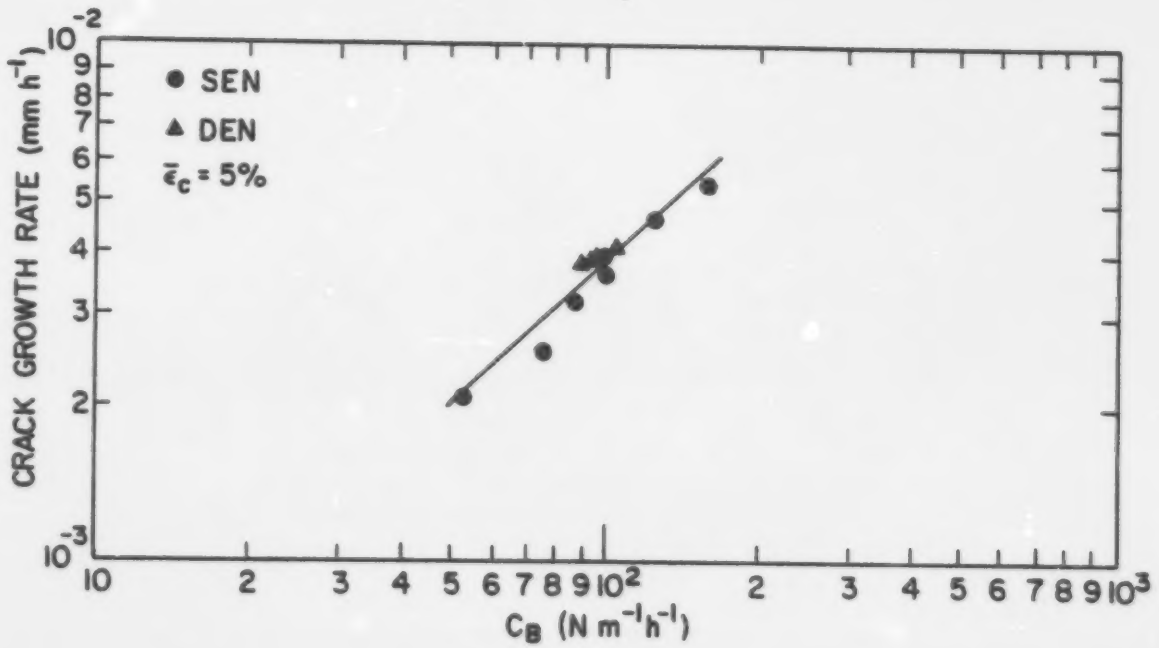

Fig. 10: The crack growth rate correlated against the near-field C-integral, C_B.

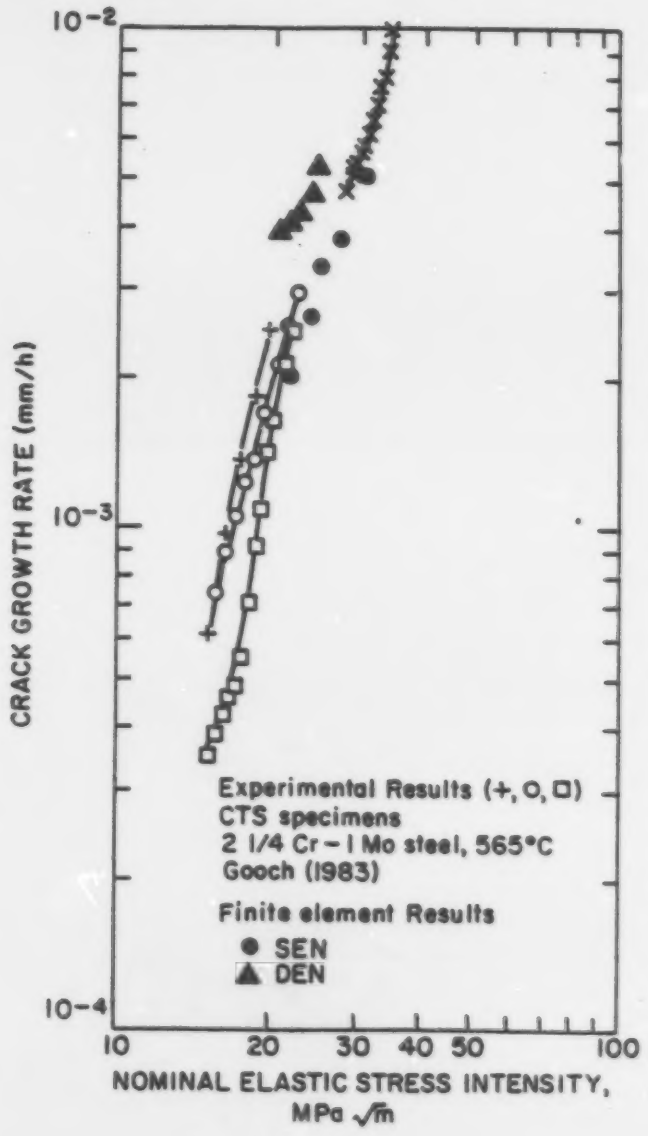

Fig. 11: Experimental data of Gooch (1983), together with the F.E.M. results, plotted against the nominal elastic stress intensity factor.

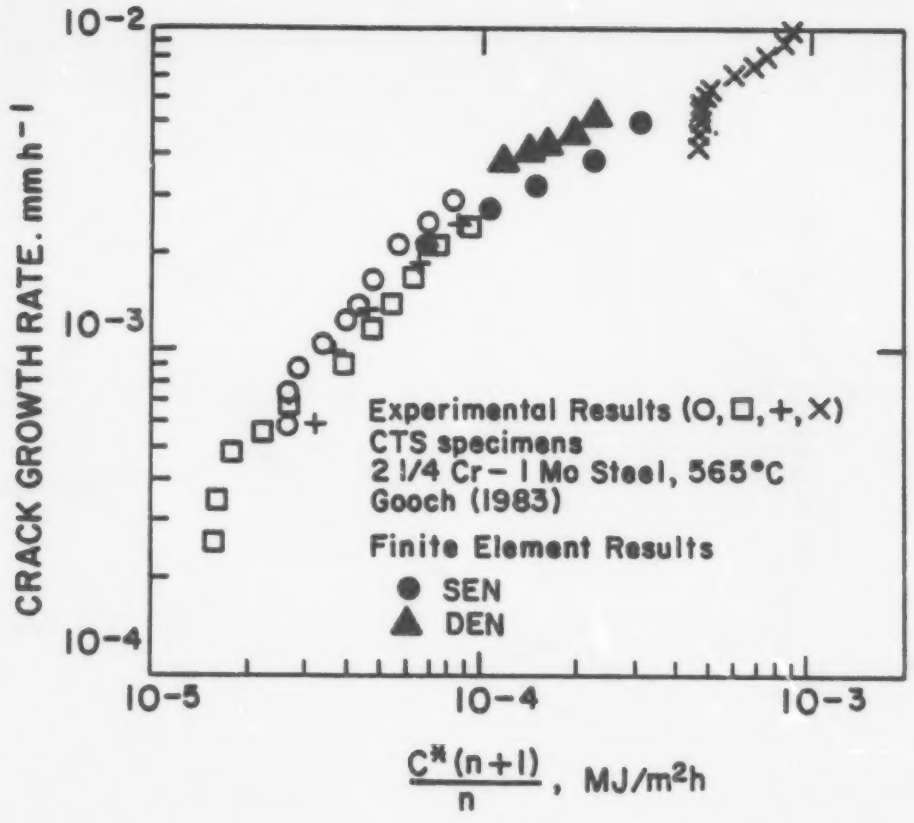

Fig. 12: The same results as in Fig. 5, but plotted against C*, and showing excellent correlation.

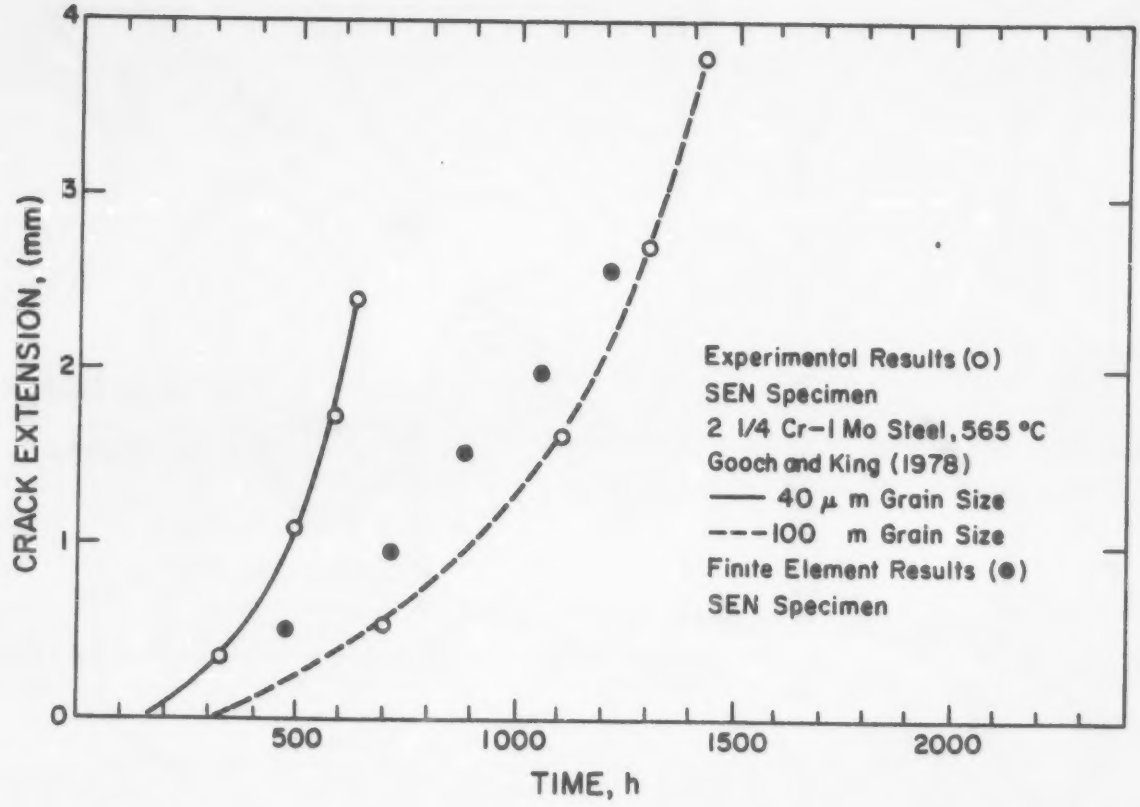

Fig. 13: The experimental data of Gooch and King (1978), together with FEM results for the SEN geometry.

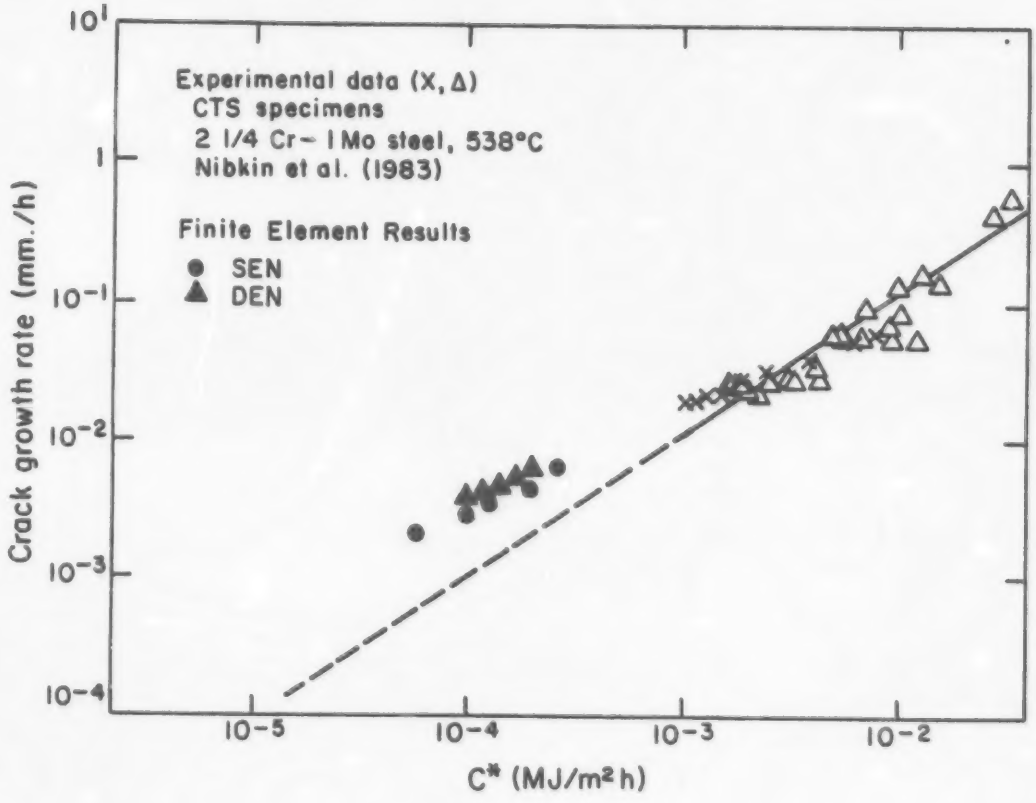

Fig. 14: The experimental data of Nibkin et al. (1983), together with the FEM results.

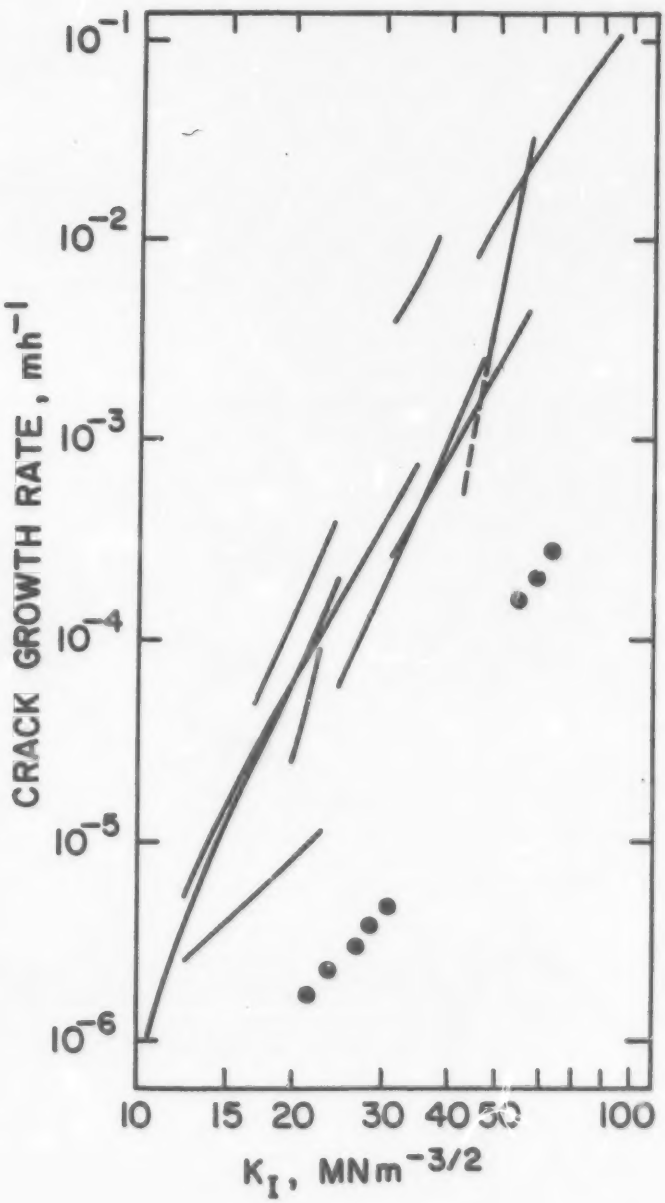

Fig. 15: Experimental data of Siverns and Price (1973), together with the F.E.M. results for the SEN specimen geometry.

CONCLUDING REMARKS

In this project, we have attempted to assess the applicability of fracture mechanics concepts to creep crack growth in thick-walled pressure vessels operating in the creep regime. Particular attention has been paid to welded 2¼ Cr-1 Mo steel plate. Our approach has been to combine an assessment of the process of creep damage in coarse-grained 2¼ Cr-1 Mo steel, with a simulation of creep crack growth using the finite element method.

The experimental work on creep damage leads us to conclude that such damage is controlled by the effective strain and not by, for example, the maximum principal stress. The data which leads to this conclusion is collected over a creep life range which is relevant to the creep crack growth process. We have used quantitative metallography to measure both the cavity number density and the cavitated area fraction as a function of strain. These data are used to estimate the appropriate critical failure strain for use in finite element modelling. For reasons discussed in the report, this is not the effective strain to fracture during creep, but rather the strain at which rapid damage coalescence commences.

These experimental results have been used to simulate creep crack growth. Since creep damage occurs in a region close to the crack tip, it is the stress field in this region which controls the rate of crack propagation. However, for practical purposes, we would prefer to correlate the rate of crack growth with macroscopic parameters, measured far from the crack tip. These include the crack opening displacement rate and the experimentally measured C* integral. From the finite element results presented in Part III, it is clear that this approach is strictly valid only if the structure has relaxed to a steady-state stress field. In this case, the stresses near the crack can be determined using measurements far from the crack tip. It is also clear that it is difficult to maintain a steady-state stress field as a crack grows. This is because of the shedding of load from the crack tip, which occurs as the crack advances. We have found, for example, that even if the stresses relax to a steady-state field before the crack begins to propagate, this situation is not maintained as the crack grows.

We have considered the possible application of new fracture mechanics parameters, which may be able to characterize the stress field near the crack tip, even under non-steady-state conditions. This is considered in detail for a stationary crack in Part I. We have found that a parameter C_B, defined as

$$C_B(t) = \lim_{p \to 0} C(t) \tag{1}$$

has potential application. C_B defines the limiting case of the path-dependent integral C(t) as the path collapses into the crack tip. The value of this parameter lies in two of its properties. First, we find that it characterizes the stress field surrounding the crack tip under both transient and steady-state conditions. Second, we have shown that $C_B(t)$ can be estimated using the steady-state value C^* and the nominal stress intensity factor K_I, as

$$C_B = C^* \left(\frac{t_I}{t} \right)^s \quad \text{if } t < r t_I$$

$$C_B = C^* \qquad \text{if } t > r t_I \tag{2}$$

where $r = 2.4$, $s = 0.73$ and t_I is given by

$$t_I = a_n \frac{(1 - \nu^2) K_I^2}{(n+1) E C^*} \tag{3}$$

These equations allow C_B to be estimated at any time and for any structure, without recourse to finite element analysis. It must be remembered, however, that these equations can be used to estimate C_B only for stationary cracks.

Our work on growing cracks indicates that the rate of crack growth under non-steady-state conditions correlates well with the near field integral C_B. However, the time dependence of C_B is no longer adequately described by eq. (2). It therefore apppears that while we have found a parameter which characterizes the stress field in the vicinity where creep damage occurs and gives excellent correlation with creep crack growth data, it is not straightforward to determine this parameter.

The correlation between the finite element modelling and the experimental results suggests that our overall approach is correct. The important parameters which govern creep

fracture can be determined from uniaxial creep tests. They can then be used in a finite element model to simulate the rate of creep crack growth. Furthermore, accelerated creep tests on service-exposed material can be used to estimate the loss of ductility during service. This in turn can lead to an assessment of the degree of creep crack growth enhancement.

In other words, now that the validity of this method of simulating creep crack growth has been established, it can be used to perform direct simulations of creep crack growth in individual components. While this is a somewhat costly exercise, it may well be warranted for large pressure vessels.

In many situations, this may not be required. The results of Part III indicate that while the measured C integral is strictly applicable only if steady-state conditions are maintained, for small deviations from steady-state, the errors induced are not large. In particular, if the incubation time for crack initiation is larger than the time to reach a steady-state, then subsequent deviations from steady-state will not be large. Under these circumstances, crack growth estimates obtained by assuming that steady-state conditions prevail should be correct to within a factor of two at worst.

APPENDIX I

FINITE ELEMENT FORMULATION FOR CREEPING AND VISCOPLASTIC SOLIDS

The F.E.M. program we have developed follows the formulation of Kanchi et al. (1978). It is outlined below.

1. Formulation

a) Constitutive Relations

The total strain rate can be expressed as

$$\dot{\varepsilon}_{ij} = (\dot{\varepsilon}_{ij})_e + (\dot{\varepsilon}_{ij})_{vp} \tag{1}$$

where $(\dot{\varepsilon}_{ij})_e$ is the elastic strain rate, and $(\dot{\varepsilon}_{ij})_{vp}$ is the viscoplastic strain rate. The total stress rate depends on elastic strain rate according to

$$\dot{\sigma}_{ij} = D_{ijkl}\,\dot{\varepsilon}_{kl} \tag{2}$$

where D is the elasticity matrix. The viscoplastic strain rate is assumed to depend only on the current stress state, i.e.

$$(\dot{\varepsilon}_{ij})_{vp} = f(\sigma_{ij}) \tag{3}$$

The onset of viscoplastic flow can be expressed by a scalar yield condition

$$F(\sigma_{ij}, (\varepsilon_{ij})_{vp}) = 0 \tag{4}$$

Using the von Mises yield criterion, this yield condition can be expressed as

$$F = \sqrt{(3J_2)} - F_o \tag{5}$$

where J_2 is the second invariant of the stress tensor, and F_o is the yield stress.

By using a viscoplastic flow rate, eq. (3) can be expressed as

$$(\dot{\varepsilon}_{ij})_{vp} = \lambda \langle \Phi \rangle a_{ij} \tag{6}$$

Here, λ is the fluidity parameter, while a_{ij} is the current flow function, defined here by the von Mises criterion. $\langle \Phi \rangle$ is the plasticity function, defined such that

$$\langle \Phi(F) \rangle = \Phi(F) \quad \text{for } F > 0 \tag{7}$$

$$\langle \Phi(F) \rangle = 0 \quad \text{for } F \leq 0 \tag{8}$$

For a material obeying Norton's creep law, the function $\Phi(F)$ can be expressed as

$$\Phi(F) = \left(\frac{F - F_o}{F_o}\right)^N . \tag{9}$$

b) The Viscoplastic Strain Increment

In a time interval $\Delta t_n = t_{n+1} - t_n$, the strain increment can be approximated by*

$$\Delta \varepsilon_{vp}^{\ n} = \Delta t_n \left[(1 - \theta)\, \dot{\varepsilon}_{vp}^{n} + \theta \dot{\varepsilon}_{vp}^{n+1}\right] \tag{10}$$

where

i) $\theta = 0$ defines the "Euler integration" scheme, in which the strain increment is completely determined from conditions existing at time, t_n;

ii) $\theta = 1$ is the "fully implicit" scheme, in which the strain increment is determined from the strain rate corresponding to the end of time interval; while

---

* In the discussion which follows, we have eliminated tensor notation for the sake of clarity.

iii) $\theta = 1/2$ is the "implicit-trapezoidal" scheme.

By using a limited Taylor series expression, $\dot{\varepsilon}_{vp}^{n+1}$ can be approximated as

$$\dot{\varepsilon}_{vp}^{n+1} = \dot{\varepsilon}_{vp}^{n} + H^n \Delta\sigma^n \tag{11}$$

where

$$H^n = \left(\frac{\partial \dot{\varepsilon}_{vp}}{\partial \sigma}\right)^n = H^n (\Delta\sigma^n)$$

$\Delta\sigma^n$ is the stress change occurring in the time interval Δt_n. Equation (10) can now be written as

$$\Delta\varepsilon_{vp}^{n} = \Delta t_n \dot{\varepsilon}_{vp}^{n} + c^n \Delta\sigma^n \tag{12}$$

where

$$c^n = \theta \Delta t_n H^n \tag{13}$$

c) Stress-Increment

Using the incremental form, eq. (2) can be re-written as

$$\Delta\sigma^n = D \cdot \Delta\varepsilon_e^n = D (\Delta\varepsilon^n - \Delta\varepsilon_{vp}^n) . \tag{14}$$

Expressing the total strain increment in terms of displacements

$$\Delta\varepsilon^n = B^n \Delta d^n \tag{14a}$$

and substituting $\Delta\varepsilon_{vp}^n$ from eq. (12), we get,

$$\Delta\sigma^n = \bar{D}^n (B^n \Delta d^n - \varepsilon_{vp}^n \Delta t_n) \tag{15}$$

where

$$\bar{D}^n = (I + DC^n)^{-1} D = [D^{-1} + C^n]^{-1}$$

d) Equations of Equilibrium

The equations of equilibrium to be satisfied at any instant of time are

$$\int_{\Omega} [B^n]^T \sigma^n \, d\Omega + f^n = 0 \tag{17}$$

Here $d\Omega$ is the volume of interest, and f^n the vector of nodal loads. Note the B^n is employed (not B) for the displacement strain matrix, since it is possible for the strain matrix not be constant throughout the solution (i.e. if large deformations are considered). During any time step, equilibrium must be satisfied, i.e.

$$\int_{\Omega} [B^n]^T \Delta\sigma^n \, d\Omega + \Delta f^n = 0 \tag{18}$$

Using eqs. (12) and (15) the displacement increment occuring during a time step, Δt^n can be calculated as

$$\Delta d^n = [K_T^n]^{-1} \Delta U^n \tag{19}$$

$$\Delta V^n = \int_{\Omega} [B^n]^T \bar{D}^n \dot{\varepsilon}_{up} \Delta t_n \, d\Omega + \Delta f^n \tag{20}$$

where K_T^n is the tangential stiffness matrix.

$$K_T^n = \int_{\Omega} [B^n]^T \bar{D}^n [B] \, d\Omega \tag{21}$$

ΔV^n is termed the incremental pseudo-load. Substituting Δd^n into eq. (15) gives the stress increments

$$\sigma^{n+1} = \sigma^n + \Delta\sigma^n$$

and

$$d^{n+1} = d^n + \Delta d^n \tag{22}$$

By using eqs. (14) and (14a) we get

$$\Delta\varepsilon_{vp}^n = B^n \Delta d^n - \bar{D}^1 \Delta\sigma^n$$

and

$$\varepsilon_{vp}^{n+1} = \varepsilon_{vp}^n + \Delta\varepsilon_{vp}^n \tag{23}$$

e) Equilibrium Correction

Since the stress increments are based on the linearized form of the

incremental equilibrium equation (eq. (18), the equations of equilibrium will not be satisfied exactly. To correct for this a force

$$\psi^{n+1} = \int_{\Omega} [B^{n+1}]^T \sigma^{n+1} \, d\Omega + f^{n+1}$$

should be added to the pseudo-loads in the next time step.

2. Description of the FEM Program (CREEP1)

The elastic-viscoplastic F.E.M. program we have developed (CREEP1) uses 8 node and 6 node (transition) isoparametric elements. The von Mises yield criterion is adopted and the program is designed to handle plane-strain, plane-stress and axisymmetric cases. The resultant equilibrium equations are solved by using the frontal solution techniques of Irons (1970). A time stepping scheme can be selected using any of the three time progressing methods described in section (1.6). The essential steps in the solution process can be summarized as follows.

The solution begins from the known initial condition at time t=0, i.e. the static elastic solution. At this stage d^o, F^o, ε^o, σ^o are known and the viscoplastic (i.e. creep) strains are zero, $\varepsilon_{vp} = 0$. The time stepping scheme described in section (1.b) is then employed to advance the solution by one timestep at a time. For a time $t = t_n$ the following quantities are computed:

Stage 1

a) $c^n = c^n (\sigma^n, \Delta t^n)$

b) $\bar{D}^n = (D^{-1} + c^n)^{-1}$

c) $K_T^n = \int_{\Omega} [B^n]^T \bar{D}^n B^n \, d\Omega$

d) $\dot{\varepsilon}_{vp}^{\,n} = \lambda \langle \Phi \rangle a^n$

Stage 2

a) The displacement increments Δd^n are then computed according to eq. (19), as

$$\Delta d^n = [K_T^n]^{-1} \Delta U^n$$

where

$$\Delta U^n = \int_\Omega [B^n]^T \bar{D}^n \dot{\varepsilon}_{vp} \Delta t \, d\Omega + \Delta f^n$$

This solution is obtained using the frontal solution technique.

b) The stress increments $\Delta\sigma^n$ are calculated according to

$$\Delta\sigma^n = \bar{D}^n (B^n \Delta d^n - \dot{\varepsilon}_{vp}^{\,n} \Delta t_n)$$

Stage 3

The total displacements and stresses are calculated:

$$d^{n+1} = d^n + \Delta d^n$$

$$\sigma^{n+1} = \sigma^n + \Delta\sigma^n$$

Stage 4

The viscoplastic strain rate is calculated:

$$\dot{\varepsilon}_{vp}^{\,n+1} = \lambda \langle \Phi \rangle a^{n+1}$$

Stage 5

The equilibrium correction is applied using

$$\psi^{n+1} = \int_\Omega [B^n]^T \sigma^{n+1} \, d\Omega + f^{n+1}$$

If the difference in the viscoplastic strain rate between subsequent time steps is acceptably close to zero at each Gaussian integration point throughout the structure then a steady state is deemed to have been reached. In this case, the solution is determined. If not

return we return to stage 1 and repeat the entire procedure for the next time step.

If geometrical non-linearities are not included, then the strain-displacement matrix $[B^n]$ is constant throughout the analysis. In this case, the explicit method is often used ($\theta = 0$ in eq. (10)), since the stiffness matrix of the elements needs to be calculated only once and thereafter remains constant. On the other hand if geometrical non-linearities are to be included, then the implicit method ($\theta = 1$) entails little or no additional computation since for each time interval the stiffness matrix of the elements has to be re-calculated in any case. The larger time steps possible with the implicit method can then be exploited.

The implicit and trapezoidal solution techniques are numerically stable but this does not guarantee the accuracy of the solution. The explicit time integration scheme is only conditionally stable and numerical integration can only proceed for values of time stepping less than some critical value. Although implicit time integration technique allows larger time steps, both techniques have a limiting time stepping value. An estimate of the allowable stable time-step Δt_c for power-law creep is given by Cormeau (1975). In terms of the maximum effective stress sampled over all integration points

$$\Delta t_c \leq \frac{4(1+\nu)}{3E\,\lambda_c} \cdot \frac{1}{n\,\sigma_{eff}^{\,n}} \qquad (25)$$

where

σ_{eff} = effective stress

E = Young Modulus

λ_c = fludity parameter

ν = Poisson's ratio

n = Creep exponent

However there is no approximate formulation for the time step length required for the implicit scheme.

During these studies we have used the cost effective explicit time stepping procedure, with variable time increment, as suggested by Dimis and Owen (1979). The size of each time step is limited by an empirical relationship

$$\Delta t_n \leq \tau[\varepsilon_{ij}/(\dot{\varepsilon}_{ij})_{vp}]^{1/2}_{min}$$

Here ε_{ij} is the first total strain invariant and $(\dot{\varepsilon}_{ij})$ is the final creep strain rate invariant. The minimum is taken over all integration points in the geometry. τ is a time increment parameter which we set equal to 0.01 (although values of τ in the range $0.05 < \tau < 0.003$ have been reported to give satisfactory results). The initial time step is selected with the above procedure suggested by Cormeau (1975).

REFERENCES

Kanchi, M.B., O.C. Zienkiewicz and D.R.J. Owen (1978), Intl. J. Num. Meth. in Engg., 12, 169.

Irons, B.M. (1970), Intl. J. Num. Meth. in Eng., 2, 5.

Owen, D.R.J., O.C. Zienkiewicz and I.C. Cormeau (1974), Nucl. Engg. and Design, 28, 278.

Cormeau, I.C., Intl. J. Num. Meth. in Eng., 9, 109.

Dimis, L.M.S. and D.R.J. Owen (1979), Computers and Structures, 8, 207.

APPENDIX II

DETERMINATION OF CRACK TIP PARAMETERS

1. Introduction

The use of finite elements in fracture mechanics has been extensive, both in the elastic and plastic range. Generally two basic approaches have evolved. When conventional finite elements with polynomial interpolation functions are used in the crack tip region, the characteristic singularities necessitate the use of an indirect procedure such as extrapolation of a field parameter to the crack tip. Alternatively a number of special crack tip elements have been developed (Byshkov, 1970; Rice and Tracey, 1971; Bezley, 1974), where the displacement method has been used. These special crack tip elements contain a singularity of the strain field at the crack tip equal to the theoretical singularity (Irwin, 1957). One of the disadvantages of these special crack tip elements is that they lack constant strains and rigid body motion modes. Therefore they do not pass the patch test (Irons and Razzaque, 1972) and the necessary requirements for convergence are not present (Zienkiewicz, 1977).

It has been shown that elastic and fully plastic crack tip singularities can be obtained if 8 node isoparametric elements are collapsed at the crack tip, and the midside nodes near the crack tip are placed at quarter point (Basoum, 1976, 1977). The nonsingular formulation of these elements satisfies the essential convergence criteria (Zienkiewicz, 1977); namely, interelement compatibility for the constant strain modes, continuity of displacement, and rigid body motion modes. This method has been implemented in the finite element programme

(CRACK-I) and the formulation for the determination of crack tip parameters is described below.

2. Determination of Crack Tip Stress Intensity Factors by Virtual Crack Extension

The stress intensity factor is calculated either by an energy balance approach (based on the J-integral), using the displacement fields of the collapsed crack tip elements. The J integral is

$$J = \int_{\Gamma} (W - \tau \frac{\partial u}{\partial x}) \, ds$$

where

W is the strain energy density, ($W = 1/2 \, \sigma_{ij} \, \varepsilon_{ij}$ for linear elasticity),

Γ is the arbitrary contour enclosing the crack tip, and

T is the traction vector associated with the outward normal n.

The physical significance of the J-integral is as the potential energy release rate G, for plane-strain.

$$J = G = \frac{(1 - \nu^2)}{E} K_I^2 \qquad (2)$$

where G is the energy release rate, E is Young's modulus, ν is Poisson's ratio, and K_I is the stress intensity factor.

Formulation

This formulation for the stress intensity factor calculation was introduced by Parks (1974). A finite element solution produces a vector of nodal displacements {u}. Then the potential energy of the finite element solution can be obtained as

$$p = 1/2 \, \{u\}^T \, [K] \, \{u\} - \{u\}^T \, \{f\} \qquad (3)$$

where [K] is the stiffness matrix, and {f} is the vector of prescribed nodal loads.

Eq. (3) can be differentiated with respect to the crack length a, to obtain the energy release rate. Thus

$$-\left(\frac{\partial P}{\partial a}\right)_{load} = \frac{\partial \{u\}^T}{\partial a}\left(\frac{1}{2}[K]\{u\} - \{f\}\right) - \frac{1}{2}\{u\}^T \frac{\partial [K]}{\partial a}\{u\} + \{u\}^T \frac{\partial \{f\}}{\partial a} \quad (4)$$

The vector in parentheses in eq. (4) is zero in the finite element solution. Therefore for the plane strain case

$$-\left(\frac{\partial P}{\partial a}\right)_{load} = K_I^2 \frac{(1-\nu^2)}{E} = -\frac{1}{2}\{u\}^T \frac{\partial [K]}{\partial a}\{u\} + \{u\}^T \frac{\partial \{f\}}{\partial a} \quad (5)$$

The matrix $\partial[K]/\partial a$ represents the change in the master stiffness matrix per unit crack advance. Using the mesh of Fig. (1), this is determined by rigidly translating all nodes on and within the contour Γ_o by an infinitesimal amount Δa in the x direction. All other nodes remain in their initial position. Thus the master stiffness matrix [K] which depends on only individual element goemetries, displacement functions and material elastic properties, remains unchanged.

The master stiffness matrix [K] is the sum over all element stiffness matrices [k]. Therefore,

$$-\frac{1}{2}\{u\}^T \frac{\partial [K]}{\partial a}\{u\} = -\frac{1}{2}\{u\}^T \sum_{i=1}^{N_e} \frac{\partial [k_i]}{\partial a}\{u\} \quad (6)$$

where $[k_i]$ is the stiffness matrix of an element between the contours Γ_o Γ_1 and N_e is the total number of such elements. The change in such an element stiffness matrix with crack length can be calculated directly as

$$\frac{\partial [k_i]}{\partial a} = \frac{\Delta [k_i]}{\Delta a} = \frac{1}{\Delta a}\left[[k_i]_{a+\Delta a} - [k_i]_a\right] \quad (7)$$

Here $[k_i]_a$ is the stiffness of an intra-contour element calculated with its initial nodal coordinates (i.e. the stiffness used in the finite element solution) while $[k_i]_{a+\Delta a}$ is the element stiffness calculated with the x-coordinates of each of its nodes lying on Γ_o incremented by Δa.

If the loading of the body is done other than on the crack face the load vector will be independent of infinitesimal crack advance, i.e.

$$\frac{\partial\{f\}}{\partial a} = 0 \tag{8}$$

Thus eq. (2) reduces to:

$$\frac{K_I^2\,(1-\nu^2)}{E} = -\frac{1}{2}\{u\}^T \frac{\partial[K]}{\partial a} \tag{9}$$

Alternatively the stress intensity factor can be obtained from the nodal displacements of the collapsed isoparametric elements around the crack tip

$$K_I = [2G/(2\pi)/(k+1)]\,[2u_B/\sqrt{L}] \tag{10}$$

where

G = shear modulus

k = $(3-\nu)/(1+\nu)$ for plane stress

ν = Poisson's ratio

u_B = nodal displacement of a wide side node of the collapsed element

L = the element length

Computational Procedure

The program developed (CRACK-I) uses 8 node-isoparametric elements together with their collapsed version ahead of the crack tip. It

handles plane-strain, plane-stress and axisymmetric cases. The resultant equilibrium equations are solved by using the frontal solution technique of Irons (1970). The essential steps in solution process can be summarized as follows:

Stage I: The solution of the given mesh is performed and the initial stiffness matrices of the elements on the selected contours are stored together with the nodal displacements of the contour elements.

Stage II: The stiffness of the contour elements are re-calculated by moving the nodes (5×10^{-6} times crack length). The resultant variation in the stiffness matrices of the contour elements due to crack advance are calculated from eq. (7).

Stage III: The energy release rate and stress intensity factor then can be computed by using the nodal displacements obtained from the first solution, using eqs. (9) and (10) respectively.

3. Determination of Stress Intensity Factors from Displacement and Stress-Strain Solutions

The virtual crack extension procedure described above is suitable to elastic and particularly nonlinear solutions in two and three dimensions. However it is not cost effective, especially for large numbers of elements. A different method is now developed. We first extend eq. (1)

$$J = \int_{\Gamma} \left(\frac{1}{2}\sigma_{ij}\,\varepsilon_{ij} - \sigma_{11}\frac{\partial n_x}{\partial x} - \sigma_{12}\frac{\partial n_y}{\partial x}\right) dy$$

$$+ \left(\sigma_{21}\frac{\partial n_x}{\partial x} + \sigma_{22}\frac{\partial n_y}{\partial x}\right) dx$$

The stress, strain and displacements which appear in this equation are determined by the FEM solution at integration points.

The displacement derivatives appearing in the equation can be obtained through the cartesian derivatives of the shape functions at the integration points. Therefore the contour chosen should follow the integration points. Although this is possible, such a requirement is inconvenient for the input of data to the program. Alternatively the resulting stress and strains at integration points can be bilinearly extrapolated to the nodal points by using interpolating functions. This enables contour paths to follow the element edges.

This alternative determination of integral has been incorporated in CREEP-I.

References

Anderson, G.P., V.L. Ruggless and G.S. Stibor (1971), Int'l. J. Fract. Mech., 7, 63.

Basoum, R.S. (1976), Int'l. J. Num. Meth. Eng., 10, 25.

Basoum, R.S. (1977), Int'l. J. Num. Meth. Eng., 11, 85.

Bezley, J.E. (1974), Int'l. J. Num. Meth. Eng., 8, 537.

Bowie, O.L. (1964), J. App. Mech., 31, 208.

Byshkov, E. (1970), Int'l. J. Fract. Mech., 6, 159.

Chan, S.K., I.S. Tuba and W.K. Wilson (1970), Eng. Fracture Mech., 2, 1.

Evans, W.T., M.F. Light, A.R. Luxmoore (1980), J. Mech. Phys. Solids, 28, 167.

Irons, B.M. (1970), Int'l. J. Num. Meth. Eng., 2, 5.

Irons, B.M. and Razzaque (1972), Proc. Conf. Math. Foundations of FEM with Appl. to Partial Diff. Equations, Academic Press, 557.

Irwin, G.R., (1957), J. App. Mech., 24, 361.

Parks, D.M. (1974), Int'l. J. Fracture, 10, 487.

Rice, J.R., R.M. McMeeking and E.P. Soronsen (1979), Compt. Methods Appl. Mech. and Eng., 18, 411.

Rice, J.R. and D.M. Tracey (1971), Symp. Num. Meth. Struct. Mech. Urbana III.

Tracy, D.M., (1972), Eng. Fracture Mech., 3, 255.

Zienkiewicz, D.C. (1977), Finite Elements in Eng. Science, McGraw Hill (London).

Westerguard, H.M., (1939), J. App. Mech., 61, 49.

APPENDIX III

ANALYSIS OF NOTCHED BAR TENSILE CREEP TESTS

The steady state stress-strain analysis of two notched tensile test specimens has been performed using the finite element program already developed. The notch details and mesh used during the studies are given in Figs. (1) and (2). The material properties used were $E = 150\ GNm^{-2}$, $\nu = 0.3$, $B = 8.12 \times 10^{-12}\ MPa^{-3.24}\ h^{-1}$ and $n = 3.24$ where B and n are constants of Norton's power law. A uniform stress of $93.19\ MNm^{-2}$ was applied to the ends of the specimen.

The initial elastic loading and the steady-state stress-distributions for both notch geometries are given in Figs. (3) and (4). The distribution of the accumulated effective creep strains up to the beginning of the steady state are also given, in Figs. (5) and (6). Finally the results obtained for the same blunt notch geometry are compared with the results of Hayhurst et al. (1977) in Fig. (7). As can be seen, although the steady state n value is slightly different from that used by Hayhurst et al., and a very coarse mesh was used, the close agreement between the two results gives confidence in the computational formulation we have used.

Reference

Hayhurst, D.R. and J.T. Henderson (1977), Intl. J. Mech. Sci., 19, 133.

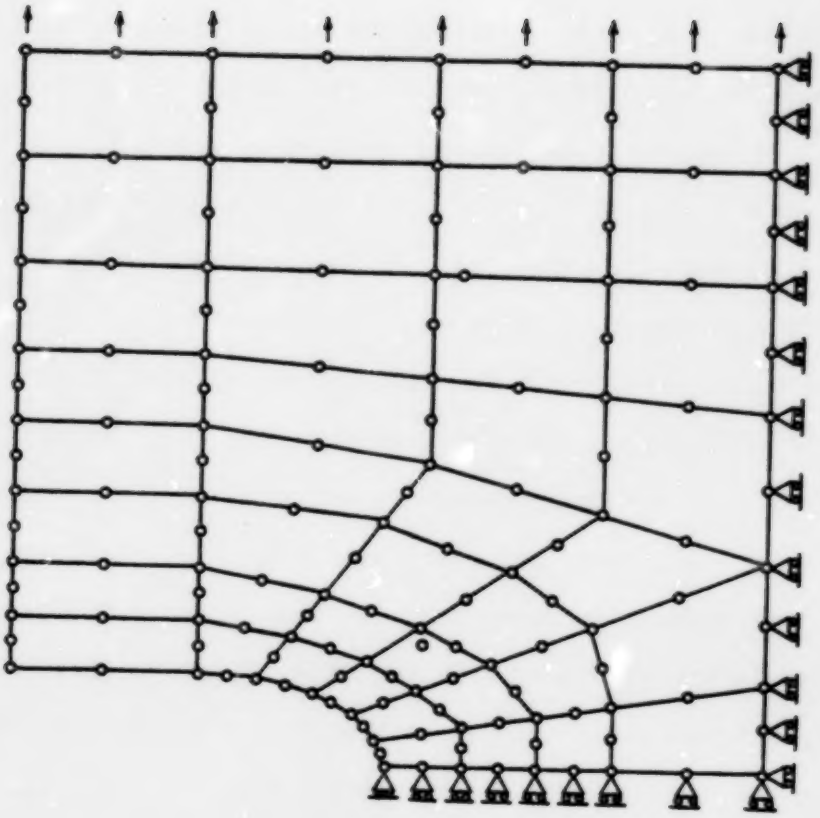

Fig. 1: The finite element mesh used to study notched bar tensile creep tests for sharp notches (notch-I). For this specimen, the minimum diameter is 5 mm, the shoulder diameter is 10 mm, and the notch root radius is 1.27 mm. This is the specimen used in the experimental work described in Part II.

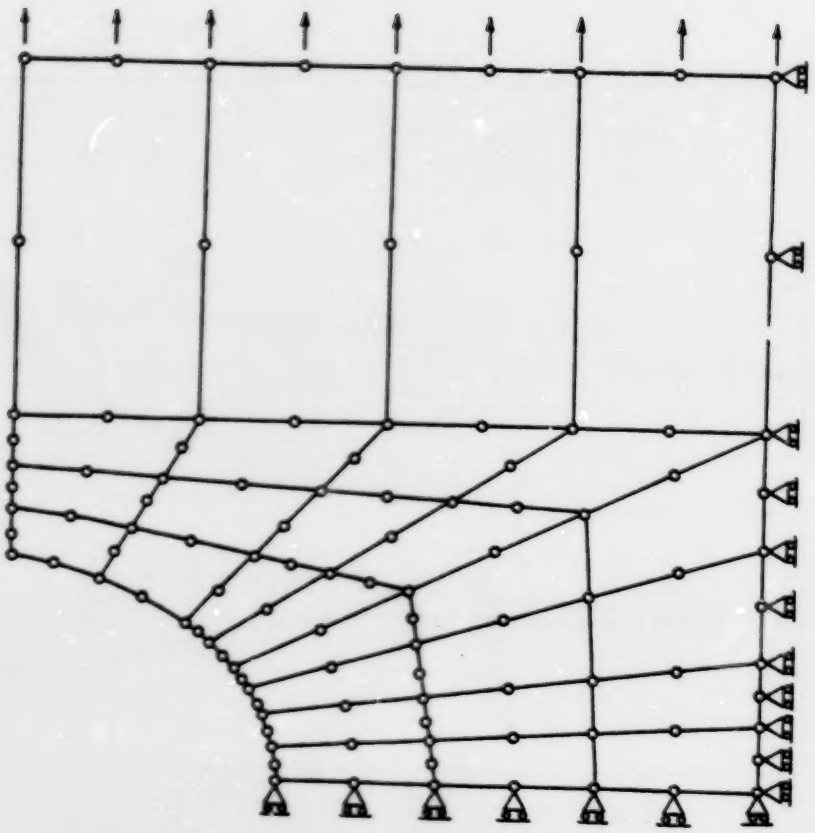

Fig. 2: The finite element mesh used to study notched bar tensile creep tests for blunt notches (notch-II). For this specimen, the minimum diameter is 10 mm, the shoulder diameter is 16.7 mm, and the notch root radius is 3.35 mm.

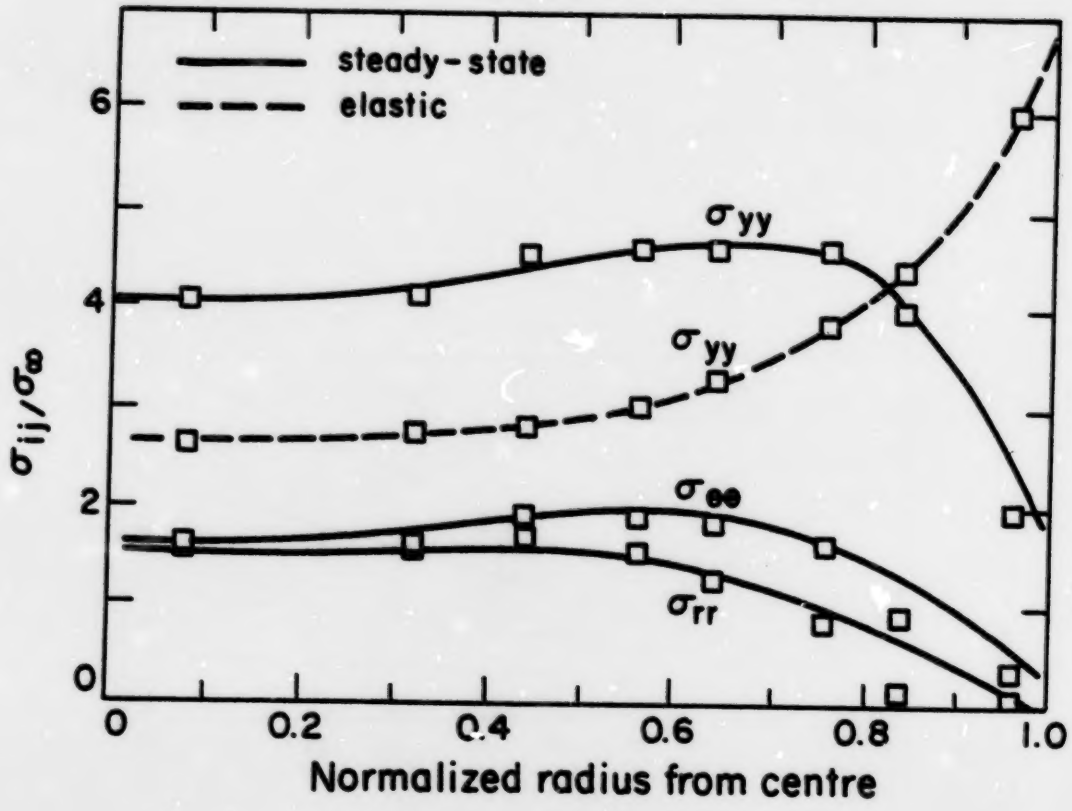

Fig. 3: The initial elastic and steady-state stress distributions for the sharp notch. (For reasons of clarity only the σ_{yy} stress is given for the elastic field).

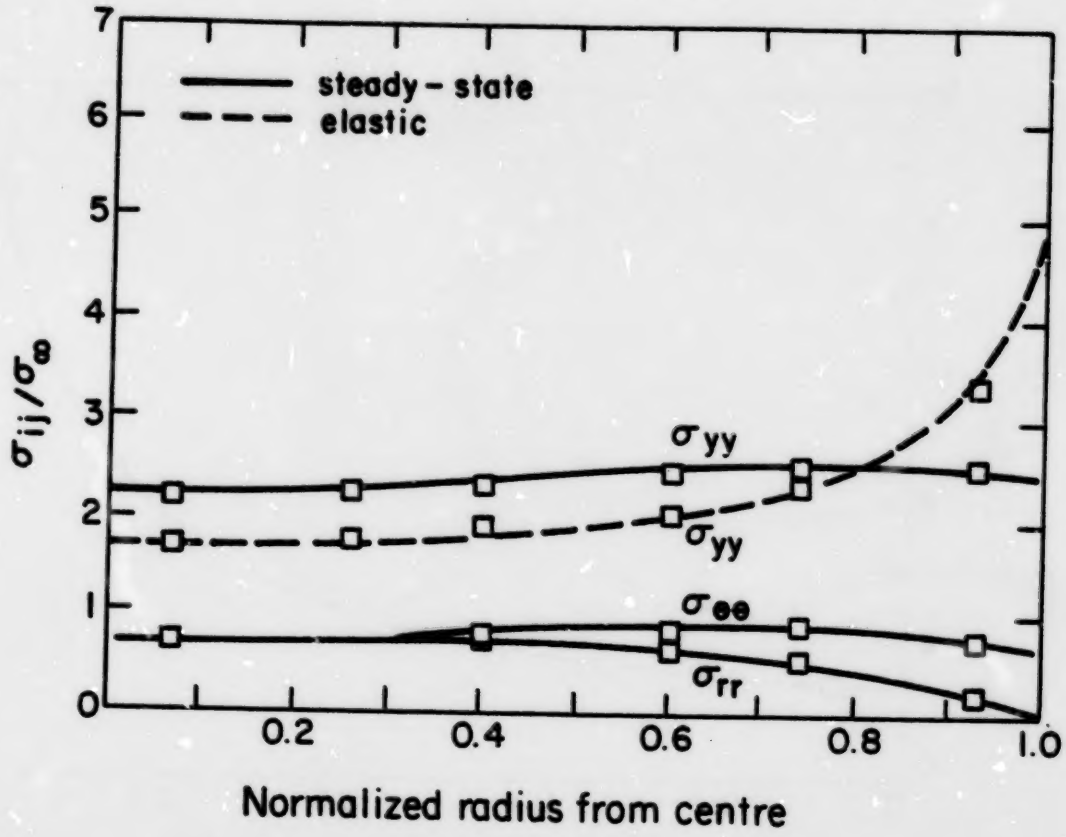

Fig. 4: The initial elastic and steady-state stress distribution for the blunt notch. (For reasons of clarity, only the σ_{yy} stress is given for the elastic field).

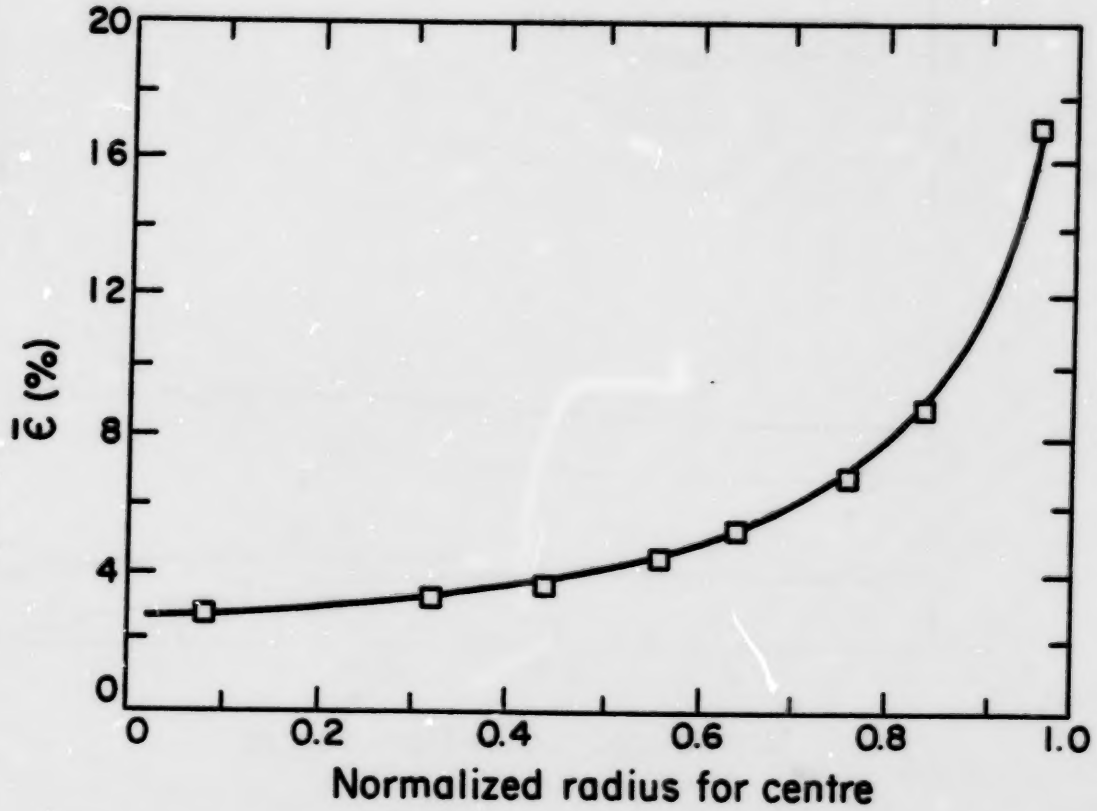

Fig. 5: The effective strain distribution in the neck, at the onset of steady-state for the sharp notch.

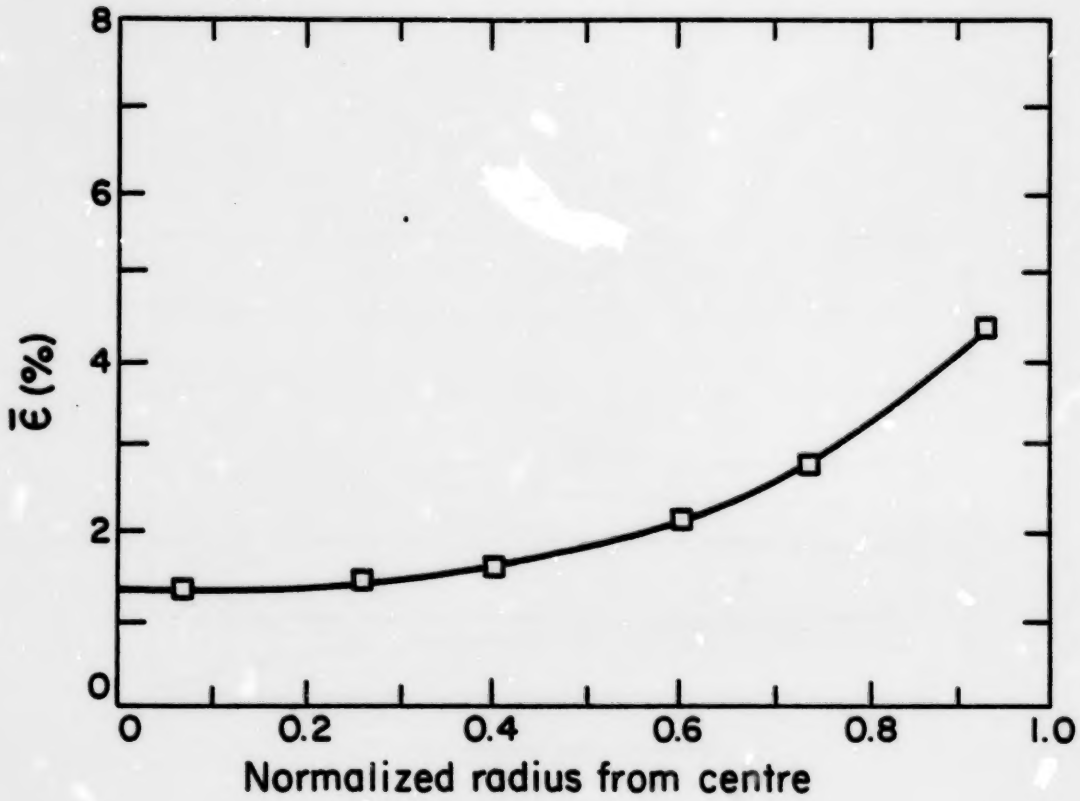

Fig. 6: The effective strain distribution in the neck, at the onset of steady-state for the blunt notch.

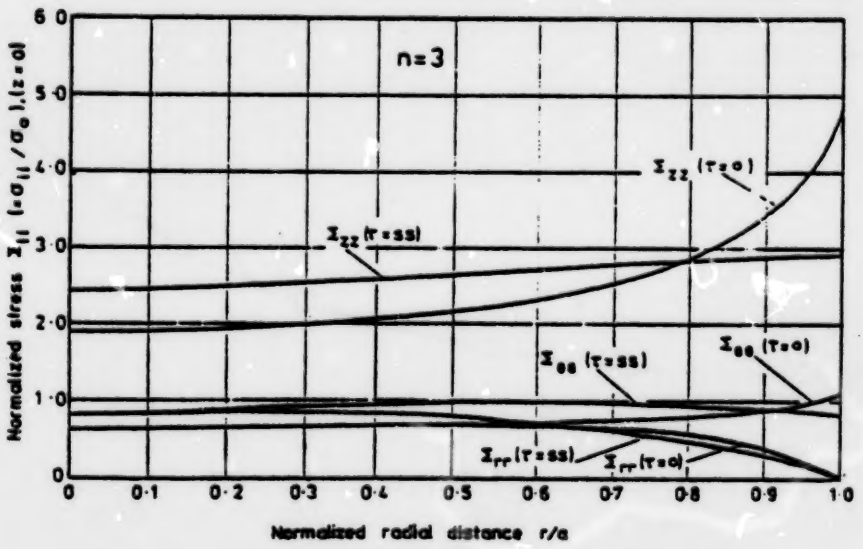

Fig. 7: The results of Hayhurst et al. (1977) for the same blunt notch. These results should be compared with Figure 6.

POOR

QUALITY

ORIGINAL